Reducing the Signaling Overhead of Contemporary and Future Wireless Networks

Trinity College Dublin
Coláiste na Tríonóide, Baile Átha Cliath
The University of Dublin

Danilo Lelin Li

Electronic & Electrical Engineering Department

The University of Dublin
Trinity College

This dissertation is submitted for the degree of

Doctor of Philosophy

Trinity College Dublin January 2025

I dedicate this thesis to my family and friends who supported me during this challenging journey.

Declaration

I declare that this thesis has not been submitted as an exercise for a degree at this or any other university and is entirely my own work.

I agree to deposit this thesis in the University's open access institutional repository or allow the Library to do so on my behalf, subject to Irish Copyright Legislation and Trinity College Library conditions of use and acknowledgement.

Signed:

Danilo Lelin Li

Danilo Lelin Li
January 2025

Summary

Signaling overhead reduction has always been a challenging task in the design of wireless networks. New applications and services in future networks, such as autonomous vehicles, and deployment of higher frequency bands, e.g., millimeter-wave and terahertz bands, face the common issue of wireless channels with large number of paths that have time-varying coefficients. The rich multipath components of the channels create delay spread. It causes inter-symbol interference in the signal, which has to be managed by guard periods in time, e.g., cyclic prefix (CP). Additionally, a high-mobility wireless environment between the transmit and receive antennas causes Doppler shifts in the channel, resulting in time-varying channel coefficients. In such scenarios, frequent channel estimation updates are required, demanding frequent transmission of pilot sequences. Consequently, the pilot signal and CP lead to substantial signaling overhead that negatively impacts spectral efficiency and leads to additional latency. Therefore, the focus of this thesis is on the overhead reduction. In particular, this thesis proposes novel approaches, for contemporary and future wireless networks, capable of dealing with the delay and Doppler spreads of the channel with significantly reduced overhead.

The first contribution of this thesis reduce the overhead of one of the main technologies of 5G systems, the orthogonal frequency-division multiplexing (OFDM)-based massive multiple-input multiple-output (MIMO). This thesis brings substantial training overhead reduction through a novel joint channel estimation and equalization technique that requires only a single pilot subcarrier. This is possible by exploiting the channel correlation property induced by spatial diversity, and the fundamental concept of coherence bandwidth. Given the design parameters of 5G systems, the coherence bandwidth extends across multiple subcarrier bands. Hence, a band of subcarriers can be equalized with the channel estimate at a single subcarrier. Subsequently, the detected data symbols are considered as virtual pilots, and the channel frequency responses (CFRs) are updated at each subcarrier. Thereafter, the remaining channel estimation and equalization can be performed in a sliding manner. Furthermore, multiple channel estimates within the coherence bandwidth create additional frequency diversity, therefore multiple channel estimates are used to equalize the data at each subcarrier. This makes the proposed technique surpass contemporary systems that use

multiple pilot subcarriers in terms of bit error rate (BER) and signal-to-interference-plus-noise ratio (SINR) performance.

As the new generation of applications and services emerge, the wireless environment becomes more time-varying, and hence, a larger overhead is required. In OFDM, the Doppler shifts of the channel break the orthogonality among the subcarriers, leading to severe inter-carrier interference. As a paradigm-shifting technology, orthogonal time frequency space (OTFS), which places the data symbols in the delay Doppler (DD) domain, has recently emerged. In the DD domain, the equivalent channel is sparse and time-invariant. As the second contribution, this thesis uses time-reversal maximum ratio combining (TR-MRC) to completely remove the CP of OTFS-based massive MIMO systems, substantially reducing the overhead. Noticeably, apart from the SE gains achieved by removing the CP, the proposed technique also reduces the duration of the OTFS block, which mitigates the effects of channel aging. Additionally, the asymptotic analysis in this thesis reveals that TR-MRC averages the large variations of the channel into the channel correlation. This insight leads to breaking the limitations of OTFS with the proposed residual Doppler correction (RDC) windowing. The specific limitation addressed is the assumption of approximately constant channel gains for the delay blocks of samples within each OTFS block. Simulation results show that using the RDC windowing to correct the channel variations within each OTFS block leads to a SINR performance close to static scenarios, even for substantially larger Doppler spreads.

Another issue of OTFS systems is the large spectral efficiency loss caused by the overhead required for channel estimation. In the current literature, OTFS deploys mostly embedded pilot (EP) structures, which use guard intervals that are twice the length of the channel delay spread to avoid interference between the pilot and data symbols. Hence, to reduce the pilot overhead, this thesis proposes a novel split pilot structure with two impulse pilots that share the same reduced guard interval. This way, the proposed split pilot can reduce the channel estimation overhead by almost half compared to the EP scheme. The challenge to reducing the delay guard rests on the interference between the pilot and the data symbols. With two impulse pilots, each pilot can be used to remove the other pilot's interference over data. This is while the data interference over the pilot can be initially absorbed into noise due to the large pilot power. To improve the accuracy of this method, this thesis also proposes to remove data interference over the channel estimates iteratively using the initial data estimates. This significantly improves the BER performance of split pilots with as few as two interference cancellation stages.

Acknowledgements

First I would like to thank my supervisor Prof. Arman Farhang for his invaluable guidance, feedback, and encouragement throughout my PhD. His countless hours of dedication were certainly crucial for all my achievements over the last four years.

I would also like to express my gratitude to my colleagues Mohsen Bayat, Arman Azizi, Sanoopkumar, Stephen McWade, Mohamad, Hanning, and Jia Liang. Each of them contributed to my research with meaningful discussions and made work life more enjoyable.

I am also grateful for the friends I made in Ireland and the ones I had in Brazil. I will not name all of them, as I believe every friend I made contributed. Even those that I have less contact at the present moment. Finding good friends is one skill I can confidently and boastfully say I excel at. The joyful moments I had throughout these years can certainly corroborate these claims.

Finally, I would like to thank my loving family for all their support. I certainly would not have reached this stage without their guidance, inspiration and encouragement.

Table of contents

List of figures

List of tables

List of Acronyms

3GPP 3rd Generation Partnership Project

AWGN additive white Gaussian noise

BCCB block circulant with circulant blocks

BEM basis expansion model

BER bit error rate

BS base station

CFR channel frequency response

CIR channel impulse response

CMs complex multiplications

CP cyclic prefix

CSI channel state information

DAC Digital-to-analog converter

DD delay-Doppler

DFT discrete Fourier transform

EVA Extended Vehicular A

EPA Extended Pedestrian A

EP embedded pilot

ETU Extended Typical Urban

FFT fast Fourier transform

IBI inter block interference

ICI inter-carrier interference

i.i.d. independent and identically distributed

IDFT inverse discrete Fourier transform (DFT)

IRS intelligent reflecting surfaces

ISFFT inverse symplectic Fourier transform (SFFT)

ISI inter-symbol interference

LTI linear time invariant

LS least squares

LSMR least squares minimum residual

LTV linear time varying

MIMO multiple input multiple output

ML maximum likelihood

MMSE minimum mean square error

MP message passing

MRC maximum ratio combining

MUI multiuser interference

NMSE normalized mean square error

OFDM orthogonal frequency-division multiplexing

OTFS orthogonal time frequency space

PCP pilot with cyclic prefix

PDF probability density function

PDP power delay profile

QAM quadrature amplitude modulation

RDC residual Doppler correction

SFFT symplectic Fourier transform

SINR signal to interference and noise ratio

SIR signal to interference ratio

SNR signal-to-noise ratio

STFT short-time Fourier transform

TDD time-division duplexing

TDL-C Tapped delay line model C

TR-MRC time reversal maximum ratio combining

UL uplink

US Uncorrelated Scattering

WSS Wide-Sense Stationary

WSSUS wide-sense stationary uncorrelated scattering

ZC Zadoff-Chu

Chapter 1

Introduction

Wireless communication is undoubtedly one of the most impactful engineering achievements that has shaped the present-day lifestyle. From the initial stages in the early 1900s, among radio and television broadcasting, wireless systems have rejoiced in significant research and improvement. Fast forward to the present, wireless computers and mobile phones have become indispensable items for the majority of the world's population. Yet, as these communication methods have advanced, so have the demands placed on them. With each new innovation, humanity finds new applications that push the boundaries of wireless systems, requiring even more sophisticated techniques.

As we look ahead to the future with 6G and beyond, we see a growing array of applications involving drone communications, high-speed trains, low-earth-orbit (LEO) satellites, autonomous driving (both aerial and terrestrial), and millimeter wave wireless communications [1–4]. These applications have led to a continuous stream of breakthroughs in areas such as space exploration and global connectivity through the deployment of mega-constellations of satellites. However, further progress of all these applications is hindered by a common issue: the large signaling overhead required to deal with doubly selective channels, which is one of the major challenges of 6G systems [5]. A channel is considered doubly selective when the channel experiences both time and frequency selectivity. The multipath characteristic of the channel causes the frequency selectivity. When the signal takes multiple paths to reach the receiver, it experiences different delays, which causes delay spread and a frequency-selective channel. The Doppler effect can occur in a wireless system when either the transmit or receive antennas are in motion during transmission. As the transmit and receive antennas move closer together or further apart, the frequency of the received signal shifts based on the relative speeds of the antennas, the speed of the signal, and the frequency of the transmitted signal [6, 7]. Therefore, Doppler spread channels become a challenge in scenarios involving high mobility, underwater communications where the signals are acoustic, and high signal frequencies, such as millimeter wave and Terahertz communications [8]. In these scenarios, conventional techniques designed for frequency selective channels, such as orthogonal frequency-division multiplexing (OFDM) and massive multiple input multiple output (MIMO) technologies, struggle to provide the efficient and reliable communication needed for these advanced applications. Hence, to meet the demands of reliability, high data rate, and low latency required by emerging applications, significant improvements or entirely new technologies are necessary [9].

When large Doppler shifts are present in the channel, the channel impulse response (CIR) varies rapidly, demanding a frequent need to track the channel variations. This results in a significant channel estimation overhead, which greatly impacts the system's spectral efficiency, data rate, and latency. As a comparison, existing systems for static channels require only one pilot sequence per frame, while those for linear time varying (LTV) channels deploy a pilot sequence for each symbol [10]. To solve this issue, the focus of this thesis is on solutions that reduce the transmission overhead required to deal with the delay and Doppler spreads of the channel. More specifically, this thesis aims to tackle two primary contributors to the high signaling overhead in high mobility systems: pilot sequences and delay spread guards, e.g., the cyclic prefix (CP). The proposed solutions are developed using two main approaches. In the first stage, this thesis studies well-established technologies in 5G systems, such as OFDM and massive MIMO, to propose new approaches to improve the spectral efficiency of the current standards. Second, this thesis investigates a promising emerging technology that has already become one of the main contender techniques for high mobility cases, the orthogonal time frequency space (OTFS) modulation [11, 12]. The subsequent sections provide an overview of these technologies, emphasizing their key advantages and the challenges that lead to the research questions this thesis addresses.

1.1 Overhead reduction in OFDM-based Massive MIMO

Massive MIMO has revolutionized wireless communications as a technology capable of significantly enhancing the spectral efficiency of multiuser systems [13–15]. Through the deployment of a large number of antennas at the base station (BS), massive MIMO systems can serve multiple users that simultaneously transmit data over the same time-frequency resources [16, 17]. This is achieved by exploiting the spatial diversity, which can efficiently average out noise and multiuser interference (MUI) in the system with low-complexity linear combining detectors, thanks to the massive number of antennas deployed at the BS. Specifically, massive MIMO transforms the randomness of the channel into a predictable statistical value, i.e., the correlation of the channel. As the number of BS antennas tends to infinity, the average of the matched filtered channel of each user becomes the autocorrelation of the channel. Furthermore, when the channels between the users are uncorrelated, MUI at the matched filter output averages out.

Therefore, an accurate channel frequency response (CFR) at each subcarrier and every BS antenna becomes a prerequisite of massive MIMO systems. Hence, channel estimation becomes a demanding factor, requiring long pilot sequences. It is also worth noting that conventional impulsive-based channel sounding methods are feasible only when the channel is linear time invariant (LTI), where the estimated channel at the pilot signal remains unchanged at the data transmission instance. This becomes a challenge in LTV channels since the frequent need to update the channel estimates introduces a substantial signaling overhead, which can severely impact the system's spectral efficiency. Hence, novel approaches are required for channel estimation.

This thesis takes an interesting approach by proposing techniques that focus on the channel correlation instead of only the autocorrelation. This approach has two main benefits. The correlation of the channel varies much slower in both frequency and time domains compared to each channel instance. Furthermore, the time-frequency channel correlation is a function of the difference in time and frequency. In other words, the channel correlation between two adjacent data subcarriers is constant. These benefits lead to the following research question.

Question 1

- Is it possible to reduce the selectivity of the channel into its known and constant correlation function to minimize the channel estimation overhead?

1.2 Overhead Reduction in OTFS Modulation

OTFS is an emerging modulation technique that shows significant advantages over OFDM in high Doppler channels [11, 18, 19]. Different from OFDM, where the data symbols are placed in the time-frequency domain, OTFS places the data symbols in

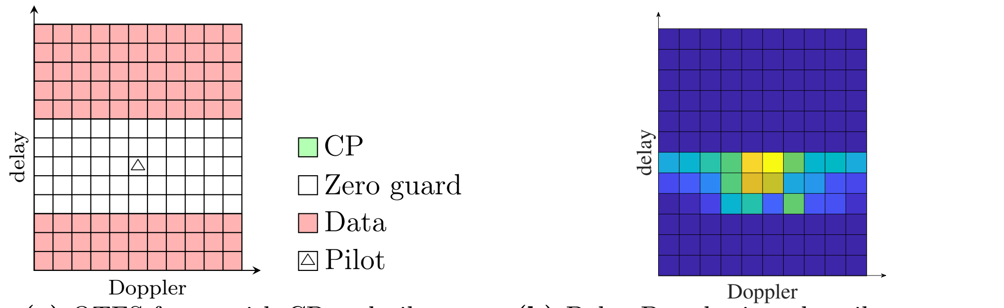

(a) OTFS frame with CP and pilot. **(b)** Delay Doppler impulse pilot response.

Fig. 1.1 Signaling overhead of OTFS (a) and the delay Doppler impulsive pilot response (b).

the delay-Doppler (DD) domain. This unique approach is advantageous due to the sparsity of the channel in the DD domain and the near-constant channel gains within each symbol. This advantage makes OTFS robust against the delay and Doppler shifts of the channel. Hence it is a promising technology in combating the adverse effects of the LTV channels. Apart from its robustness to doubly spread channels, OTFS is also attractive for deployment in future networks due to its backward compatibility with OFDM and the current standards [20].

Since its first appearance in literature [11], OTFS has gained extraordinary interest from both the research community and industry. This led to significant improvements of OTFS in various fronts. This includes alternative implementation schemes of OTFS with Zak transform [21] or OFDM-based implementations [22, 23] that significantly simplify the representation of the equivalent channel and showcase the backward compatibility of OTFS. Additionally, channel estimation techniques such as the embedded pilot (EP) scheme, which employs a single impulsive pilot in the DD plane surrounded by zero-guards [10] as shown in Fig. 1.1 (a), or pilot with cyclic prefix (PCP) scheme, where the high power impulse pilot is spread using the Zadoff-Chu (ZC) sequence [24]. However, there is still significant room for improvement in OTFS. To deal with the doubly spread channel shown in Fig. 1.1 (b), OTFS requires a large signaling overhead from CP and channel estimation, as shown in Fig. 1.1 (a), leading to an immense spectral efficiency loss. To address this issue, this thesis proposes solutions to reduce the overhead on two fronts: CP and pilot overhead.

1.2.1 CP Overhead Reduction

One of the main issues that OTFS faces is the large signaling overhead. One of the main contributors to the large overhead is the CP as its length can be up to 25% of the symbol duration in its extended form as devised in the 3GPP 5G NR standard [25]. Furthermore, many OTFS techniques rely on the approximation of a static channel over each delay block within the DD grid. This is only possible by shortening the duration of each delay block to approximate the channel as constant. However, the CP becomes a bottleneck to this solution as the required CP length depends only on the channel's delay spread and not the delay block's length. Hence, shortening a delay block would incur severe spectral efficiency loss. As a result, analysis of the effect of reduced CP in OTFS systems has become a research area that has attracted considerable attention [26–28]. To this end, the authors in [26] have shown that the CP overhead can be reduced to only one CP at the beginning of each OTFS block instead of having multiple CPs at the beginning of each delay block. Recently, the authors in [29, 30] have shown that in massive MIMO systems one can dispense the redundant CP by application of time reversal maximum ratio combining (TR-MRC) in LTI channels. Motivated by the results in [29, 30] and aiming to completely remove CP in OTFS, the following research question arises.

Question 2

- Can TR-MRC average out doubly spread channel effects and break the Doppler limitations of OTFS?

1.2.2 Pilot Overhead Reduction

Another source of the large signaling overhead of OTFS systems is the pilot signal for channel estimation. To reduce the pilot overhead, the authors in [10] presented a reduced guard EP for integer Doppler scenarios by reducing the zero guard across the Doppler dimension to twice the maximum Doppler index. The authors in [31–33] proposed a superimposed pilot structure to remove the pilot overhead completely. This technique superimposes a high-power pilot signal over data along the whole DD domain and uses previously estimated delay and Doppler parameters to extract the channel estimates. In [34], the authors developed a basis expansion model (BEM) based joint channel estimation and detection technique for impulse pilot with reduced guard across Doppler dimension. This method consists of deploying a reduced Doppler guard and iteratively refining the estimated channel and data using detected data as pseudo-pilots.

It is evident the efforts in the literature to reduce the Doppler guard in channel estimation. However, in many cases, the delay guard causes a larger pilot overhead than the Doppler guard. Despite that, the literature on reducing the delay guard is scarce. This can be attributed to the fact that in LTI systems, the channel in the frequency domain does not suffer from delay spread. Therefore, channel estimation requires only a pilot sequence equal to the channel length, contrary to channel estimation in the delay domain which requires a pilot sequence almost twice as long. However, the scenario changes for LTV channels. When the channel is doubly spread, channel estimation in frequency domain suffers from the Doppler spread and for this reason, OTFS systems rely on estimating the channel in the delay domain. Hence, in the efforts of reducing OTFS systems overhead, the following research question is raised.

Question 3

- Is it possible to reduce the pilot overhead along the delay dimension to a minimum, i.e., to the channel length, thereby almost halving the pilot overhead?

1.3 Contributions

The main objective of this thesis is to propose solutions to reduce the large overhead required in high Doppler scenarios. To this end, three novel techniques are proposed in this thesis. First, a novel technique is proposed for OFDM-based massive MIMO systems. It is worth noting that the massive MIMO literature primarily discusses flat fading channels. Consequently, some properties of multicarrier systems are not fully exploited, one of which is the coherence bandwidth of the channel. The coherence bandwidth determines the range of signal bandwidth over which the channel can be approximated as constant, i.e., flat fading. In most cases, practical wideband systems cannot limit their bandwidth to within the coherence bandwidth. However, in OFDM, the bandwidth of multiple adjacent subcarriers falls within the coherence bandwidth. Therefore, a band of subcarriers' data can be detected using only one reference subcarrier's channel estimate. Thereafter, the detected data can be considered as virtual pilots to update the channel estimates. The updated channel estimates are then used to equalize a new adjacent band of subcarriers. Hence, by repeating the process in a sliding manner, all the data symbols and the CFR can be estimated, starting from one reference pilot. Ultimately, the proposed technique requires pilots only for the reference subcarrier instead of estimating the CFR. As a result, the proposed technique brings a substantial reduction in training overhead for OFDM-based massive MIMO LTI systems.

Moving to the topic of CP overhead of OTFS systems, this thesis analyzes the effect of TR-MRC in OTFS-based massive MIMO systems. TR-MRC focuses the CIR of the channel into a single point and, with the spatial diversity of massive MIMO, completely diminishes the effect of the delay spread of the channel. Furthermore, this thesis shows that with the assumption of locally time-invariant channels over each delay block, both the delay and the Doppler spread of the channel at the time-reversal combiner output average out as the number of BS antennas grows large. However, for considerably large Doppler shifts, this assumption does not hold and a residual Doppler effect remains after time-reversal combining. An interesting finding of this thesis is that in the asymptotic regime, this effect reduces to a scaling by the channels correlation function. Based on this observation, residual Doppler correction (RDC) window is proposed as a novel solution to address the Doppler limitation of OTFS. Simulations show that by using RDC windowing, OTFS systems can achieve bit error rate (BER) performance comparable to static scenarios, even with Doppler shifts corresponding to speeds of up to 2000 kmph. Furthermore, for systems operating at lower speeds, additional simulations demonstrate that similar performance can be achieved even with longer delay block durations.

While the TR-MRC and RDC windowing is capable of completely removing CP overhead and breaking the Doppler limitations of OTFS-based massive MIMO systems, it still requires accurate channel estimates. The most prevalent channel estimation technique in the OTFS literature deploys an EP scheme, which has a significant drawback: the large pilot overhead. To solve this issue, this thesis proposes a channel estimation design where the delay guard is reduced by half compared to the conventional EP schemes, leading to a significant gain in spectral efficiency. When reducing the delay guard, the delay spread causes the transmitted pilot to corrupt the surrounding data and vice versa. Hence the proposed technique utilizes a split pilot structure with two impulse pilots to circumvent this problem. In the channel estimation stage, the responses of the split pilots are combined, and an initial channel estimate is obtained by considering the data interference as noise. In the channel equalization stage, the two pilots are used to effectively remove the pilot interference from the received signal, without losing the data information. It is also proven in this thesis that this step is impossible when only a single pilot with insufficient delay guards is employed. Without the pilot interference over data, the data can be estimated with conventional detectors such as the least squares minimum residual (LSMR)-based technique with interference cancellation [35]. To improve the accuracy of the data estimates, an iterative joint channel estimation and detection step can be considered. This method uses the data estimates to remove the data interference from the channel estimates at each iteration. It is shown through simulations that this additional step significantly improves the BER performance of the split pilot structure. Furthermore, it has a high convergence speed, as two iterations are sufficient even in very high Doppler scenarios.

The contributions of this thesis can be summarized as follows.

- A joint channel estimation and equalization massive MIMO technique that requires a single pilot subcarrier is developed. This technique offers substantial overhead reduction as it can capture the time or frequency variations of the channel through the use of the transmitted data as virtual pilots.

- This thesis also studies the TR-MRC technique in OTFS-based massive MIMO systems. This proves to offer a significant spectral efficiency improvement as it allows the removal of CP from the system. Furthermore, the TR-MRC is followed by the RDC windowing, which corrects the channel variations between the channel estimates. This alleviates the restrictions of OTFS, where each Doppler bin must be sufficiently short for the time variations within to be negligible.

- This thesis also proposes a novel OTFS channel estimation technique with a split pilot scheme that only requires half the delay guard required in EP schemes. Hence, the total channel estimation overhead is reduced by almost half. An iterative method is used to deal with the interference between data and the pilot caused by the delay spread. The iterative method considerably improves the performance of the system with as few as two iterations.

1.4 Structure of the Thesis

The structure of this thesis is laid out as follows. Chapter 2 provides a background and literature review of the key concepts presented in this thesis. Namely, the foundations of the wireless channel medium, massive MIMO, OFDM, and OTFS modulation are the topics addressed in Chapter 2. Chapter 3 describes the proposed joint channel estimation and equalization technique that requires only a single impulsive pilot subcarrier. This technique takes advantage of the channel correlation to estimate the data at frequency instances adjacent to the transmitted pilot. The detected data is then used as virtual pilots to update the channel estimates, which allows for data at further frequencies to be estimated. This process is repeated sequentially until the transmitted data at all frequencies are estimated. This addresses the research question presented in Section 1.1. The large overhead caused by CP and the first research question raised in Section 1.2 are addressed in Chapter 4. This issue is solved with the TR-MRC technique. Furthermore, this chapter discusses how TR-MRC can deal with the Doppler spread as well, and proposes the RDC windowing technique to correct the channel variation within each Doppler slot of the channel. Chapter 5 focuses on reducing the pilot overhead of OTFS systems, and the second research question raised in Section 1.2. To this end, a split pilot channel estimation scheme is proposed. This scheme reduces the pilot overhead by almost half compared to the EP based scheme vastly used in the literature. Finally, Chapter 6 concludes this thesis and discusses future research questions that emanate from this thesis.

1.5 Publications

The following publications are related to this thesis.

- **D. L. Li** and A. Farhang, "OTFS without CP in Massive MIMO: Breaking Doppler limitations with TR-MRC and Windowing," *2022 IEEE Wireless Communications and Networking Conference (WCNC)* [36].

- **D. L. Li** and A. Farhang, "Joint Channel Estimation and Equalization in Massive MIMO Using a Single Pilot Subcarrier," *IEEE Wireless Communications Letters (WCL)* [37].

- **D. L. Li**, S. P. S., and A. Farhang, "Reduced Overhead Channel Estimation for OTFS With Split Pilot," *Accepted in the 2024 IEEE Global Communications Conference Workshops (GLOBECOM).*

Chapter 2

Background and Literature Review

This chapter provides a brief background theory and literature review necessary for the thesis. This chapter starts with the mathematical model of the wireless channel. Then, a detailed explanation of massive MIMO, OFDM, and some of their key benefits are provided. This chapter focuses on their main advantages in 5G systems, and how these benefits are affected by LTV channels. Finally, this chapter concludes with the introduction of a new modulation technique called OTFS. OTFS was recently proposed in the literature as a substitute to OFDM in high Doppler scenarios.

2.1 Wireless Transmission Channel

To effectively understand and design any wireless communication system, it is essential to have a deep understanding of the physical transmission channel. When the signal is sent through the channel, it undergoes multiple fading effects, e.g. attenuation, shadowing, and scattering [6, 38]. These effects cause interference between the received samples while leading to fluctuations in the received power. Thus, to detect the received signal, it is important to understand and model the channel appropriately.

The channel impairments are generally divided into two categories: large-scale fading and small-scale fading. Large-scale fading accounts for the path loss due to distance and shadowing of large objects, while small-scale fading accounts for interference from multiple channel paths. The large-scale fading defines the received signal power, which varies according to the channel environment and the distance from the transmit to the receive antenna. The distance between antennas typically varies only slightly over multiple transmission frames, resulting in a constant large-scale fading effect across these frames. Therefore, large-scale fading determines the received signal power and consequently, given any noise level, the signal-to-noise ratio (SNR) at the receiver input. For this reason, the attenuation from large-scale fading is generally not the focus of channel estimation and equalization techniques.

Depending on the wireless environment of the channel, the signal can take multiple paths to reach the receiving antenna(s). The small-scale fading represents the phase shifts and attenuations from different propagation paths. Different environments can have diverse channel effects, influencing the performance of channel estimation and equalization methods. The interference from each propagation path can be modeled with three parameters: delay shift, Doppler shift, and path gain. Each parameter can differ greatly according to the transmission environment.

- **The Delay shift** is caused by the different arrival times of the multipath components.
- **The Doppler shift** refers to the signal frequency change due to the movement between the transmit and receive antenna or reflector object.
- **The path gain** represents the power decay of the signal on a propagation path.

Therefore, the channel is modeled as the summation of the received signals from P channel paths. Each path p is characterized by its own path gain, delay shift, and Doppler shift, represented by α_p, τ_p, and υ_p, respectively. Hence, for any transmitted signal $s(t)$, the received signal, ignoring noise, can be modeled as

$$r(t) = \sum_{p=0}^{P-1} \alpha_p e^{2j\pi\upsilon_\mathrm{p} t} s(t-\tau_p). \tag{2.1}$$

Since the input-output response of the channel is linear, the channel can also be described by the impulse response

$$h(\tau,t) = \sum_{p=0}^{P-1} \alpha_p e^{2j\pi\upsilon_\mathrm{p} t} \delta(\tau-\tau_p), \tag{2.2}$$

and the received signal is given as

$$r(t) = \int h(\tau,t) s(t-\tau) d\tau. \tag{2.3}$$

From (2.2), one may observe that in the special case of a stationary environment, i.e., when there is no Doppler effect in the channel, the impulse response does not depend on time t. Therefore, in LTI systems, estimating the impulse response at any time t provides the channel input-output response for the whole transmission frame. This property offers an initial insight into why LTV systems become more challenging than LTI systems. A more detailed comparison between the two scenarios will be given in the following sections of this chapter.

In digital communication systems, analog-to-digital conversion is the first step after down-converting the received signal to the baseband. Hence, it is convenient to convert the continuous time channel in the passband to its equivalent discrete-time representation in the baseband. Consider a transmit signal $s(t)$ constructed from the $M \times 1$ vector $\mathbf{x}$ with M discrete symbols, $x[m]$, with an ideal sinc interpolation Digital-to-analog converter (DAC) [39, p. 428] at a sampling period of T_s, i.e.,

$$s(t) = \sum_{m=0}^{M-1} x[m] \mathrm{sinc}(\frac{t}{T_\mathrm{s}} - m). \tag{2.4}$$

Substituting (2.4) in (2.1), the received signal becomes

$$r(t) = \sum_{p=0}^{P-1} \sum_{m=0}^{M-1} \alpha_p e^{2j\pi \upsilon_\mathrm{p} t} x[m] \mathrm{sinc}(\frac{t - \tau_p}{T_\mathrm{s}} - m). \tag{2.5}$$

Finally, sampling the received signal with the same sampling period T_s results in

$$r[n] = r(nT_\mathrm{s}) = \sum_{p=0}^{P-1} \sum_{m=0}^{M-1} \alpha_p e^{2j\pi \upsilon_\mathrm{p} n T_\mathrm{s}} x[m] \mathrm{sinc}[n - m - \frac{\tau_p}{T_\mathrm{s}}]. \tag{2.6}$$

In practical systems, the sampling period is short enough to approximate the path delays to the nearest sampling points. Consequently, the delay shift τ_p of each path p can be approximated to the nearest discretized sample. Hence, fractional delays are generally not considered and each τ_p is approximated as an integer multiple of the sampling period T_s, i.e., $\tau_p \approx \ell_{\tau_p} T_\mathrm{s}$ where $\ell_{\tau_p} \in [0, L-1]$ and L is the number of delay taps after discretization [40]. Hence, (2.6) is reduced to

$$\boxed{r[n] = \sum_{p=0}^{P-1} \alpha_p e^{2j\pi \upsilon_\mathrm{p} n T_\mathrm{s}} x[n - \ell_p].} \tag{2.7}$$

Equation (2.7) can also presented in the vectorized form as,

$$\mathbf{r} = \mathbf{H}\mathbf{x}, \tag{2.8}$$

where $[\mathbf{H}]_{m,n} = \sum_{p=0}^{P-1} \alpha_p e^{2j\pi \upsilon_{\mathrm{p}} m T_{\mathrm{s}}} \delta(m - n - \ell_p)$, with $m \in [0, M + L - 2]$ and $n \in [0, M - 1]$.

The essence of channel estimation is presented in (2.7). Observe that each column of $\mathbf{H}$ contains exactly L non-zero elements. An impulsive pilot-based channel estimator transmits an impulse pilot surrounded by zero guards. Transmitting an impulse at any given index n, returns the $L \times 1$ vector $\mathbf{h}_n$, containing the non-zero elements of the n-th column of $\mathbf{H}$.

Throughout this thesis, the channel of any transmitted signal will be modeled based on (2.7). Our main objective is to discuss how to retrieve the transmit signal $x[n - \ell_p]$ from the received signal $r[n]$ in the most spectral efficient manner. The following subsections provide a thorough background review of how to mathematically model the channel and its different representations. Subsection 2.1.1 describes how the channel impulse response is derived and represented in different domains. Subsequently, a description of the channel model and statistics of the channel parameters are given in subsection 2.1.2.

2.1.1 The Channel in Different Domains

One of the primary challenges of dealing with the channel revolves around estimating the channel with the least amount of overhead, and maintaining low complexity in channel equalization. Developing effective techniques to uphold the required efficiency requires a comprehensive understanding of the channel's properties. Hence, in this subsection, various representations of the channel are derived, exploring the advantages of each representation.

As mentioned previously, the channel small-scale fading affects the transmit signal through scaling, delay shifts, and Doppler shifts. Hence, a generic representation of the channel with a continuum of scatterers can be given as

$$r(t) = \int_{-\infty}^{\infty} \int_{-\infty}^{\infty} h(\tau, \upsilon) e^{2j\pi \upsilon t} s(t - \tau) d\tau d\upsilon, \tag{2.9}$$

where $h(\tau, \upsilon)$ is the DD spreading function and determines the attenuation at a given delay τ and Doppler υ. It is worth noting that in any environment, the channel is limited by a maximum delay and maximum Doppler, i.e., $\tau \in [0, \tau_{\max}]$

and $\upsilon \in [-\upsilon_{\max}, \upsilon_{\max}]$. Hence, the limits of the integrals in (2.9) can be reduced to the respective delay and Doppler limits of any given channel scenario. However, throughout this chapter, the integral limits in (2.9) are kept at $[-\infty, \infty]$ for the sake of generalization.

The spreading function of a channel with P discrete scatterers is represented as [41]

$$h(\tau, \upsilon) = \sum_{p=0}^{P-1} \alpha_p \delta(\tau - \tau_p)\delta(\upsilon - \upsilon_p), \tag{2.10}$$

and (2.1) can be derived by substituting (2.10) in (2.9). A discrete number of scatterers can be observed when looking at a single snapshot of the channel. Since a transmission frame spans in the order of milliseconds, the physical channel, and therefore, the scattering parameters, can be considered constant through the transmission [42]. Hence, a discrete number of scatterers is considered throughout this thesis, as it is widely used in the literature [6, 7, 11, 16].

As the Doppler shift affects the frequency of the transmitted channel, its effect is more evident when analyzing the received signal in the frequency domain. Let $S(f)$ and $R(f)$ represent the frequency domain transmit signal and receive signal, respectively. The dual of (2.9) is given as

$$R(f) = \int_{-\infty}^{\infty}\int_{-\infty}^{\infty} h(\tau, \upsilon) e^{-2j\pi\tau(f-\upsilon)} S(f - \upsilon) d\tau d\upsilon. \tag{2.11}$$

The duality of the received signal shines light into an interesting analysis of the channel. Each domain of the channel has different properties that can be taken advantage of during channel estimation and equalization. For example, substituting (2.10) in (2.11) and considering a static channel (no Doppler effect) results in

$$R(f) = \left(\sum_{p=0}^{P-1} \alpha_p e^{-2j\pi\tau_p f} \right) S(f). \tag{2.12}$$

In other words, the channel effect becomes a simple scaling effect, and the channel detection stage becomes significantly simplified.

The channel representation is not restricted to only the time or frequency domains. Consider the transmit and receive signal as a 2D function where the signal is divided into multiple time blocks, i.e.,

$$s(t_m, t_n) = s(t_m + t_n T), \tag{2.13}$$

where T is a design parameter representing the duration of a time block, $t_m \in [0, T)$ represents the time instance within each time block, and $t_n \in \mathbb{Z}$ represents the time block index. In the following derivations, T is designed to be larger than the maximum delay $\tau_{\max}$ of the channel. Substituting the above equation in (2.1) results in

$$r(t_m, t_n) = \int_{-\infty}^{\infty} \int_{-\infty}^{\infty} h(\tau, \upsilon) e^{2j\pi\upsilon(t_m + t_n T)} s(t_m - \tau, t_n). \tag{2.14}$$

With a 2D signal, it is possible to analyze a time-dependent frequency domain channel. This leads to two additional channel representations: the time-frequency and DD channels. These representations can better capture the time variations of the channel and thus provide interesting properties to combat LTV channels.

The time-frequency channel is obtained through a short-time Fourier transform (STFT)

$$X(f, n) = \int_{-\infty}^{\infty} x(t) w(t - n) e^{-j2\pi t f} dt, \tag{2.15}$$

where $w(t - \omega)$ is a window function and $X(f, \omega)$ is the STFT of $x(t)w(t - n)$. By dividing the whole signal into shorter segments, it is possible to limit the channel variations within each segment.

Considering a rectangular window function $\mathrm{rect}(\frac{t - T(t_n + 0.5)}{T})$ at the transmitter and receiver as shown in Fig. 2.1, the STFT of the received signal can be obtained as

$$R(f_m, t_n) = \int_{-\infty}^{\infty} \int_{-\infty}^{\infty} h(\tau, \upsilon) e^{2j\pi t_n T \upsilon} e^{-2j\pi\tau(f_m - \upsilon)} S(f_m - \upsilon, t_n) d\tau d\upsilon. \tag{2.16}$$

Substituting (2.10) in (2.16), results in

$$R(f_m, t_n) = \sum_{p=0}^{P-1} \alpha_p e^{2j\pi t_n T \upsilon_p} e^{-2j\pi\tau_p(f_m - \upsilon_p)} S(f_m - \upsilon_p, t_n). \tag{2.17}$$

It may be observed from the equation above that the channel becomes significantly simplified in LTI systems. With the absence of the Doppler effect, the following properties appear.

- The channel becomes a scaling effect.
- For any frequency f_m, the channel is constant for all values of t_n.

A scaling channel, i.e., a single-tap channel, significantly simplifies the channel equalization step of the system. Furthermore, with a constant channel along t_n, the

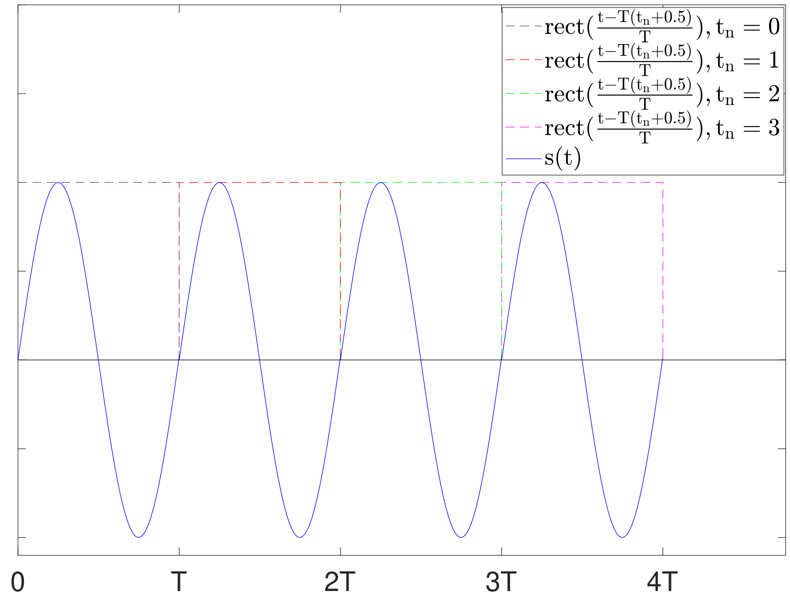

Fig. 2.1 Transmit signal multiplied by rectangular windows in function of t_n.

channel needs to be only estimated once within all values of t_n. Hence, the channel estimation overhead is reduced.

However, these benefits are lost with the introduction of high Doppler shifts. Noticeably, the Doppler shift causes interference between the signal in different frequencies f_m. Furthermore, the channel ages from one time slot t_n to the next.

While the time-frequency channel can be seen as taking the time parameter t_m to frequency f_m while keeping the time dependency on t_n, the DD domain channel takes t_n to frequency f_n while dependent on the time variable t_m. In other words, the DD equivalent channel is given as

$$R(t_m, f_n) = \int_{-\infty}^{\infty} \int_{-\infty}^{\infty} h(\tau, \upsilon) e^{2j\pi\upsilon t_m} S(t_m - \tau, f_n - \upsilon) d\tau d\upsilon. \tag{2.18}$$

This can be derived from a discrete-time Fourier transform with a sampling spacing of T, starting at time t_m. Alternatively, the channel can also be derived as the Fourier transform of the signal $s(t)$ multiplied by a train of impulses with a period T and time-shifted by t_m, as shown in Figure 2.2.

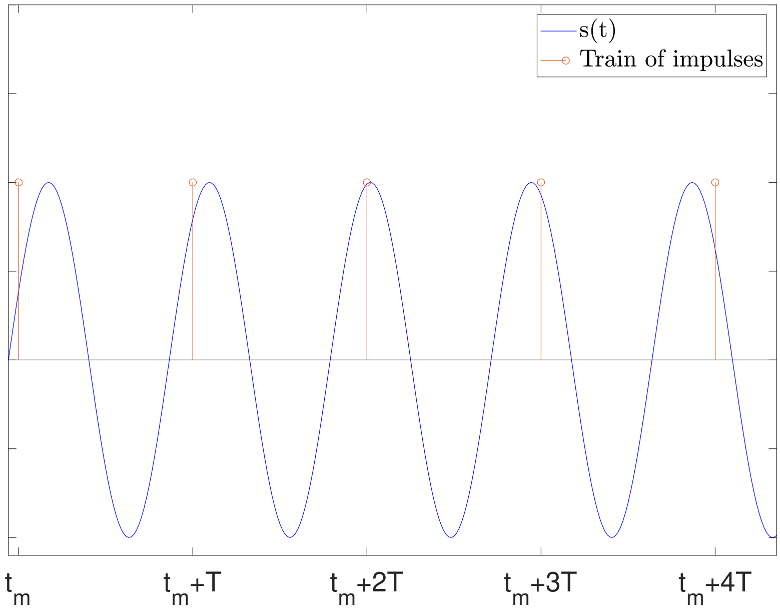

Fig. 2.2 Transmit signal multiplied by a train of impulses time shifted by t_m.

Substituting (2.10) in (2.18), results in

$$R(t_m, f_n) = \sum_{p=0}^{P-1} \alpha_p e^{2j\pi t_m \upsilon_p} S(t_m - \tau_p, f_n - \upsilon_p). \tag{2.19}$$

This representation highlights the following unique properties of the channel.

- The channel is independent of the parameter f_n, i.e., the channel is now invariant over f_n
- If T is short enough to approximate the channel as a constant within the segment, i.e., $e^{2j\pi t_m \upsilon_p} \approx e^{2j\pi t'_m \upsilon_p}$, for any value of t_m and t'_m, the channel becomes invariant over t_m and f_n.
- The impulse response is sparse, with impulses on the delay and Doppler pairs of each channel path.

An invariant channel can reduce the overhead required for channel estimation. Furthermore, it can also improve the accuracy when estimating the transmitted signal. The sparsity of the channel can also reduce the complexity of channel equalization techniques.

2.1.2 Channel Model

Each specific environment may exhibit different channel characteristics and a deterministic model of the channel for each individual scenario is unfeasible. However, it is crucial for a wireless system to perform well under a variety of operating conditions. Therefore, understanding the stochastic properties required to model the channel is essential for ensuring consistent performance across a range of wireless channels. In this regard, the wide-sense stationary uncorrelated scattering (WSSUS) channel model is one of the most important and employed in the literature [6, 7, 43].

2.1.2.1 WSSUS channels and Correlation Function

The channel Correlation Function represents the statistical relationship between channels in any two instances. This is an important parameter to characterize the rate of change of a channel. Consider the delay-time channel correlation

$$\mathbb{E}\{h^*(\tau,t)h(\tau',t')\} = C_{\mathrm{DT}}(t,t',\tau,\tau'). \tag{2.20}$$

Observe from the above equation that the channel correlation depends on 4 variables. However, a simplified description of the channel was proposed in [43] with the assumption of WSSUS.

A. Uncorrelated Scattering

Uncorrelated Scattering (US) assumes that the channel paths with different delay taps are uncorrelated,i.e.,

$$\mathbb{E}\{h^*(\tau,t)h(\tau',t')\} = C_{\mathrm{DT}}(t,t',\tau,\tau')\delta(\tau-\tau'). \tag{2.21}$$

B. Wide-sense Stationary

Wide-Sense Stationary (WSS) assumes that the channel parameters remain consistent within the observed channel time-frequency window, i.e.,

$$\mathbb{E}\{h^*(\tau,t)h(\tau',t')\} = C_{\mathrm{DT}}(0,t-t',\tau,\tau'). \tag{2.22}$$

In conjunction, the WSSUS channel model simplifies the channel correlation, allowing it to be characterized by only two variables, namely

$$\mathbb{E}\{h^*(\tau,t)h(\tau',t')\} = C_{\mathrm{DT}}(\Delta t,\tau), \tag{2.23}$$

where $\Delta t = t - t'$ represents the time difference between the two channel instances.

The assumption of WSSUS extends to all the channel domains. Consider the DD Correlation function

$$\mathbb{E}\{h^*(\tau,\upsilon)h(\tau',\upsilon')\} = C_{\mathrm{DD}}(\tau,\tau',\upsilon,\upsilon'). \tag{2.24}$$

Each channel path is characterized by a delay and Doppler pair. Under the US assumption, the delay and the Doppler of two different scatterers are uncorrelated. Consequently, (2.21) can be extended to the delay Doppler domain

$$\mathbb{E}\{h(\tau,\upsilon)^*h(\tau',\upsilon')\} = C_{\mathrm{DD}}(\tau,\tau',\upsilon,\upsilon')\delta(\tau-\tau')\delta(\upsilon-\upsilon') = C_{\mathrm{DD}}(\tau,\upsilon). \tag{2.25}$$

Following the same line of thought, the WSS extends to the time-frequency correlation function. By definition, WSS assumes that the channel parameters remain constant within the observed time-frequency window. Hence, the time-frequency correlation function can be characterized by the time and frequency differences between the channel instances, i.e.,

$$\mathbb{E}\{h^*(t,f)h(t',f')\} = C_{\mathrm{TF}}(\Delta t,\Delta f), \tag{2.26}$$

where $\Delta f = f - f'$.

2.1.2.2 Modeling the Channel

The most common and simplest probabilistic model for the channel is the Rayleigh fading model [6, 7]. This model is most suitable when there is a sufficiently large number of propagation paths at each delay tap. Under such scenarios, the channel response $[\mathbf{H}]_{n+\ell,n}$ at any delay tap ℓ becomes a summation of many independent random path gain variables. Consequently, the Central Limit Theorem dictates that the channel response at each delay tap can be modeled as a Gaussian process.

The Rayleigh fading models each channel instance as a complex random variable and the correlation function dictates the channel's rate of change. Within the literature, it is common to define the correlation function into separable delay and Doppler correlations, i.e., $C_{\mathrm{DD}}(\tau, \upsilon) = c_{\mathrm{delay}}(\tau) c_{\mathrm{Doppler}}(\upsilon)$ [7]. This simplifies the channel modeling as the delay and Doppler correlations can now be analyzed individually.

A. Delay Correlation

The delay correlation $c_{\mathrm{delay}}(\ell) = \sigma_\ell^2$ dictates the variance of each tap shown in the Rayleigh channel model, i.e., $[\mathbf{H}]_{n+\ell,n} \sim \mathcal{CN}(0, \sigma_\ell^2)$. The delay correlation at all delay taps is termed as the power delay profile (PDP) of the channel $\boldsymbol{\rho} = [\sigma_0^2, ..., \sigma_{L-1}^2]^{\mathrm{T}}$, and has normalized power, i.e., $\sum_{\ell=0}^{L-1} \sigma_\ell^2 = 1$. A common model to design the PDP of the channel is the exponential decaying delay profile [7], namely

$$c_{\mathrm{delay}}(\tau) = \begin{cases} \frac{1}{\tau_0} e^{-\tau/\tau_0}, & \text{if } \tau < \tau_{\mathrm{max}}, \\ 0, & \text{if } \tau > \tau_{\mathrm{max}}, \end{cases} \tag{2.27}$$

where τ_0 is a delay design parameter. Alternatively, the PDP can model more specific scenarios, e.g., Extended Vehicular A (EVA) and Extended Typical Urban (ETU) models from the 4G standards [44], or Tapped delay line model C (TDL-C) model from 5G standards [45]. These models are generated from an ensemble of the physical channel measurements in given scenarios.

With a separable correlation, the frequency correlation, dual of delay, becomes separable too. Consider the time-frequency correlation $C_{\mathrm{TF}}(\Delta t, \Delta f) = c_{\mathrm{time}}(\Delta t) c_{\mathrm{freq}}(\Delta f)$. Under the assumption of no Doppler spread, i.e., $c_{\mathrm{time}}(\Delta t) = 1, \forall \Delta t$, the time frequency correlation becomes $C_{\mathrm{TF}}(\Delta t, \Delta f) = c_{\mathrm{freq}}(\Delta f)$. Hence, the frequency correlation can be derived from (2.12) as

$$\begin{aligned} c_{\mathrm{freq}}(\Delta f) &= \mathbb{E}\{h^*(t, f) h(t', f')\} \\ &= \mathbb{E}\{\sum_{p=0}^{P-1} |\alpha_p|^2 e^{-2j\pi\tau_p \Delta f}\} \\ &= \int_0^{\tau_{\mathrm{max}}} c_{\mathrm{delay}}(\tau) e^{-2j\pi\tau\Delta f} d\tau. \end{aligned} \tag{2.28}$$

B. Doppler Correlation

At any given path p, the Doppler frequency υ_{p} is given by the relative speed of the transmitter with respect to the receiver and signal frequency

$$\upsilon_{\mathrm{p}} = f_{\mathrm{c}} \frac{V}{3.6C}, \tag{2.29}$$

where f_c represents the carrier frequency, V km/h represents the relative speed and $C \approx 3 \times 10^8$ m/s is the speed of light. It is worth noting that even when the transmitter is moving at a constant speed, its relative speed is dependent on the angle of arrival of each scattering path. With this in mind, the most common Doppler correlation model, the Jake model [46], dictates that for a given maximum Doppler frequency $\upsilon_{\max}$, the Doppler shift of each path is given by

$$\upsilon_{\mathrm{p}} = f_{\mathrm{c}} \frac{V_{\max} \cos(\theta_p)}{3.6C} = \upsilon_{\max} \cos(\theta_p), \tag{2.30}$$

where θ_p is uniformly distributed within the range $[-\pi, \pi]$, i.e. $\theta_p \sim \mathcal{U}(-\pi, \pi)$. Hence, the probability density function (PDF) of the Doppler frequencies, i.e., the Doppler correlation is given as

$$c_{\mathrm{Doppler}}(\upsilon) = \begin{cases} \frac{1}{\pi\sqrt{\upsilon_{\max}^2 - \upsilon^2}}, & \text{if } |\upsilon| < \upsilon_{\max}, \\ 0, & \text{if } |\upsilon| > \upsilon_{\max}. \end{cases} \tag{2.31}$$

The time correlation as a separable function can be derived by considering the delay time channel without delay spread. In the Jakes model, the time correlation is given as

$$\begin{aligned} c_{\mathrm{time}}(\Delta t) &= \mathbb{E}\{\sum_{p=0}^{P-1} |\alpha_p|^2 e^{j2\pi\upsilon_p \Delta t}\} \\ &= \int_{-\infty}^{\infty} e^{j2\pi\Delta t \upsilon_{\max}\cos(\theta)} f(\theta) d\theta \\ &= J_0(2\pi\upsilon_{\max}\Delta t), \end{aligned} \tag{2.32}$$

where $f(\theta) = \frac{1}{2\pi}$ is the PDF of θ and $J_0(\cdot)$ denotes the zero-order Bessel function of the first kind. The time correlation can also be derived in the same fashion as in (2.28), i.e.,

$$c_{\mathrm{time}}(\Delta t) = \int_{-\upsilon_{\max}}^{\upsilon_{\max}} c_{\mathrm{Doppler}}(\upsilon) e^{2j\pi\upsilon\Delta t} d\upsilon. \tag{2.33}$$

An interesting observation from (2.28) and (2.33) is that the duality extends to correlation functions. The frequency/time correlation can be derived from the delay/Doppler correlation through a Fourier transform.

2.1.2.3 Coherence Time and Frequency

The last parameter discussed in this thesis that influences the channel models is the transmission system design parameters. Specifically, a transmission frame can be restricted within a time-frequency window where the channel is approximately constant, i.e., the correlation at any two instances is high. Thus, the terms *coherent bandwidth* F_c and *coherent time* T_c arise. When the transmitted signal is within the intervals F_c/T_c in the frequency/time domain, the effect of delay/Doppler spread can be approximated as zero. Typically, F_c and T_c are defined as [6]

$$F_c = \frac{1}{2\tau_{\max}} \text{ and } T_c = \frac{1}{8\upsilon_{\max}}. \tag{2.34}$$

Apart from the high correlation, coherence time and frequency can be analyzed according to the system's sampling parameters. Consider a system where the bandwidth is limited within the coherence frequency, i.e., $B_{\mathrm{w}} = F_c = \frac{1}{2\tau_{\max}}$. Under these conditions, the sampling period becomes twice as long as the maximum delay shift $T_{\mathrm{s}} = 2\tau_{\max}$. Hence, it becomes plausible to round all the delay shifts to the same nearest sampling point, leading to a maximum delay tap of zero.

Example 2-1

Consider a Rayleigh channel model with an exponential decaying PDP and a Jake model Doppler profile. If the receiver antenna is stationary while the transmitter antenna moves at a speed of $v = 50$ km/h, and the signal is modulated at a carrier frequency of $f_c = 5.9$ GHz, the maximum Doppler of the channel is calculated as $\upsilon_{\max} \approx 250$ Hz. The maximum delay is set as $\tau_{\max} = 5$ μs, the same value as in the ETU model, and the PDP delay parameter set to $\tau_0 = 2.5$ μs.

Under the given conditions, the coherence time and frequency are

$$F_c = 100 \text{ kHz and } T_c = 0.5 \text{ ms}, \tag{2.35}$$

with the corresponding correlation of

$$c_{\text{freq}}(F_c) = 0.62 - 0.49\jmath \text{ and } c_{\text{time}}(T_c) = 0.85. \tag{2.36}$$

Figure 2.3 shows the time-frequency and delay Doppler correlation functions.

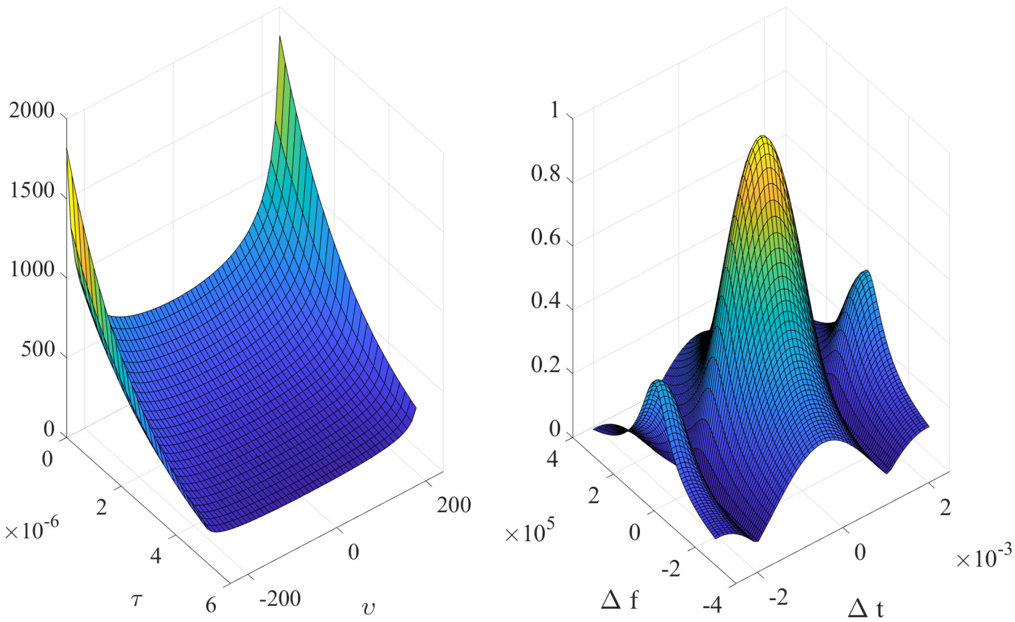

Fig. 2.3 Delay Doppler Correlation function (left) and time-frequency Correlation function (right).

2.2 5G Key technologies

In this section, two technologies that greatly improved the spectral efficiency of wireless communication systems are presented. Namely, OFDM and massive MIMO. We focus on how these technologies improve the spectral efficiency of 5G systems, with LTI channels, and how they are affected in LTV channels.

2.2.1 OFDM

OFDM has been the technology of choice for 4G and 5G systems. One of the main benefits of OFDM is its robustness to multipath fading in LTI systems. By placing the data in the frequency domain, the channel becomes single-tap scaling factor. This allows for an efficient channel estimation and low complexity equalization. These benefits become evident when analyzing the equivalent channel of the system.

In OFDM, each transmission stream is divided into multiple narrow-band subcarriers. Each subcarrier is placed in different frequency bins, with overlapping Nyquist pulses to avoid inter-carrier interference (ICI). An OFDM symbol with M subcarriers can be obtained with an M-point inverse DFT (IDFT) operation

$$\mathbf{s} = \mathbf{F}_M^{\mathrm{H}} \mathbf{x}, \tag{2.37}$$

where $\mathbf{x}$ represents a $M \times 1$ vector containing the transmitted complex data samples, and $\mathbf{F}_M$ is the normalized M-point DFT matrix with the elements $[\mathbf{F}_M]_{mn} = \frac{1}{\sqrt{M}} e^{\frac{-j2\pi mn}{M}}$, for $m,\ n = 0, ..., M-1$. To analyze the effect of the channel, refer back to (2.8),

$$\mathbf{r} = \mathbf{H}\mathbf{s} = \mathbf{H}\mathbf{F}_M^{\mathrm{H}} \mathbf{x}. \tag{2.38}$$

Observe that the channel has a transient, extending $\mathbf{r}$ into $(M + L - 1) \times 1$ vector. Naturally, if a signal is transmitted prior to $\mathbf{x}$, the channel transient causes severe inter-symbol interference (ISI). To avoid this interference, a CP of length $M_{\mathrm{CP}} \geq L-1$ is appended at the beginning of the signal, i.e., the last M_{CP} samples of $\mathbf{x}$ are appended at the beginning of the transmitted signal. This operation can be performed by the matrix $\mathbf{A}_{\mathrm{CP}} = [\mathbf{G}_{\mathrm{CP}}^{\mathrm{T}}, \mathbf{I}_M]^{\mathrm{T}}$, where the $M_{\mathrm{CP}} \times M$ matrix $\mathbf{G}_{\mathrm{CP}}$ includes the last M_{CP} rows of $\mathbf{I}_M$. Hence, the received signal becomes

$$\mathbf{r} = \mathbf{H}\mathbf{A}_{\mathrm{CP}}\mathbf{s} = \mathbf{H}\mathbf{A}_{\mathrm{CP}}\mathbf{F}_M^{\mathrm{H}} \mathbf{x}. \tag{2.39}$$

The CP is then removed at the receiver with the matrix $\mathbf{R}_{\mathrm{CP}} = [\mathbf{0}_{M \times M_{\mathrm{CP}}}, \mathbf{I}_M]$. Finally, demodulation is performed with the DFT matrix, and the transmitted data can be reconstructed from

$$\mathbf{y} = \mathbf{F}_M \mathbf{R}_{\mathrm{CP}} \mathbf{H}\mathbf{A}_{\mathrm{CP}}\mathbf{F}_M^{\mathrm{H}} \mathbf{x} = \mathbf{H}_{\mathrm{eq}}^{\mathrm{OFDM}} \mathbf{x}. \tag{2.40}$$

2.2.1.1 LTI channel

Consider first the case of an LTI channel. In the absence of the Doppler effect, the elements of $\mathbf{H}$ are constant along each diagonal, i.e., $[\mathbf{H}]_{i,j} = [\mathbf{H}]_{i',j'}$ if $(i-j) = (i'-j')$, and $\mathbf{H}$ becomes a Toeplitz matrix. Considering the CP addition and removal matrices, the effective time-domain channel matrix $\mathbf{R}_{\mathrm{CP}}\mathbf{H}\mathbf{A}_{\mathrm{CP}}$ is a circulant matrix, with the first column given by the vector $[\mathbf{h}_0^{\mathrm{T}}, \mathbf{0}_{1 \times M-L}]^{\mathrm{T}}$, and the vector $\mathbf{h}_0$ represents the time domain CIR of length L and contains L non-zero elements of the first column of $\mathbf{H}$. Due to the circulant property of the channel, the OFDM equivalent channel becomes

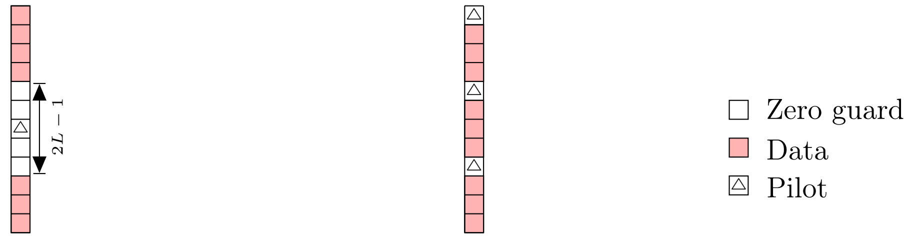

Time domain impulse pilot Frequency domain impulse pilot

Fig. 2.4 Pilot placement in time (left) and frequency (right) domains.

diagonalized by the DFT matrices

$$\mathbf{H}_{\mathrm{eq}}^{\mathrm{OFDM}} = \mathbf{F}_M \mathrm{circ}\{[\mathbf{h}_0^{\mathrm{T}}, \mathbf{0}_{1\times \mathrm{M-L}}]^{\mathrm{T}}\}\mathbf{F}_{\mathrm{M}}^{\mathrm{H}} = \mathrm{diag}\{\sqrt{\mathrm{M}}\mathbf{F}_{\mathrm{M}}[\mathbf{h}_0^{\mathrm{T}}, \mathbf{0}_{1\times \mathrm{M-L}}]^{\mathrm{T}}\} = \mathrm{diag}\{\boldsymbol{\lambda}\}, \tag{2.41}$$

where the $M \times 1$ vector $\boldsymbol{\lambda}$ represents the CFR, i.e., $\boldsymbol{\lambda} = \sqrt{M}\mathbf{F}_M[\mathbf{h}_0^{\mathrm{T}}, \mathbf{0}_{1\times M-L}]^{\mathrm{T}}$.

Hence, the OFDM equivalent channel scales the transmit data symbols on different subcarriers with the frequency response of the channel at the center of each subcarrier band. Consequently, the channel effect can be undone by using a simple single-tap equalizer. Furthermore, a second advantage of a single-tap channel is found in channel estimation, where the pilot overhead is reduced, as shown in [47].

When the channel estimation is performed in the time domain, the delay spread causes the transmitted impulse pilot to interfere with the transmitted data and vice versa. To avoid this issue, a zero guard of length $L-1$ is appended before and after the impulse, as shown in Figure 2.4. Therefore, the total overhead spent for channel estimation is $2L-1$ samples.

On the other hand, OFDM channels do not cause interference between the transmitted subcarriers. Hence, the zero guard in channel estimation is unnecessary. The channel can be fully extracted by allocating L equally spaced impulses in the frequency domain, as shown in Figure 2.4 [47, 48]. Let $\mathcal{I}$ represent the subcarrier indices allocated to the pilot. After transmission of the pilot signal, the received subcarriers with index $\mathcal{I}$ form the vector $\boldsymbol{\lambda}^{\mathcal{I}}$, given as

$$\boldsymbol{\lambda}^{\mathcal{I}} = \sqrt{M}\mathbf{F}_M^{\mathcal{I}}\mathbf{h}_0, \tag{2.42}$$

where $\mathbf{F}_M^{\mathcal{I}}$ is a $L \times L$ matrix formed by selecting the first L columns of $\mathbf{F}_M$ with the rows indexed by $\mathcal{I}$. From (2.42), the CIR can be estimated as

$$\widehat{\mathbf{h}}_0 = \frac{1}{\sqrt{M}}(\mathbf{F}_M^{\mathcal{I}})^{-1}\boldsymbol{\lambda}^{\mathcal{I}}. \tag{2.43}$$

It is worth noting that the indices in $\mathcal{I}$ have to be carefully chosen. The optimum structure and the one considered in the standards consists of equally spaced subcarrier indices $\mathcal{I}$ [49–51]. In the special case where L is a divisor of M, since the term $\sqrt{M}\mathbf{F}_M^{\mathcal{I}}$ becomes the L-point DFT matrix, i.e., $\sqrt{M}\mathbf{F}_M^{\mathcal{I}} = \sqrt{L}\mathbf{F}_L$, (2.43) can be simplified as

$$\widehat{\mathbf{h}}_0 = \frac{1}{\sqrt{L}}\mathbf{F}_L^{\mathrm{H}}\boldsymbol{\lambda}^{\mathcal{I}}. \tag{2.44}$$

2.2.1.2 LTV channel

In the case of LTV channels, the elements of $\mathbf{H}$ vary according to the Doppler shift of each path, i.e., $\mathbf{H}$ is no longer a Toeplitz matrix. Hence, the OFDM equivalent channel loses the scaling property. Furthermore, it can be observed that the LTV channel causes severe ICI, affecting the data detection and channel estimation [52]. A second aspect of LTV channels is the frequency at which the channel needs to be estimated, which significantly differs from LTI channels, where a single channel estimate suffices for an entire transmission frame. Due to the quick variations of the channel, each channel estimate quickly becomes outdated, and the channel must be estimated multiple times within the same frame.

To better understand the effect of LTV channels in OFDM, it is helpful to examine the equivalent channel of an OFDM frame. Consider an OFDM frame, where N symbols with M subcarriers each are transmitted through an LTV channel. Let the $M \times N$ matrix $\mathbf{X}$ represent the transmitted data signal. Without any modifications from the LTI case, modulation is performed with an IDFT matrix followed by the CP addition matrix, as follows

$$\mathbf{S} = \mathbf{A}_{\mathrm{CP}}\mathbf{F}_M^{\mathrm{H}}\mathbf{X}, \tag{2.45}$$

where each column of $\mathbf{S}$ represents an OFDM symbol.

To prepare for transmission, the signal undergoes parallel-to-serial conversion, resulting in $\mathbf{s} = \mathrm{vec}\{\mathbf{S}\} = [\mathbf{s}_0^{\mathrm{T}}, \ldots, \mathbf{s}_{N-1}^{\mathrm{T}}]^{\mathrm{T}}$, where $\mathbf{s}_n$ represents the n^{th} column of $\mathbf{S}$. Alternatively, the transmitted signal can be represented in vectorized form as

$$\mathbf{s} = (\mathbf{I}_N \otimes \mathbf{A}_{\mathrm{CP}}\mathbf{F}_M^{\mathrm{H}})\mathbf{x}. \tag{2.46}$$

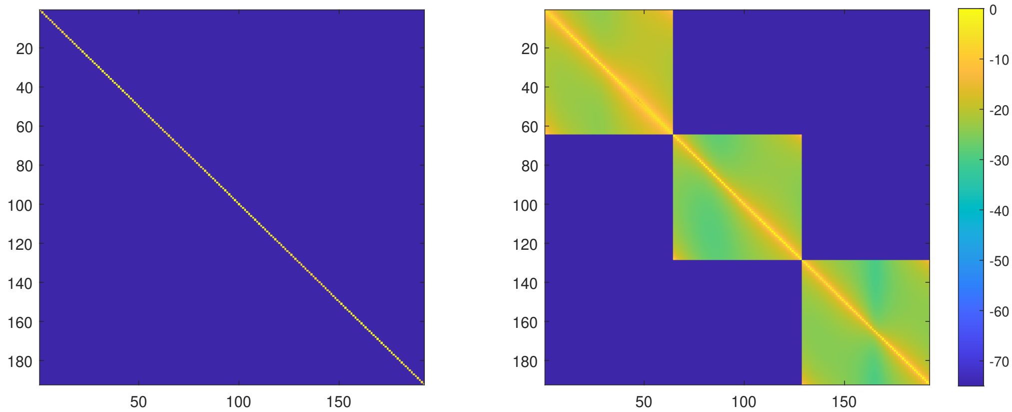

Fig. 2.5 Matrix $\mathbf{H}_{\text{eq}}^{\text{OFDM}}$ in LTI (left) and LTV (right) scenarios for $M = 128$.

This way, the above equation can be directly substituted in (2.8). Finally, performing demodulation in the same fashion results in the OFDM frame equivalent channel

$$\mathbf{y} = (\mathbf{I}_N \otimes \mathbf{F}_M \mathbf{R}_{\text{CP}})\mathbf{H}(\mathbf{I}_N \otimes \mathbf{A}_{\text{CP}} \mathbf{F}_M^{\text{H}})\mathbf{x} = \mathbf{H}_{\text{eq}}^{\text{OFDM}} \mathbf{x}. \tag{2.47}$$

The following example shows two different equivalent OFDM channels, one under LTI channels and the second under LTV channels.

Example 2-2

Consider an OFDM frame with $N = 3$ symbols and $M = 64$ subcarriers. The subcarrier spacing is $\Delta F = 15$ kHz, which translates into a symbol duration of approximately $T = 0.067$ ms. In the case of an LTV channel, the maximum Doppler frequency of 2.7 kHz is considered, i.e., the transmitter moves at a speed of 500 km/h.

Figure 2.5 shows the structure of $\mathbf{H}_{\text{eq}}^{\text{OFDM}}$ for LTI channels (left) and LTV channels (right). One can notice that the LTI equivalent matrix is a diagonal matrix. This is while the LTV channel matrix contains significant elements on its off-diagonals, representing the ICI. The ICI is disruptive in data detection and is impossible to capture by conventional channel estimation methods.

As mentioned previously, the channel variations within each OFDM symbol can be alleviated by reducing the duration of the symbol T. Naturally, the 4G and 5G standards [44, 45] consider larger subcarrier spacings Δf to deal with time-varying channels. However, the CP duration in each symbol must be at least the maximum delay spread of the channel. Hence, when shortening the OFDM symbol, the CP becomes a bottleneck leading to significant efficiency loss [29, 53–56].

Furthermore, the frequency at which the channel has to be estimated also increases significantly. In the previous section, it was shown that the channel can be approximated as LTI when within the coherence time. The coherence time is defined by a high time correlation of the channel at two different time instances. Table 2.1 shows the channel correlation at three different time windows: half a symbol duration, one symbol, and two symbols. The correlation values indicate that even after a single OFDM symbol, the channel undergoes significant changes, necessitating a new channel estimate. In other words, a CIR needs to be estimated at each OFDM symbol, significantly increasing the system overhead.

Table 2.1 Channel correlation for maximum Doppler of 2.7 kHz.

	$t = \frac{T}{2}$	$t = T$	$t = 2T$
$c_{\text{time}}(t)$	0.92	0.7	0.06

Summary of challenges:

- OFDM in LTV channels loses one of its main benefits, the single-tap equivalent channel. The LTV equivalent OFDM channels suffer from severe ICI.
- In high Doppler scenarios, OFDM systems require a significantly larger overhead for channel estimation.

To tackle these challenges, a novel joint channel estimation and equalization technique for massive MIMO is proposed in Chapter 3. This technique requires only one pilot subcarrier per user in LTI channels. For LTV channels, this technique can track the channel variations using data as virtual pilots. Consequently, the pilot overhead for OFDM-based massive MIMO systems is significantly reduced with this method.

2.2.2 Massive MIMO

Massive MIMO technology was first introduced in [16] and rapidly became the mainstream technology of modern communication systems. Massive MIMO allows multiple users to reuse the same time-frequency resources and each user's signal can be distinguished by its own channel response through linear combining methods. This can be achieved due to the *channel hardening* and *asymptotically favorable propagation* effects [17] present in most propagation environments.

To describe these two effects, consider a scenario where K users are transmitting a signal to a BS with Q receive antennas. The transmitted signals are kept within a time-frequency window in which the channel can be considered frequency flat and time-invariant. In other words, the effect of the channel is reduced into a constant scaling factor of the samples. Since all the users share the same time-frequency resources, the received signal at a given antenna q for any transmitted discrete sample s can be described as

$$r_q = \sum_{k=0}^{K-1} h_{k,q} s_k + \eta_q, \tag{2.48}$$

where $h_{k,q}$ denotes the channel from user k to antenna q, s_k the transmitted signal from user k, and η_q the additive white Gaussian noise (AWGN) at antenna q. To pave the way for future derivations, the received samples can be represented in the space domain $\overline{\mathbf{r}} = [r_0, \dots, r_{Q-1}]^{\mathrm{T}}$, a vector containing the received samples at all the BS antennas. The channel from each user and the noise term at each receive antenna can be represented in the same way, i.e., $\overline{\mathbf{h}}_k = [h_{k,0}, \dots, h_{k,Q-1}]^{\mathrm{T}}$ and $\overline{\boldsymbol{\eta}} = [\eta_0, \dots, \eta_{Q-1}]^{\mathrm{T}}$, respectively. Thus, $\overline{\mathbf{r}}$ can be represented as

$$\overline{\mathbf{r}} = \sum_{k=0}^{K-1} \overline{\mathbf{h}}_k s_k + \overline{\boldsymbol{\eta}}. \tag{2.49}$$

The *channel hardening* effect can be seen as an extension of the US effect to multiple receive antennas. *Channel hardening* occurs when multi-path arrivals from different antennas undergo uncorrelated scattering. In other words, $\mathbb{E}\{{h_{k,q}}^* h_{k,q'}\} = 0, \forall q \neq q'$, and consequently

$$\frac{\overline{\mathbf{h}}_k^{\mathrm{H}} \overline{\mathbf{h}}_k}{Q} \to 1, \text{ as } Q \to \infty, \forall k. \tag{2.50}$$

Furthermore, *asymptotically favorable propagation* assumes that the multi-path arrival of different user signals is also uncorrelated. In other words, $\mathbb{E}\{{h_{k,q}}^* h_{k',q}\} = 0, \forall k \neq k'$, and consequently

$$\frac{\overline{\mathbf{h}}_k^{\mathrm{H}} \overline{\mathbf{h}}_{k'}}{Q} \to 0, \text{ as } Q \to \infty, \text{ for } k \neq k'. \tag{2.51}$$

These effects play an important role in channel equalization in massive MIMO. Noticeably, as the number of BS antennas grows large, the signal from any user k can be singled out from (2.49) with

$$\frac{\overline{\mathbf{h}}_k^{\mathrm{H}}\overline{\mathbf{r}}_\ell}{Q} = \frac{1}{Q}\sum_{k'=0}^{K-1}\overline{\mathbf{h}}_k^{\mathrm{H}}\overline{\mathbf{h}}_{k'}s_{k'}[\ell] + \overline{\mathbf{h}}_k^{\mathrm{H}}\overline{\boldsymbol{\eta}}_\ell \to s_k[\ell], \text{ as } Q \to \infty. \tag{2.52}$$

The above effects are commonly termed spatial diversity since the benefits are achieved through the diversity of different receive antenna channels. In order to take full advantage of spatial diversity, the following challenges to the system should be considered.

- Equation (2.48) considers the limiting assumption of a single-tap channel, where channel hardening is straightforward. In cases where the channel is not single-tap, channel hardening can still be achieved through specific techniques, such as time reversal, though these methods involve increased complexity [29].
- Performing (2.52) is only possible when the channel is known. Hence, channel estimation is of utmost importance in massive MIMO.
- Equations (2.50) and (2.51) are result of an unlimited number of antennas. However, with a sufficient number of antennas the same results can be obtained with a small amount of interference, negligible to the system. To reduce the required number of antennas, additional steps can be taken to reduce the interference, e.g., minimum mean square error (MMSE) combining [57, 58].

2.2.2.1 OFDM-based Massive MIMO in LTI Channels

The benefits of massive MIMO are fully depicted in an OFDM-based massive MIMO system. As shown in Section 2.2.1, OFDM has a single tap equivalent channel, one of the requirements for taking advantage of channel hardening. Furthermore, estimating LTI channels in the frequency domain requires less pilot overhead than in the time domain. In this subsection, it is shown how each user's channel to each antenna can be estimated and how MMSE combining can used to estimate each user's data.

Consider the uplink (UL) of a single-cell massive MIMO system operating in the time-division duplexing (TDD) mode, where K single antenna users communicate with a BS with Q antennas. Each user modulates its data with OFDM, where each frame consists of N symbols with M subcarriers. The number of symbols $N \geq K$ is designed to be at least equal to the number of users. Thus, a given user k transmits the time-frequency symbols $\mathbf{X}_k \in \mathbb{C}^{M\times N}$. From (2.41), the $M \times N$ matrix representing the received signal from all the users at a given BS antenna q is given as

$$\mathbf{Y}_q = \sum_{k=0}^{K-1} \mathrm{diag}\{\boldsymbol{\lambda}_{\mathrm{k,q}}\}\mathbf{X}_{\mathrm{k}} + \mathbf{W}_{\mathrm{q}}, \tag{2.53}$$

where $\boldsymbol{\lambda}_{k,q}$ is the CFR from user k to BS antenna q and $\mathbf{W}_q$ includes the complex AWGN in the frequency domain, with the variance σ_w^2, i.e., $[\mathbf{W}_q]_{m,n} \sim \mathcal{CN}(0, \sigma_w^2)$.

The received signals are rearranged into the space-time representation to pave the way toward the derivations in the following sections. By stacking the received samples at a given subcarrier m, i.e., the m^{th} row of $\mathbf{Y}_q$ from all the Q receive antennas, the $Q \times N$ space-time matrix $\overline{\mathbf{Y}}_m$ is obtained. Thus, the input-output relationship for a given subcarrier m across all the antennas can be represented as

$$\overline{\mathbf{Y}}_m = \overline{\boldsymbol{\Lambda}}_m \overline{\mathbf{X}}_m + \overline{\mathbf{W}}_m, \tag{2.54}$$

where the elements of the matrices $\overline{\boldsymbol{\Lambda}}_m \in \mathbb{C}^{Q\times K}$, $\overline{\mathbf{X}}_m \in \mathbb{C}^{K\times N}$ and $\overline{\mathbf{W}}_m \in \mathbb{C}^{Q\times N}$ are given by $[\overline{\boldsymbol{\Lambda}}_m]_{q,k} = \lambda_{q,k}[m]$, $[\overline{\mathbf{X}}_m]_{k,n} = [\mathbf{X}^k]_{m,n}$ and $[\overline{\mathbf{W}}_m]_{q,n} = [\mathbf{W}_q]_{m,n}$, respectively.

At the channel sounding stage, each user transmits a pilot sequence with the length $N_{\mathrm{p}} \geq K$ over different time slots on a given subcarrier allocated to pilot symbols [17]. The pilot sequence of length N_{p} for a given user k at a given subcarrier m, $\overline{\mathbf{p}}_m^k$, is chosen from a pilot book $\overline{\mathbf{P}}_m = [\overline{\mathbf{p}}_m^0, \overline{\mathbf{p}}_m^1, \ldots, \overline{\mathbf{p}}_m^{K-1}]^{\mathrm{T}}$ that satisfies the orthogonality property $\overline{\mathbf{P}}_m \overline{\mathbf{P}}_m^{\mathrm{H}} = N_{\mathrm{p}}\mathbf{I}_K$, [59]. Most commonly, a pilot book where each $\overline{\mathbf{p}}_m^k$ is obtained from k cyclic shifts of the Zadoff-Chu (ZC) root sequence of length N_{p} is considered. Using (2.54), the received pilots from all the users at subcarrier m can be represented as $\overline{\mathbf{Y}}_m = \overline{\boldsymbol{\Lambda}}_m \overline{\mathbf{P}}_m + \overline{\mathbf{W}}_m$. Consequently, the channel response for all the users at a given subcarrier m can be estimated as

$$\widehat{\overline{\boldsymbol{\Lambda}}}_m = \frac{1}{N_{\mathrm{p}}} \overline{\mathbf{Y}}_m \overline{\mathbf{P}}_m^{\mathrm{H}} = \overline{\boldsymbol{\Lambda}}_m + \frac{1}{N_{\mathrm{p}}} \overline{\mathbf{W}}_m \overline{\mathbf{P}}_m^{\mathrm{H}} \triangleq \overline{\boldsymbol{\Lambda}}_m + \widetilde{\mathbf{W}}_m, \tag{2.55}$$

where $\widetilde{\mathbf{W}}_m = \frac{1}{N_{\mathrm{p}}} \overline{\mathbf{W}}_m \overline{\mathbf{P}}_m^{\mathrm{H}}$.

To estimate the CFR, it was shown previously that it suffices to estimate $\boldsymbol{\lambda}_{k,q}^{\mathcal{I}}$ [47]. Hence, each user transmits its pilot sequence $\overline{\mathbf{p}}_m^k$ only at the subcarriers within set $\mathcal{I}$, while the remaining subcarriers are allocated for data transmission. Therefore, the channel estimation process requires a minimum of LK pilots.

Once the channel is estimated, the transmit data symbols of all users can be estimated with linear combining techniques such as maximum ratio combining (MRC)

[16]

$$\widehat{\mathbf{X}}_m^{\mathrm{MRC}} = \mathbf{\Gamma}_m^{-1}\widehat{\mathbf{\Lambda}}_m^{\mathrm{H}}\overline{\mathbf{Y}}_m^{\mathrm{d}} = \mathbf{\Gamma}_m^{-1}\widehat{\mathbf{\Lambda}}_m^{\mathrm{H}}(\overline{\mathbf{\Lambda}}_m\overline{\mathbf{D}}_m + \mathbf{W}_m^{\mathrm{d}}), \tag{2.56}$$

where $\mathbf{\Gamma}_m$ is a $K \times K$ diagonal matrix, with the k^{th} diagonal element given by $\frac{1}{Q}\sum_{q=0}^{Q-1}|\lambda_{q,k}[m]|^2$, considered solely to normalize the amplitude of the equalizer output. In the literature, the effect of channel estimation noise is often neglected and the diagonal elements of $\mathbf{\Gamma}_m$ are formed from the diagonal elements of $\overline{\mathbf{\Lambda}}_m^{\mathrm{H}}\overline{\mathbf{\Lambda}}_m$, i.e., the norm squared of the channel vector for each user at a given subcarrier m. However, in the presence of channel estimation errors, using (2.55), the normalization factors on the elements of $\overline{\mathbf{\Lambda}}_m^{\mathrm{H}}\overline{\mathbf{\Lambda}}_m$ are obtained as the diagonal elements of

$$\widehat{\mathbf{\Lambda}}_m^{\mathrm{H}}\widehat{\mathbf{\Lambda}}_m = \widehat{\mathbf{\Lambda}}_m^{\mathrm{H}}\overline{\mathbf{\Lambda}}_m + \overline{\mathbf{\Lambda}}_m^{\mathrm{H}}\widetilde{\mathbf{W}}_m + \frac{1}{N_{\mathrm{p}}^2}\overline{\mathbf{P}}_m(\overline{\mathbf{W}}_m^{\mathrm{p}})^{\mathrm{H}}\overline{\mathbf{W}}_m^{\mathrm{p}}\overline{\mathbf{P}}_m^{\mathrm{H}}. \tag{2.57}$$

The term $\overline{\mathbf{\Lambda}}_m^{\mathrm{H}}\widetilde{\mathbf{W}}_m$ tends to zero in the asymptotic regime, as $Q \to \infty$, since the channel path gain and noise are independent. However, the same is not true for $(\overline{\mathbf{W}}_m^{\mathrm{p}})^{\mathrm{H}}\overline{\mathbf{W}}_m^{\mathrm{p}}$. As $\overline{\mathbf{W}}_m^{\mathrm{p}}$ represents the AWGN, in the asymptotic regime, the following property takes place

$$\left(\overline{\mathbf{\Lambda}}_m^{\mathrm{H}}\widetilde{\mathbf{W}}_m + \frac{1}{N_{\mathrm{p}}^2}\overline{\mathbf{P}}_m(\overline{\mathbf{W}}_m^{\mathrm{p}})^{\mathrm{H}}\overline{\mathbf{W}}_m^{\mathrm{p}}\overline{\mathbf{P}}_m^{\mathrm{H}}\right) \to \frac{Q\sigma_w^2}{N_{\mathrm{p}}^2}\overline{\mathbf{P}}_m\overline{\mathbf{P}}_m^{\mathrm{H}}. \tag{2.58}$$

Hence, taking a similar approach to [60], the channel estimation noise can be mitigated by subtracting (2.58) from the normalization factor, i.e., $\mathbf{\Gamma}_m$ is formed from the diagonal elements of $(\widehat{\mathbf{\Lambda}}_m^{\mathrm{H}}\widehat{\mathbf{\Lambda}}_m - \frac{Q\sigma_w^2}{N_{\mathrm{p}}^2}\overline{\mathbf{P}}_m\overline{\mathbf{P}}_m^{\mathrm{H}})$.

Due to the *channel hardening* effect in (2.50) and *asymptotically favorable propagation* effect in (2.51), the following property appears in the asymptotic regime, i.e., as $Q \to \infty$,

$$\frac{\overline{\boldsymbol{\lambda}}_{m,k}^{\mathrm{H}}\overline{\boldsymbol{\lambda}}_{m,k'}}{Q} \to \begin{cases} \mathbb{E}\{|\overline{\lambda}_{m,k}[q]|^2\} = 1 & \text{if } k = k' \\ 0 & \text{otherwise} \end{cases}, \tag{2.59}$$

where $\overline{\boldsymbol{\lambda}}_{m,k}$, of length Q, represents the k^{th} column of $\overline{\mathbf{\Lambda}}_m$. Therefore, as $Q \to \infty$, $\mathbf{\Gamma}_m^{-1}\widehat{\mathbf{\Lambda}}_m^{\mathrm{H}}\overline{\mathbf{\Lambda}}_m \to \mathbf{I}_K$.

In practical systems, the number of BS antennas is limited, and the off-diagonal elements of $\widehat{\mathbf{\Lambda}}_m^{\mathrm{H}}\overline{\mathbf{\Lambda}}_m$, in (2.56), lead to a significant amount of interference. Thus, MMSE combining provides an improved performance compared to MRC with

$$\widehat{\mathbf{X}}_m^{\mathrm{MMSE}} = \mathbf{\Phi}_m^{\mathrm{MMSE}}\overline{\mathbf{Y}}_m, \tag{2.60}$$

where $\boldsymbol{\Phi}_m^{\mathrm{MMSE}} \triangleq (\widehat{\boldsymbol{\Lambda}}_m^{\mathrm{H}} \widehat{\boldsymbol{\Lambda}}_m - \frac{Q\sigma_w^2}{N_{\mathrm{p}}^2} \overline{\mathbf{P}}_m \overline{\mathbf{P}}_m^{\mathrm{H}} + \sigma_w^2 \mathbf{I}_K)^{-1} \widehat{\boldsymbol{\Lambda}}_m^{\mathrm{H}}$.

2.2.2.2 Massive MIMO in LTV Channels

Massive MIMO systems suffer severely in high mobility scenarios. In OFDM-based massive MIMO systems, the Doppler breaks the orthogonality of OFDM, making different subcarriers interfere with each other. Therefore, the channel estimation and equalization processes become corrupted with ICI, significantly degrading systems performance. Furthermore, in LTV channels, the channel's time-variability necessitates frequent updates to channel state information (CSI). This leads to a large overhead allocated for channel estimation from each user, severely affecting the system's spectral efficiency.

Finally, it is important to note that spatial diversity relies heavily on the uncorrelated channels between the users and receive antennas. The correlation of the channel is largely influenced by the architecture of the massive MIMO system [61]. Antennas can be intentionally designed to increase the correlation between channels, favoring angular diversity rather than spatial diversity [61].

In such systems, all receive antennas observe the same channel from each user, with the only variation being the angle of arrival, which is determined by the antenna array design. This approach is particularly advantageous for channel estimation, as angle diversity allows for estimating the channel parameters with reduced overhead, as shown in [62–65]. However, the study of angular diversity is beyond the scope of this thesis. The focus of this thesis is on massive MIMO systems with uncorrelated channels and alternative waveforms to the existing ones in massive MIMO literature.

Summary of challenges:

- In LTV channels, massive MIMO systems require novel approaches to harness the full potential of spatial diversity.
- The substantial overhead in LTV channel estimation is further amplified by the number of users in the system. As a result, spectral efficiency becomes a major concern in massive MIMO systems, highlighting the need for novel channel estimation techniques.

A novel channel equalization technique for massive MIMO that takes advantage of the spatial diversity to deal with the channel variations is proposed in Chapter

4. Furthermore, the large overhead issue is addressed in Chapter 5, where a novel split pilot channel estimation method is proposed. This method reduces by half the required delay zero-guard compared to conventional methods.

2.3 OTFS Modulation

While OFDM has been the technology of choice for 4G and 5G systems, its high sensitivity to Doppler effects due to the time variations of the channel motivates the need for a more robust waveform. Thus, a new waveform called OTFS has recently emerged, [11]. OTFS has a novel and fresh approach to waveform design as it deploys DD instead of time-frequency domain for data transmission. An important aspect of placing data symbols in the DD domain is that the response in this domain relating the input to the output of the channel is sparse and time-invariant, [11, 18, 66]. Hence, OTFS requires much lower training overheads and much slower channel tracking requirements than OFDM. Due to these benefits, OTFS has been proven to outperform OFDM in many aspects [19, 67].

In the original form of OTFS [11], the transmitted data is modulated in two steps. The first step, known as the OTFS transform, involves mapping the DD data into the time-frequency domain using inverse SFFT (ISFFT), followed by the application of a windowing function. The second step is the Heisenberg transform, where the time-frequency signal is converted into the delay-time domain transmit signal $s(t)$ using a pulse-shaping waveform. At the receiver, demodulation begins with the Wigner transform, which is the inverse of the Heisenberg transform, and is followed by the SFFT.

Consider a sequence of MN quadrature amplitude modulation (QAM) symbols transmitted through OTFS modulation. The transmitted symbols are first mapped in a $M \times N$ DD grid $\mathbf{X}_{\mathrm{DD}}$. Then, the DD data is brought to the time-frequency domain, represented by the $M \times N$ matrix $\mathbf{X}_{TF}$, through an ISFFT and scaled by a $M \times N$ windowing function $\mathbf{W}_{\mathrm{tx}}$. Noticeably, ISFFT can be implemented with two DFT matrices, therefore, the data at frequency slot m and time slot n is obtained from

$$[\mathbf{X}_{TF}]_{m,n} = [\mathbf{W}_{\mathrm{tx}}]_{m,n}[\mathbf{F}_M \mathbf{X}_{\mathrm{DD}} \mathbf{F}_N^{\mathrm{H}}]_{m,n}. \tag{2.61}$$

Finally, the transmit signal $s(t)$ is obtained after the Heisenberg transform with the pulse shaping function $g_{\text{tx}}(t)$, i.e.,

$$s(t) = \sum_{m=0}^{M-1} \sum_{n=0}^{N-1} [\mathbf{X}_{TF}]_{m,n} g_{\text{tx}}(t - nT) e^{j2\pi m \Delta f (t-nT)}, \tag{2.62}$$

where T and Δf represent the time and frequency spacing on the time-frequency grid.

After transmitting the signal through the channel, the received signal, in the absence of noise, is given as

$$r(t) = \sum_{p=1}^{P-1} \alpha_p e^{2j\pi \upsilon_p t} s(t - \tau_p) + . \tag{2.63}$$

The demodulation process starts with the Wigner transform to obtain the time-frequency data

$$[\mathbf{Y}_{TF}]_{m,n} = \int g_{rx}^*(t-\tau) r(t) e^{-j2\pi\upsilon(t-\tau)} dt|_{\tau=nT, \upsilon=m\Delta f}. \tag{2.64}$$

The Wigner transform pulse shapes the received signal with the function $g_{rx}^*(t)$ followed by the Fourier transform to bring the signal to the time-frequency domain. The signal is then sampled in the time-frequency lattice, i.e., at the sample points $\tau = nT$ and $\upsilon = m\Delta f$ for $n = 0, \ldots, N-1$ and $m = 0, \ldots, M-1$. This operation reverses the Heisenberg transform.

The last demodulation step consists of the receiver windowing $\mathbf{W}_{\text{rx}}$ followed by the SFFT operation, resulting in

$$[\mathbf{Y}_{DD}]_{m,n} = [\mathbf{W}_{\text{rx}}]_{m,n} [\mathbf{F}_M^{\text{H}} \mathbf{Y}_{TF} \mathbf{F}_N]_{m,n}. \tag{2.65}$$

One may notice from (2.65) the similarities of the Heisenberg transform and OFDM transform. Indeed, the Heisenberg transform is a generalized representation of OFDM transform, where the former is obtained by setting T, Δf and the pulse-shaping function $g_{\text{tx}}(t)$ as the symbol duration, subcarrier spacing, and sinc function, respectively. This is an interesting benefit of OTFS since it can be implemented on top of the existing OFDM structures.

Building on this idea, the authors in [23, 68] presented a low complexity OFDM-based OTFS modulator. By considering a rectangle windowing and an OFDM modulator with CP length of $L-1$ similar to (2.40), the OTFS transmitted signal matrix can be obtained as

$$\mathbf{S} = \mathbf{A}_{\mathrm{CP}}\mathbf{F}_M^{\mathrm{H}}\mathbf{F}_M\mathbf{X}_{\mathrm{DD}}\mathbf{F}_N^{\mathrm{H}} = \mathbf{A}_{\mathrm{CP}}\mathbf{X}_{\mathrm{DD}}\mathbf{F}_N^{\mathrm{H}}. \tag{2.66}$$

In other words, OTFS modulation can be performed with a single IDFT matrix. The same is true at the receiver side, where OTFS demodulation can be performed with a DFT matrix. Before transmission, the signal undergoes parallel-to-serial conversion, resulting in $\mathbf{s} = [\mathbf{s}_0^{\mathrm{T}}, \ldots, \mathbf{s}_{N-1}^{\mathrm{T}}]^{\mathrm{T}}$, where $\mathbf{s}_n$ represents the n^{th} column of $\mathbf{S}$. Hence, the OTFS transmit signal in vectorized form is given as

$$\mathbf{s} = (\mathbf{F}_N^{\mathrm{H}} \otimes \mathbf{A}_{\mathrm{CP}})\mathbf{x}. \tag{2.67}$$

The signal is then transmitted through the LTV channel and demodulated at the receiver. This process results in the received signal

$$\mathbf{y} = (\mathbf{F}_N \otimes \mathbf{R}_{\mathrm{CP}})\mathbf{H}(\mathbf{F}_N^{\mathrm{H}} \otimes \mathbf{A}_{\mathrm{CP}})\mathbf{x}. \tag{2.68}$$

In preparation for future discussions regarding CP in OTFS systems in Chapter 4, the OTFS equivalent channel matrix is presented with the modulation matrices and CP matrices, namely

$$\begin{aligned}\mathbf{H}_{\mathrm{eq}}^{\mathrm{OTFS}} &= (\mathbf{F}_N \otimes \mathbf{R}_{\mathrm{CP}})\mathbf{H}(\mathbf{F}_N^{\mathrm{H}} \otimes \mathbf{A}_{\mathrm{CP}}) \\ &= (\mathbf{F}_N \otimes \mathbf{I}_M)(\mathbf{I}_N \otimes \mathbf{R}_{\mathrm{CP}})\mathbf{H}(\mathbf{I}_N \otimes \mathbf{A}_{\mathrm{CP}})(\mathbf{F}_N^{\mathrm{H}} \otimes \mathbf{I}_M).\end{aligned} \tag{2.69}$$

From the above OTFS equivalent channel equation, many authors in the literature have proposed approximations in the channel that lead to interesting properties in the OTFS equivalent channel [10, 23, 26]. These approximations are described in detail in the following, highlighting their main benefits.

A. Effect of Integer Delay and Doppler Shifts

In equation (2.6), the concept of integer delays was introduced. This concept can also be extended to Doppler shifts [10]. Consider an OTFS frame of size $M \times N$ with the modulated signal as

$$x_{DT}[m + Mn] = \sum_{n'=0}^{N-1} [X_{DD}]_{m,n'} e^{\frac{2j\pi nn'}{N}}, \tag{2.70}$$

and the received DD domain signal as

$$[Y_{DD}]_{m,n} = \sum_{n'=0}^{N-1} r[m + Mn']e^{\frac{-2j\pi nn'}{N}}, \tag{2.71}$$

for $n = 0, \ldots, N-1$ and $m = 0, \ldots, M-1$.

Substituting the above equations in (2.6), the received DD domain signal becomes

$$\begin{aligned}[Y_{DD}]_{m,n} = \sum_{\substack{n_1=0\\n_2=0\\n_3=0}}^{N-1} \sum_{p=0}^{P-1} \sum_{m_1=0}^{M-1} \alpha_p e^{2j\pi\upsilon_p(m+Mn_1)T_s} e^{\frac{-2j\pi nn_1}{N}} e^{\frac{2j\pi n_2 n_3}{N}} \times \\ [X_{DD}]_{m_1,n_3} \mathrm{sinc}[(m + Mn_1) - (m_1 + Mn_2) - \frac{\tau_p}{T_s}].\end{aligned} \tag{2.72}$$

Considering the case of integer delay $\ell_p = \frac{\tau_p}{T_s}$, the sinc term assumes the following values

$$\mathrm{sinc}[(m + Mn_1) - (m_1 + Mn_2) - \ell_p] = \begin{cases} 1 & \text{if } m_1 = m - \ell_p \text{ and } n_1 = n_2 \\ 0 & \text{otherwise} \end{cases}. \tag{2.73}$$

This way, (2.72) is simplified as

$$[Y_{DD}]_{m,n} = \sum_{\substack{n_1=0\\n_3=0}}^{N-1} \sum_{p=0}^{P-1} \alpha_p e^{2j\pi\upsilon_p mT_s} e^{2j\pi n_1 \frac{((\upsilon_p MT_s N)-(n)+(n_3))}{N}} [X_{DD}]_{m-\ell_p,n_3}. \tag{2.74}$$

If the Doppler shifts at each path υ_p are restricted in such a way that $\kappa_p = \upsilon_p MT_s N$ results in only integer values, then (2.72) can be further simplified as

$$[Y_{DD}]_{m,n} = \sum_{p=0}^{P-1} \alpha_p e^{2j\pi\upsilon_p mT_s} [X_{DD}]_{m-\ell_p,n-\kappa_p}. \tag{2.75}$$

In summary, the assumption of integer delay and Doppler limits the delay and Doppler shifts to integer values of ℓ_p and κ_p for

$$\tau_p = \ell_p T_s \text{ and } \upsilon_p = \frac{\kappa_p}{MT_s N}. \tag{2.76}$$

Furthermore, the maximum delay and Doppler becomes limited to

$$\tau_{\max} = \ell_{\max} T_s \text{ and } \upsilon_{\max} = \frac{\kappa_{\max}}{MT_s N}. \tag{2.77}$$

This representation has two main benefits: the equivalent channel becomes significantly simplified, and the effect of the channel is contained within $[0, \ell_{\max}]$ along the delay dimension and $[-\kappa_{\max}, \kappa_{\max}]$ along Doppler dimension. These benefits are further explained in Subsection 2.3.0.1.

A. 2D circular convolution

In high mobility scenarios, the Coherence time of the channel is significantly shortened [69]. Therefore, it becomes impossible to fit a transmission frame within the coherence time to approximate an LTI channel. However, one may argue that the duration of each time slot of OTFS can be designed to be within the coherence time. Consider the approximation where the channel is invariant for every time slot, i.e., every $M + M_{\mathrm{CP}}$ data sample, or every column of $\mathbf{X}$. Under this condition, $(\mathbf{I}_N \otimes \mathbf{R}_{\mathrm{CP}})\mathbf{H}(\mathbf{I}_N \otimes \mathbf{A}_{\mathrm{CP}})$ becomes a block diagonal matrix with its diagonal composed of blocks of $M \times M$ circulant submatrices. As a result, $\mathbf{H}_{\mathrm{eq}}^{\mathrm{OTFS}}$ becomes a block circulant matrix with each block composed of a $M \times M$ circulant submatrix, i.e., a block circulant with circulant blocks (BCCB) matrix [70]. An example structure of the BCCB channel matrix $\mathbf{H}_{\mathrm{eq}}^{\mathrm{OTFS}}$ is shown in Fig. 2.6 (left). Consequently, using the property of a BCCB matrices, the effect of the channel can be expressed as a 2D circular convolution, i.e.,

$$\mathbf{Y} = \boldsymbol{\mathcal{H}}_{\mathrm{BC}} \overset{\mathrm{2D}}{\circledast} \mathbf{X}, \tag{2.78}$$

where $\mathbf{Y}$ represents the received signal $\mathbf{y}$ concatenated into a $M \times N$ matrix, and $\boldsymbol{\mathcal{H}}_{\mathrm{BC}}$ is formed by concatenating the first column of $\mathbf{H}_{\mathrm{eq}}^{\mathrm{OTFS}}$ into a $M \times N$ matrix. An example structure of $\boldsymbol{\mathcal{H}}_{\mathrm{BC}}$ is shown in Fig. 2.6 (right).

This property is crucial for channel estimation in OTFS. Under this assumption, it becomes only necessary to estimate $\boldsymbol{\mathcal{H}}_{\mathrm{BC}}$, an $M \times N$ matrix, i.e., only a single column of $\mathbf{H}_{\mathrm{eq}}^{\mathrm{OTFS}}$, instead of the full matrix. The following subsection describes how channel estimation can be performed using this approximation, along with additional techniques to reduce the error that arises from it. Furthermore, the simplified equivalent channel representation in 2.78 also allows for low-complexity channel equalization techniques, since $\mathbf{H}_{\mathrm{eq}}^{\mathrm{OTFS}}$ can be diagonalized in the frequency domain, as show in [71].

2.3.0.1 Channel Estimation in OTFS

The prevalent channel estimation technique in the present literature is a high-power impulse pilot embedded in the DD domain together with data symbols [10, 72], as

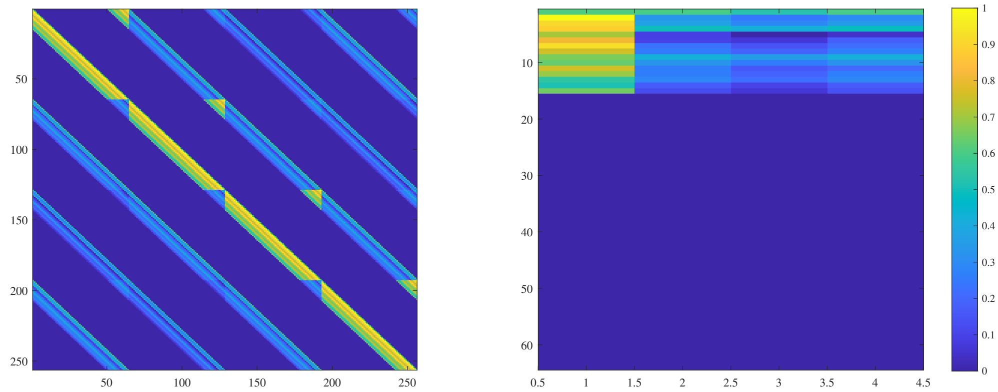

Fig. 2.6 Structure of matrices $\mathbf{H}_{\mathrm{eq}}^{\mathrm{OTFS}}$ (left) and $\boldsymbol{\mathcal{H}}_{\mathrm{BC}}$ (right).

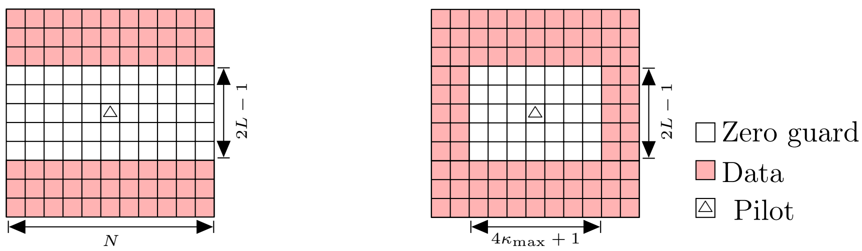

(a) Full-guard EP

(b) Reduced guard EP

Fig. 2.7 Embedded pilot structure for fractional (a) and integer (b) Doppler.

shown in Figure 2.7 (a). As shown in Section 2.1.1, the DD channel spreads the transmitted signal according to the channel's delay and Doppler shifts. Hence, to prevent the pilot and data from interfering with each other, the EP structure deploys a large zero-guard surrounding the transmitted pilot along both delay and Doppler domains, resulting in a large pilot overhead. To reduce the pilot overhead, the authors in [10] also presented a reduced guard embedded impulse pilot with the assumption of integer Doppler. Under these conditions, the Doppler spread is limited by the maximum integer Doppler $\kappa_{\max}$. Therefore, the Doppler guard can be reduced to $4\kappa_{\max} + 1$, as shown in Figure 2.7 (b).

However, the assumption of integer Doppler is unrealistic. When implemented in more practical scenarios, this approximation error leads to a significant performance loss. Therefore, alternative techniques that can reduce the pilot overhead are required. The authors in [31–33] proposed a superimposed pilot structure to remove the pilot overhead completely. This technique superimposes a high-power pilot signal over data symbols in the DD domain. The main drawback of such a pilot structure is the huge computational complexity associated with the sophisticated estimation and detection algorithms. Furthermore, superimposed pilots are susceptible to channel variations within each time slot of OTFS, requiring a super-frame solely to obtain initial estimates of the channel delay and Doppler parameters. In [34], the authors developed a BEM-based [7] joint channel estimation and detection technique for impulse pilot with reduced guard across Doppler dimension. This method consists of deploying a reduced pilot overhead and iteratively refining the estimated channel and data using detected data as virtual pilots. However, using impulse pilots has the unique benefit of not requiring matrix inversion for channel estimation.

Furthermore, the EP structure approximates the channel as time-invariant per time slot. While this is the only sensible way to perform channel estimation with impulsive pilots, the time variations of the channel can cause significant interference at the channel equalization stage. Therefore, authors in [24, 34, 73, 74] proposed an additional interpolation step to capture the full variation of the channel. Specifically, [73] proposed a spline interpolation method, whereas [24, 34, 74] proposed a BEM-based [7] technique to interpolate the channel.

The authors in [75] proposed extending the EP structure to MIMO systems. In this technique, a distinct DD region is assigned to each transmit antenna for channel estimation. Naturally, this demands a large portion of the transmission frame for channel estimation and limits the number of users that the system can accommodate. The authors in [62, 63] proposed a channel estimation technique in massive MIMO by taking advantage of the angular diversity. In the 3D DD-angle domain, the channel becomes extremely sparse, significantly reducing the overhead required for channel estimation. However, the angle domain can only be explored in scenarios without spatial diversity. Consequently, channel equalization techniques that exploit spatial diversity fail under such scenarios.

2.3.0.2 CP in OTFS

As shown in the previous sections, CP has mainly two benefits: avoiding ISI and making the channel matrix circulant. However, when the channel is time-variant, it becomes impossible to construct circulant channels. Hence, one may consider removing the CP to improve spectral efficiency. A reduced CP structure was proposed in [26], where each OTFS block utilizes only a single CP sequence, instead of a sequence per time slot. This way, the CP addition and removal matrices become

$$\overline{\mathbf{A}}_{\mathrm{CP}} = [\mathbf{G}^{\mathrm{T}}_{M_{\mathrm{CP}},MN}, \mathbf{I}_{MN}]^{\mathrm{T}} \text{ and } \overline{\mathbf{R}}_{\mathrm{CP}} = [\mathbf{0}_{MN\times M_{\mathrm{CP}}}, \mathbf{I}_{MN}] \tag{2.79}$$

And the equivalent channel becomes

$$\overline{\mathbf{H}}^{\mathrm{OTFS}}_{\mathrm{eq}} = (\mathbf{F}_N \otimes \mathbf{I}_{\mathrm{M}})\overline{\mathbf{R}}_{\mathrm{CP}}\mathbf{H}\overline{\mathbf{A}}_{\mathrm{CP}}(\mathbf{F}^{\mathrm{H}}_N \otimes \mathbf{I}_{\mathrm{M}}). \tag{2.80}$$

This structure differs slightly from the conventional method as it loses the BCCB property. However, multiple detectors that do not depend on this property implement the reduced CP structure, e.g., message passing (MP) [76, 77] and maximum likelihood (ML) [11] detectors.

The issue with large pilot overhead is dealt with in Chapters 3 and 5. Specifically, Chapter 5 proposes a novel split pilot channel estimation method for OTFS that reduces the delay guard required by half compared to the EP in [10]. Chapter 4 shows how CP can be completely removed from OTFS-based massive MIMO systems.

Summary of challenges in OTFS:

- The overhead of the existing OTFS systems is still large. This significantly impacts the spectral efficiency and latency of the system and remains a critical issue to be addressed in practical systems.
- Appending CP becomes less effective in LTV channels. Hence, alternative methods that can deal with ISI can enable CP-less transmission, improving the system's spectral efficiency.

Chapter 3

Massive MIMO with only a Single Pilot Subcarrier

Massive MIMO has brought substantial improvements to 4G and 5G systems and it continues to be a dominant technology in next-generation networks. In particular, spatial diversity and beamforming gains provided by massive MIMO have led to significant improvements in capacity, spectral efficiency, and energy efficiency compared to the previous generation networks [15, 17]. In massive MIMO, multiple users reuse the same time-frequency resources, as their signals can be distinguished based on their channel responses. Therefore, obtaining accurate CIR at each BS antenna is crucial. Conventional channel estimation methods, e.g. least squares (LS) [48, 78], rely on the transmission of pilot sequences from each user. These methods are favorable due to their low complexity. However, this comes at the expense of spectral efficiency loss.

Extensive research has been conducted to reduce the pilot overhead, see [79–83] and the references therein. For instance, (semi) blind techniques emphasize reducing the pilot length and estimating the channel by solving underdetermined systems of equations using iterative algorithms [79–81]. Alternatively, superimposed pilots share the same time-frequency resources for both data and pilot transmission. In these techniques, the channel is estimated by treating data as noise. While this can completely remove the pilot overhead, it comes at the cost of interference and extra computational load [82, 83]. Most works on massive MIMO consider a narrow band channel [17, 84]. Therefore, utilizing these channel estimation techniques for OFDM would require pilots on each subcarrier. Alternatively, pilots can be placed in equally spaced subcarriers and the CFR of subcarriers with data symbols can be estimated through interpolation methods [85, 86]. In such cases, the authors of [47] show that the number of pilot subcarriers should be at least equal to the length of the channel. However, this leads to a large overhead, as the channel length varies from 7% to 25% of the OFDM symbol duration [87]. To alleviate this issue, the authors in [47] proposed a technique that can reduce the required pilot subcarriers by 80%, however, the technique is limited to sparse channels. One important aspect of all the aforementioned methods is that the pilot length is tied to the delay spread of the channel. Hence, in order to reduce the pilot overhead, the following research question is addressed in this chapter.

Is it possible to reduce the selectivity of the channel into its known and constant correlation function to minimize the channel estimation overhead?

To address the aforementioned limitations of the existing literature, in this chapter, a technique where only one reference subcarrier is sufficient for both channel estimation and data detection in massive MIMO is proposed. This is possible by taking advantage of multiple adjacent subcarriers being within the channel's coherence bandwidth. Thus, the transmitted data over a band of subcarriers can be detected using only one reference subcarrier's channel estimate. Thereafter, the detected data symbols are considered as virtual pilots to update their corresponding channel estimates. Each updated channel estimate is then used to equalize a new band of subcarriers within the coherence bandwidth. This way, multiple estimates of the transmitted data symbols at each subcarrier can be obtained and averaged. In other words, this approach utilizes both the frequency diversity and the spatial diversity to achieve improved performance. By repeating this process in a sliding manner, all the data symbols and the CFRs can be estimated, starting from one reference pilot.

Furthermore, it is proven in this chapter that in the large antenna regime, linear combining can be performed using the channel estimate at any subcarrier. The combined signal at a subcarrier will be scaled by a coefficient, which depends on the channel PDP and frequency spacing between the subcarrier and the CFR used for combining. However, this coefficient can take very small values leading to noise enhancement. To avoid this issue, it is defined a *depth* factor for the proposed sliding technique. The depth factor is a design parameter determining how many subcarriers within each band will be equalized using the same CFR. This ensures that only large values of the aforementioned coefficient are considered. To evaluate the effectiveness of the proposed technique, its BER and signal to interference and noise ratio (SINR) performances are compared with the conventional techniques.

For 15 MHz transmission bandwidth, the existing techniques require over 70 pilot subcarriers, whereas the proposed technique reduces this overhead to only one pilot subcarrier. Moreover, the proposed technique outperforms the linear equalizers by approximately 2 dB, at high SNR, in terms of the BER performance.

3.1 Uplink of OFDM-based Massive MIMO System

Consider the UL of a single-cell massive MIMO system operating in the time-division duplex (TDD) mode. OFDM with M subcarriers is deployed as the modulation format, with the CP of length M_{CP}. M_{CP} is chosen to be larger than the channel length to avoid intersymbol interference. The BS is equipped with Q antennas and serves K single antenna users. The duration of each frame is assumed to be within the channel coherence time, including N number of OFDM time symbols in the UL. Hence, the channel remains time-invariant within each frame.

The UL transmission is divided into two phases, training and data transmission. N_{p} and N_{d} time slots are allocated to pilot and data transmission, respectively. Thus, a given user k transmits the time-frequency symbols $\mathbf{X}^k = [\mathbf{P}^k, \mathbf{D}^k]$, where $\mathbf{P}^k \in \mathbb{C}^{M\times N_{\mathrm{p}}}$ represents the pilot and $\mathbf{D}^k \in \mathbb{C}^{M\times N_{\mathrm{d}}}$ the data symbols. Hence, the OFDM transmit signal of user k is obtained as $\mathbf{S}^k = \mathbf{A}_{\mathrm{CP}}\mathbf{F}_M^{\mathrm{H}}\mathbf{X}^k$, where $\mathbf{A}_{\mathrm{CP}} = [\mathbf{G}_{\mathrm{CP}}^{\mathrm{T}}, \mathbf{I}_M]^{\mathrm{T}}$ is the CP addition matrix and the $M_{\mathrm{CP}} \times M$ matrix $\mathbf{G}_{\mathrm{CP}}$ includes the last M_{CP} rows of $\mathbf{I}_M$.

The signal is transmitted through the channel and undergoes OFDM demodulation. Thus, the received signal from all the users at a given BS antenna q is obtained as

$$\begin{aligned}\mathbf{Y}_q &= \mathbf{F}_M\mathbf{R}_{\mathrm{CP}}\sum_{k=0}^{K-1}\mathbf{H}_{q,k}\mathbf{S}^k + \mathbf{W}_q\\ &= \sum_{k=0}^{K-1}\mathrm{diag}\{\boldsymbol{\lambda}_{\mathrm{q,k}}\}\mathrm{X}^{\mathrm{k}} + \mathbf{W}_{\mathrm{q}},\end{aligned} \tag{3.1}$$

where $\mathbf{R}_{\mathrm{CP}} = [\mathbf{0}_{M\times M_{\mathrm{CP}}}, \mathbf{I}_M]$ is the CP removal matrix, $\mathbf{H}_{q,k}$ denotes the Toeplitz channel matrix realizing the linear convolution, which is formed by the CIR between user k and antenna q, i.e., $\mathbf{h}_{q,k} = [h_{q,k}[0], \ldots, h_{q,k}[L-1]]^{\mathrm{T}}$, and $\mathbf{W}_q$ includes the complex AWGN in the frequency domain, with the variance σ_w^2, i.e., $[\mathbf{W}_q]_{m,n} \sim \mathcal{CN}(0, \sigma_w^2)$. Assuming the CIR between the UEs and the BS antennas to be independent and identically distributed (i.i.d.) complex random variables with the length L, $\mathbf{h}_{q,k} \sim \mathcal{CN}(\mathbf{0}_{L\times 1}, \boldsymbol{\Sigma}_k)$ for $q = 0, \ldots, Q-1$ and $k = 0, \ldots, K-1$. $\boldsymbol{\Sigma}_k$ is a diagonal matrix with the diagonal elements formed by the PDP of the channel $\boldsymbol{\rho}_k = [\rho_k[0], \ldots, \rho_k[L-1]]^{\mathrm{T}}$, where the normalized PDP is considered, i.e., $\sum_{l=0}^{L-1} \rho_k[l] = 1$. As $M_{\mathrm{CP}} \geq L-1$, $\widetilde{\mathbf{H}}_{q,k} = \mathbf{R}_{\mathrm{CP}}\mathbf{H}_{q,k}\mathbf{A}_{\mathrm{CP}}$ is a circulant matrix, with the first column formed by the zero-padded CIR, i.e., $\widetilde{\mathbf{h}}_{q,k} = [\mathbf{h}_{q,k}^{\mathrm{T}}, \mathbf{0}_{M-L\times 1}^{\mathrm{T}}]^{\mathrm{T}}$. Hence, the channel matrix $\widetilde{\mathbf{H}}_{q,k}$ can be diagonalized by the DFT and IDFT matrices as $\mathbf{F}_M\widetilde{\mathbf{H}}_{q,k}\mathbf{F}_M^{\mathrm{H}} = \mathrm{diag}\{\boldsymbol{\lambda}_{\mathrm{q,k}}\}$, where $\boldsymbol{\lambda}_{q,k} = [\lambda_{q,k}[0], \ldots, \lambda_{q,k}[M-1]]^{\mathrm{T}}$ represents the CFR with the elements obtained as

$$\lambda_{q,k}[m] = \sqrt{M}\mathbf{f}_{M,m}^{\mathrm{T}}\widetilde{\mathbf{h}}_{q,k}. \tag{3.2}$$

To pave the way toward the derivations in the following sections, the received signals are rearranged into the space-time representation. By stacking the received samples at a given subcarrier m, i.e., the m^{th} row of $\mathbf{Y}_q$ from all the Q receive antennas, obtaining the $Q \times N$ space-time matrix $\overline{\mathbf{Y}}_m$. Thus, the input-output relationship for a given subcarrier m across all the antennas can be represented as

$$\overline{\mathbf{Y}}_m = \overline{\boldsymbol{\Lambda}}_m\overline{\mathbf{X}}_m + \overline{\mathbf{W}}_m, \tag{3.3}$$

where the elements of the matrices $\overline{\boldsymbol{\Lambda}}_m \in \mathbb{C}^{Q\times K}$, $\overline{\mathbf{X}}_m \in \mathbb{C}^{K\times N}$ and $\overline{\mathbf{W}}_m \in \mathbb{C}^{Q\times N}$ are given by $[\overline{\boldsymbol{\Lambda}}_m]_{q,k} = \lambda_{q,k}[m]$, $[\overline{\mathbf{X}}_m]_{k,n} = [\mathbf{X}^k]_{m,n}$ and $[\overline{\mathbf{W}}_m]_{q,n} = [\mathbf{W}_q]_{m,n}$, respectively.

Finally, $\overline{\mathbf{X}}_m \triangleq [\overline{\mathbf{P}}_m, \overline{\mathbf{D}}_m]$, where $\overline{\mathbf{P}}_m$ and $\overline{\mathbf{D}}_m$ represent the transmitted pilot and data symbols, respectively. Correspondingly, $\overline{\mathbf{Y}}_m \triangleq [\overline{\mathbf{Y}}_m^{\mathrm{p}}, \overline{\mathbf{Y}}_m^{\mathrm{d}}]$ and $\overline{\mathbf{W}}_m \triangleq [\overline{\mathbf{W}}_m^{\mathrm{p}}, \overline{\mathbf{W}}_m^{\mathrm{d}}]$.

3.2 Conventional Techniques for Channel Estimation and Equalization

In this section, the widely used linear pilot-based channel estimation and equalization techniques are described. In particular, LS-based channel estimation, and two linear combining techniques, namely MRC and MMSE equalization techniques are considered. At the channel sounding stage, each user transmits a pilot sequence with the length $N_{\mathrm{p}} \geq K$ over different time slots on a given subcarrier allocated to pilot symbols [17]. The pilot sequence of length N_{p} for a given user k at a given subcarrier m, $\overline{\mathbf{p}}_m^k$, is chosen from a pilot book $\overline{\mathbf{P}}_m = [\overline{\mathbf{p}}_m^0, \overline{\mathbf{p}}_m^1, \ldots, \overline{\mathbf{p}}_m^{K-1}]^{\mathrm{T}}$ that satisfies the orthogonality property $\overline{\mathbf{P}}_m\overline{\mathbf{P}}_m^{\mathrm{H}} = N_{\mathrm{p}}\mathbf{I}_K$, [59]. Consider a pilot book where each $\overline{\mathbf{p}}_m^k$ is obtained from k cyclic shifts of the Zadoff-Chu (ZC) root sequence of length N_{p}. Using (3.3), the received pilots from all the users at subcarrier m can be represented as $\overline{\mathbf{Y}}_m^{\mathrm{p}} = \overline{\boldsymbol{\Lambda}}_m\overline{\mathbf{P}}_m + \overline{\mathbf{W}}_m^{\mathrm{p}}$. Consequently, the channel response for all the users at a given subcarrier m can be estimated as

$$\widehat{\mathbf{\Lambda}}_m = \frac{1}{N_\mathrm{p}}\overline{\mathbf{Y}}^\mathrm{p}_m\overline{\mathbf{P}}^\mathrm{H}_m = \overline{\mathbf{\Lambda}}_m + \frac{1}{N_\mathrm{p}}\overline{\mathbf{W}}^\mathrm{p}_m\overline{\mathbf{P}}^\mathrm{H}_m \triangleq \overline{\mathbf{\Lambda}}_m + \widetilde{\mathbf{W}}_m, \tag{3.4}$$

where $\widetilde{\mathbf{W}}_m = \frac{1}{N_\mathrm{p}}\overline{\mathbf{W}}^\mathrm{p}_m\overline{\mathbf{P}}^\mathrm{H}_m$.

To estimate the CFR at all subcarriers, it is sufficient to allocate $m_\mathrm{P} = L$ subcarriers as pilots [47]. This is due to the fact that the L CFR estimates can be transformed to the time domain, obtaining the CIR, where the channel has only L parameters. Subsequently, the CIR can be transformed again to frequency to obtain the CFR of all subcarriers. Let $\mathcal{I}$ represent the set of subcarrier indices allocated to the pilot, and $\boldsymbol{\lambda}^\mathcal{I}_{q,k}$ the vector formed by selecting the m_P entries of $\boldsymbol{\lambda}_{q,k}$ at the pilot subcarriers, each element of $\boldsymbol{\lambda}^\mathcal{I}_{q,k}$ can be estimated from (3.4), as $\lambda_{q,k}[m] = [\widehat{\mathbf{\Lambda}}_m]_{q,k}$. From (3.2), the following relation between CFR and CIR holds

$$\boldsymbol{\lambda}^\mathcal{I}_{q,k} = \sqrt{M}\mathbf{F}^\mathcal{I}_M\mathbf{h}_{q,k}, \tag{3.5}$$

where $\mathbf{F}^\mathcal{I}_M$ is a $m_\mathrm{P} \times L$ matrix formed by selecting the L first columns of $\mathbf{F}_M$ with the rows indexed by $\mathcal{I}$. Hence, the CIR of user k at a given BS antenna q can be estimated by solving (3.5) for $\mathbf{h}_{q,k}$, i.e., $\mathbf{h}_{q,k} = \frac{1}{\sqrt{M}}(\mathbf{F}^\mathcal{I}_M)^{-1}\boldsymbol{\lambda}^\mathcal{I}_{q,k}$. Finally, after obtaining the CIR, $\widehat{\mathbf{\Lambda}}_m$ at each subcarrier can be reconstructed with (3.2). Therefore, the channel estimation process, (3.4) and (3.5), requires a minimum of LK pilots.

Using the channel estimates $\widehat{\mathbf{\Lambda}}_m$, and deploying a linear combining technique such as MRC, the transmit data symbols for all the users can be estimated as

$$\widehat{\mathbf{X}}^\mathrm{MRC}_m = \mathbf{\Gamma}^{-1}_m\widehat{\mathbf{\Lambda}}^\mathrm{H}_m\mathbf{Y}^\mathrm{d}_m = \mathbf{\Gamma}^{-1}_m\widehat{\mathbf{\Lambda}}^\mathrm{H}_m(\overline{\mathbf{\Lambda}}_m\mathbf{D}_m + \mathbf{W}^\mathrm{d}_m), \tag{3.6}$$

where $\mathbf{\Gamma}_m$ is a $K \times K$ diagonal matrix, with the k^th diagonal element given by $\frac{1}{Q}\sum_{q=0}^{Q-1}|\lambda_{q,k}[m]|^2$, considered solely to normalize the amplitude of the equalizer output. In the literature, the effect of channel estimation noise is often neglected and the diagonal elements of $\mathbf{\Gamma}_m$ are formed from the diagonal elements of $\overline{\mathbf{\Lambda}}^\mathrm{H}_m\overline{\mathbf{\Lambda}}_m$, i.e., the norm squared of the channel vector for each user at a given subcarrier m. However, in the presence of channel estimation errors, using (3.4), the normalization factors on the elements of $\overline{\mathbf{\Lambda}}^\mathrm{H}_m\overline{\mathbf{\Lambda}}_m$ are obtained as the diagonal elements of

$$\widehat{\mathbf{\Lambda}}^\mathrm{H}_m\widehat{\mathbf{\Lambda}}_m = \widehat{\mathbf{\Lambda}}^\mathrm{H}_m\overline{\mathbf{\Lambda}}_m + \overline{\mathbf{\Lambda}}^\mathrm{H}_m\widetilde{\mathbf{W}}_m + \frac{1}{N_\mathrm{p}^2}\overline{\mathbf{P}}_m(\overline{\mathbf{W}}^\mathrm{p}_m)^\mathrm{H}\overline{\mathbf{W}}^\mathrm{p}_m\overline{\mathbf{P}}^\mathrm{H}_m. \tag{3.7}$$

The term $\overline{\mathbf{\Lambda}}_m^{\mathrm{H}}\widetilde{\mathbf{W}}_m$ tends to zero in the asymptotic regime, as $Q \to \infty$, since the channel gain and noise are independent. However, the same is not true for $(\overline{\mathbf{W}}_m^{\mathrm{p}})^{\mathrm{H}}\overline{\mathbf{W}}_m^{\mathrm{p}}$. As $\overline{\mathbf{W}}_m^{\mathrm{p}}$ represents the AWGN, in the asymptotic regime, it can be derived that

$$\left(\overline{\mathbf{\Lambda}}_m^{\mathrm{H}}\widetilde{\mathbf{W}}_m + \frac{1}{N_{\mathrm{p}}^2}\overline{\mathbf{P}}_m(\overline{\mathbf{W}}_m^{\mathrm{p}})^{\mathrm{H}}\overline{\mathbf{W}}_m^{\mathrm{p}}\overline{\mathbf{P}}_m^{\mathrm{H}}\right) \to \frac{Q\sigma_w^2}{N_{\mathrm{p}}^2}\overline{\mathbf{P}}_m\overline{\mathbf{P}}_m^{\mathrm{H}}. \tag{3.8}$$

Hence, taking a similar approach to [60], the channel estimation noise can be mitigated by subtracting (3.8) from the normalization factor, i.e., $\mathbf{\Gamma}_m$ is formed from the diagonal elements of $(\widehat{\mathbf{\Lambda}}_m^{\mathrm{H}}\widehat{\mathbf{\Lambda}}_m - \frac{Q\sigma_w^2}{N_{\mathrm{p}}^2}\overline{\mathbf{P}}_m\overline{\mathbf{P}}_m^{\mathrm{H}})$.

Due to the channel hardening effect [17], in the asymptotic regime, as $Q \to \infty$, it can be derived

$$\frac{\overline{\boldsymbol{\lambda}}_{m,k}^{\mathrm{H}}\overline{\boldsymbol{\lambda}}_{m,k'}}{Q} \to \begin{cases} \mathbb{E}\{|\overline{\lambda}_{m,k}[q]|^2\} = 1 & \text{if } k = k' \\ 0 & \text{otherwise} \end{cases}, \tag{3.9}$$

where $\overline{\boldsymbol{\lambda}}_{m,k}$, of length Q, represents the k^{th} column of $\overline{\mathbf{\Lambda}}_m$. Therefore, as $Q \to \infty$, $\mathbf{\Gamma}_m^{-1}\widehat{\mathbf{\Lambda}}_m^{\mathrm{H}}\overline{\mathbf{\Lambda}}_m \to \mathbf{I}_K$.

In practical systems, the number of BS antennas is limited, and the off-diagonal elements of $\widehat{\mathbf{\Lambda}}_m^{\mathrm{H}}\overline{\mathbf{\Lambda}}_m$, in (3.6), lead to a significant amount of interference. Thus, MMSE combining,

$$\widehat{\mathbf{X}}_m^{\mathrm{MMSE}} = \mathbf{\Phi}_m^{\mathrm{MMSE}}\overline{\mathbf{Y}}_m^{\mathrm{d}}, \tag{3.10}$$

where $\mathbf{\Phi}_m^{\mathrm{MMSE}} \triangleq (\widehat{\mathbf{\Lambda}}_m^{\mathrm{H}}\widehat{\mathbf{\Lambda}}_m - \frac{Q\sigma_w^2}{N_{\mathrm{p}}^2}\overline{\mathbf{P}}_m\overline{\mathbf{P}}_m^{\mathrm{H}} + \sigma_w^2\mathbf{I}_K)^{-1}\widehat{\mathbf{\Lambda}}_m^{\mathrm{H}}$, provides an improved performance compared to MRC.

3.3 The Proposed Joint Channel Estimation and Equalization Technique

The linear combining techniques presented in the previous section take advantage of the channel hardening effect and spatial diversity gains in massive MIMO. However, it requires knowledge of the CFR at all subcarriers, and therefore, a minimum of LK time-frequency slots are allocated to the pilots for channel estimation. In practical systems, L can take large values, especially as the bandwidth increases. Hence, in this section, a novel method is proposed that is capable of reducing the pilot overhead to a single pilot subcarrier. Therefore, only K time-frequency slots would be necessary for pilot allocation, reducing the training overhead by a factor of L.

In current standards, the subcarrier spacing Δf is chosen to be much shorter than the coherence bandwidth [88]. Hence, the channel can be considered flat across the frequency band of multiple adjacent subcarriers. This suggests that the channel at a single subcarrier can be considered for the equalization of its adjacent subcarriers. Moreover, the correlation between the CFR of adjacent subcarriers can be obtained from the following approximation [7]

$$|\alpha_{\Delta m,k}| \approx \sqrt{1 - \left(\frac{\Delta f \Delta m}{F_{\mathrm{c}}}\right)^2}, \tag{3.11}$$

where $\alpha_{\Delta m,k} \triangleq \mathbb{E}\{\overline{\lambda}^*_{m,k}[q]\overline{\lambda}_{((m+\Delta m))_M,k}[q]\}$, $F_{\mathrm{c}} = \frac{1}{\ell_\tau}$ is the coherence bandwidth and ℓ_τ is the maximum delay spread of the channel.

Taking this into account, consider a reference pilot in one subcarrier where its channel estimate is used for equalization of the neighboring subcarriers. The detected data symbols will be considered as virtual pilots, updating their channel estimates and allowing for the equalization of data at their adjacent subcarriers. This process can then be repeated, in a sliding manner, until all the data and the CFR in the UL frame are estimated. Hence, the data $\overline{\mathbf{X}}_m$, at any given subcarrier m, can be equalized using (3.10) and (3.11) with the CFR at subcarrier $m-1$ as

$$\widehat{\mathbf{X}}_m^{\mathrm{MMSE}} = \frac{1}{|\alpha_{1,k}|}\mathbf{\Phi}_{m-1}^{\mathrm{MMSE}}\overline{\mathbf{Y}}_m. \tag{3.12}$$

In (3.12), it was considered the approximation $(\widehat{\mathbf{\Lambda}}_m)^{\mathrm{H}}\widehat{\mathbf{\Lambda}}_m \approx (\widehat{\mathbf{\Lambda}}_{m-1})^{\mathrm{H}}\widehat{\mathbf{\Lambda}}_{m-1}$, and the phase of $\alpha_{1,k}$ to be negligible.

After obtaining $\widehat{\mathbf{X}}_m^{\mathrm{MMSE}}$, hard decision is performed by quantizing each symbol to their nearest QAM constellation point, resulting in $\widehat{\mathbf{X}}_m^{\mathrm{HD}}$. With $\widehat{\mathbf{X}}_m^{\mathrm{HD}}$, the CFR estimate at subcarrier m can be updated as

$$\widehat{\mathbf{\Lambda}}_m = \overline{\mathbf{Y}}_m(\widehat{\mathbf{X}}_m^{\mathrm{HD}})^\dagger. \tag{3.13}$$

This channel estimate is then used for equalization of the following subcarrier, $m+1$, using (3.12). It is worth noting that, since $\widehat{\mathbf{X}}_m$ was considered as the pilot, the noise mitigation term in (3.8) should be corrected accordingly. That is, the term $\overline{\mathbf{P}}_m^{\mathrm{H}}$ in $\mathbf{\Gamma}_m$ and $\mathbf{\Phi}_m^{\mathrm{MMSE}}$ should be substituted by $(\widehat{\mathbf{X}}_m^{\mathrm{HD}})^\dagger$. Then the procedure is repeated in a sliding manner until the whole frame is equalized. If the detected symbols $\widehat{\mathbf{X}}_m^{\mathrm{HD}}$ are erroneous, (3.13) provides imperfect channel estimates, and hence, the sliding technique propagates the error to further subcarriers. Therefore, the concept of depth is proposed, further described in the later part of this section. Incorporating the concept of depth in the proposed joint channel estimation and equalization method significantly improves the accuracy of $\widehat{\mathbf{X}}_m^{\mathrm{HD}}$, alleviating the error propagation issue.

It is worth noting that $\overline{\mathbf{X}}_m$ can be a rank-deficient matrix. Specifically, if the rank of $\overline{\mathbf{X}}_m$ is lower than K, (3.13) fails to retrieve $\widehat{\mathbf{\Lambda}}_m$. To solve this issue, $\alpha_{\Delta m,k}$ is calculated for any value of Δm. This way, $\widehat{\mathbf{X}}_m^{\mathrm{MMSE}}$ at any subcarrier can be detected with the same reference pilot using (3.12).

Proposition 1 *In the asymptotic regime, it is possible to perform MRC with the channel estimates on a single subcarrier. In other words, the data at any given subcarrier m can be equalized with the CFR at any other subcarrier m'.*

Proof The data $\overline{\mathbf{X}}_m$, at any given subcarrier m, can be detected by performing MRC with the channel estimates at subcarrier m'

$$\widehat{\mathbf{X}}_m^{\mathrm{MRC}} = \mathbf{\Gamma}_{m'}^{-1}\mathbf{\Lambda}_{m'}^{\mathrm{H}}\mathbf{Y}_m^{\mathrm{d}}. \tag{3.14}$$

Considering (3.9) in the asymptotic regime, as $Q \to \infty$,

$$\frac{\overline{\boldsymbol{\lambda}}_{m',k'}^{\mathrm{H}}\overline{\boldsymbol{\lambda}}_{m,k}}{Q} \to \begin{cases} \alpha_{\Delta m,k} & \text{if } k = k' \\ 0 & \text{otherwise} \end{cases}, \tag{3.15}$$

where $\Delta m = m - m'$. Consequently, in (3.14), $\mathbf{\Gamma}_{m'}^{-1}\mathbf{\Lambda}_{m'}^{\mathrm{H}}\mathbf{\Lambda}_m \to \mathbf{\Psi}_{\Delta m}$, where $\mathbf{\Psi}_{\Delta m}$ is a diagonal matrix with the diagonal elements formed by the vector $[\alpha_{\Delta m,0}, \ldots, \alpha_{\Delta m,K-1}]$.

The exact value of $\alpha_{\Delta m,k}$ can be obtained by substituting the CFRs with the expression given in (3.2). This yields a quadratic form, with the expectation defined as [89]

$$\mathbb{E}\{\widetilde{\mathbf{h}}_{q,k}^{\mathrm{H}}(M\mathbf{f}_{M,m}^{*}\mathbf{f}_{M,((m+\Delta m))_M}^{\mathrm{T}})\widetilde{\mathbf{h}}_{q,k}\} = \mathrm{tr}\{\mathbf{A}\widetilde{\mathbf{\Sigma}}_k\} + \boldsymbol{\mu}'\mathbf{A}\boldsymbol{\mu}, \tag{3.16}$$

where $\mathbf{A} = M\mathbf{f}_{M,m}^{*}\mathbf{f}_{M,((m+\Delta m))_M}^{\mathrm{T}}$. The variables $\boldsymbol{\mu}$ and $\widetilde{\mathbf{\Sigma}}_k$ represent the mean and covariance matrices of $\widetilde{\mathbf{h}}_{q,k}$, respectively. With the parameters presented in section 3.1, it is given that the channel is zero mean, i.e., $\boldsymbol{\mu} = \mathbf{0}_{M\times 1}$, and $\widetilde{\mathbf{\Sigma}}_k$ is a diagonal matrix with the diagonal elements formed by the vector $\widetilde{\boldsymbol{\rho}}_k = [\boldsymbol{\rho}_k^{\mathrm{T}}, \mathbf{0}_{M-L\times 1}^{\mathrm{T}}]^{\mathrm{T}}$. Hence, (3.16) reduces to

$$\alpha_{\Delta m,k} = \mathrm{tr}\{\mathbf{A}\widetilde{\mathbf{\Sigma}}_k\} = \sqrt{M}\mathbf{f}_{M,((\Delta m))_M}^{\mathrm{T}}\widetilde{\boldsymbol{\rho}}_k. \tag{3.17}$$

Based on this result, as long as the PDP is known, equalization can be performed using (3.14) followed by scaling the MRC output for each subcarrier by $\frac{1}{\alpha_{\Delta m,k}}$. It is worth noting that the PDP can also be estimated within a superframe of transmission blocks, as shown in [60]. $\blacksquare$

In the asymptotic regime, it is sufficient to use *Proposition* 1 and the channel estimate from a single subcarrier to equalize the entire OFDM frame. However, in practical systems, the aforementioned scaling by $\frac{1}{\alpha_{\Delta m,k}}$ may lead to noise enhancement and, consequently, a performance loss. For this reason, the proposed equalization technique is performed in a sliding manner, as $\alpha_{\Delta m,k}$ is larger for the smaller values of $|\Delta m|$. When $\overline{\mathbf{X}}_m$ is rank-deficient, $\widehat{\mathbf{\Lambda}}_m$ cannot be estimated. Thus, it is necessary to utilize the previously estimated channels on the closest subcarrier, independent of $|\Delta m|$. Furthermore, if the PDP is known at the receiver, the scaling term $\alpha_{\Delta m,k}$ can be calculated from (3.17), instead of using the approximation from (3.11).

3.4 Frequency Diversity

In the previous sections, it was shown how the system can benefit from using the CFR from a single subcarrier to estimate the data of adjacent subcarriers within the coherence bandwidth. However, this concept can be seen from a different angle, where the data from a single subcarrier can be estimated using the CFR from all adjacent subcarriers within the coherence bandwidth. In other words, the coherence bandwidth can also be seen as a form of frequency diversity. To this end, this section starts by showing how the proposed joint channel estimation and equalization technique can take advantage of frequency diversity through the concept of *depth*. Then, this section also shows how frequency diversity is ineffective in conventional methods. In particular, the derivations of this section show that, in conventional methods, frequency diversity is only beneficial when a large number of pilots is used. This is while using only $m_{\mathrm{P}} = L$ results in no gains from frequency diversity.

3.4.1 Depth Concept

When the coherence bandwidth is much larger than the subcarrier spacing, the correlation $\alpha_{\Delta m,k}$ takes large values for multiple values of Δm. This sparks the idea of taking advantage of the frequency diversity in addition to the spatial diversity. To this end, improved SINR performance can be achieved by performing equalization for each subcarrier multiple times, each with the channel of a different subcarrier within the coherence bandwidth. This improvement substantially reduces the error propagation issue from (3.13).

While the channels from all subcarriers could be considered for the averaging, the channels with a small correlation would bring minimal improvement to the output. Since, the value of $\alpha_{\Delta m,k}$ decreases as the value of $|\Delta m|$ increases, only channels of subcarriers within a range are considered. Hence, the maximum range considered is denoted as the depth, D.

Ideally, the depth would consider all adjacent subcarriers, at higher and lower indices. However, since the channels are updated in a sliding manner, only the channel on one side of the subcarriers is available at the time of equalization. Therefore, the final output of my proposed technique is achieved with two steps. The first step of the proposed technique is performed by sliding from lower to upper subcarrier indices until the whole frame is equalized. For the second step, the procedure is realized again, however, now sliding from higher to lower subcarrier indices. It is worth noting that both steps can be realized in parallel as the steps are independent of each other. The outputs from both steps are then averaged to obtain the final output of the proposed technique. Each step is distinguished with the direction variable $\xi \in [-1, 1]$ representing steps one and two, respectively. This way, each step can be represented as

$$\widehat{\mathbf{X}}_{m,\xi} = \frac{1}{D} \sum_{\Delta m=1}^{D} \mathbf{\Psi}_{\xi\Delta m}^{-1} \mathbf{\Phi}_{m-\xi\Delta m}^{\mathrm{MMSE}} \overline{\mathbf{Y}}_{m}. \tag{3.18}$$

The final output is then obtained as $\widehat{\mathbf{X}}_m = \frac{1}{2}(\widehat{\mathbf{X}}_{m,-1} + \widehat{\mathbf{X}}_{m,1})$. The proposed technique is summarized in Algorithm 1 and depicted in Fig. 3.1.

3.4.2 Frequency Diversity in Conventional Methods

It is worth noting that the frequency diversity is unique to the proposed method in this chapter and depth cannot be adapted to the conventional MMSE combining. Noticeably, the LS channel estimation technique estimates the CFR at all subcarriers. With all the channel estimates, it becomes possible to perform MMSE combining multiple times to detect each subcarrier, each combining using the CFR at the corresponding subcarrier and the adjacent subcarriers, in the same manner as the proposed depth method. Hence, it can be misconstrued that averaging all these outputs would achieve the same frequency diversity as in the proposed depth method. However, this is not possible due to the fact that when using only $m_{\mathrm{P}} = L$ pilots to estimate the channel at M subcarriers, the channel estimation noise between adjacent subcarriers becomes correlated. The main benefit of the depth implementation is that it can essentially average the channel estimation noise with frequency diversity.

Algorithm 1 Proposed sliding technique with reference pilot at subcarrier i.

Initialize: Estimate channel at reference subcarrier (Pilot), obtaining $\widehat{\mathbf{\Lambda}}_i$ using (3.4).
for $\xi = [-1, 1]$ **do**
  $m' = i$ {Define the anchor for closest available CFR}
  for $m_{\text{dir}} = 1$ to $M - 1$ **do**
    $m = ((i + \xi m_{\text{dir}}))_M$
    Initialize $\widehat{\mathbf{X}}_{m,\xi} = \mathbf{0}_{K \times N}$
    $c = 0$ {Define total channels used for equalization}
    for $\Delta m = 1$ to D **do**
      if $\widehat{\mathbf{\Lambda}}_{((m-\xi\Delta m))_M}$ was estimated **then**
        $\widehat{\mathbf{X}}_{m,\xi} = \widehat{\mathbf{X}}_{m,\xi} + \mathbf{\Psi}^{-1}_{\xi\Delta m}\mathbf{\Phi}^{\text{MMSE}}_{((m-\xi\Delta m))_M}\overline{\mathbf{Y}}_m$
        $c = c + 1$
      end if
    end for
    if $c == 0$ **then**
      $\widehat{\mathbf{X}}_{m,\xi} = \mathbf{\Psi}^{-1}_{m-m'}\mathbf{\Phi}^{\text{MMSE}}_{m'}\overline{\mathbf{Y}}_m$
    else
      $\widehat{\mathbf{X}}_{m,\xi} = \frac{\widehat{\mathbf{X}}_{m,\xi}}{c}$
    end if
    $\widehat{\mathbf{X}}^{\text{HD}}_{m,\xi}$ is obtained from hard decision of $\widehat{\mathbf{X}}_{m,\xi}$
    if $\widehat{\mathbf{X}}^{\text{HD}}_{m,\xi}$ is invertible **then**
      $\widehat{\mathbf{\Lambda}}_m = \overline{\mathbf{Y}}_m(\widehat{\mathbf{X}}^{\text{HD}}_m)^{\dagger}$ and update $m' = m$
    else
      $\widehat{\mathbf{\Lambda}}_m$ is not estimated and m' is not updated
    end if
  end for
end for
Obtain $\widehat{\mathbf{X}}_m$ by averaging the two sets of result

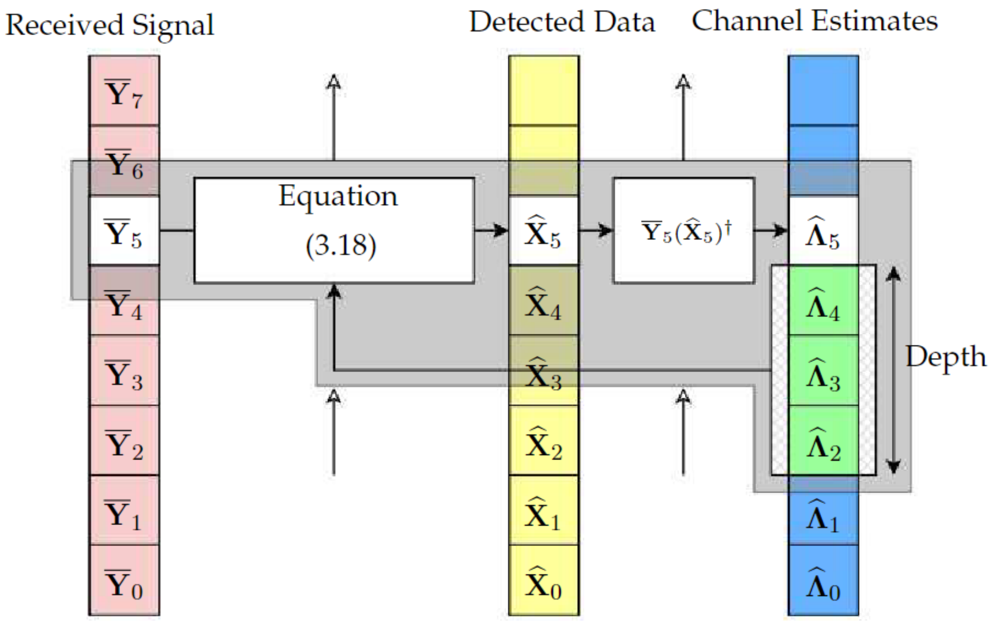

Fig. 3.1 Proposed technique sliding from lower to higher subcarrier indexes, i.e., $\xi = 1$. Sliding to the opposite direction ($\xi = -1$) can be performed in parallel and both outputs are averaged to obtain the results in (3.18)

However, if the noise is correlated, then the frequency diversity gain becomes very limited. Thus, in the following, it is mathematically proven that the channel estimation noise between subcarriers is correlated.

To prove that the noise terms from the estimated CFR are correlated in the conventional method, the covariance between the noise terms in two different subcarriers is derived. To simplify the analysis, without loss of generality, the scenario is reduced to a single user. With a single user, the pilot needs to be inserted only in one symbol, or time slot, i.e., $\overline{\mathbf{p}}_m^0 = [1]$. Hence, the channel estimation matrix in equation (3.4) becomes a $Q \times 1$ vector given as

$$\widehat{\boldsymbol{\lambda}}_m = \overline{\boldsymbol{\lambda}}_m + \overline{\mathbf{w}}_m^{\mathrm{p}}, \tag{3.19}$$

where Q denotes the number of BS antennas.

Consider now a generic representation of the relation between CFR and CIR shown in (3.5). The following representation assumes $m_{\mathrm{P}} \geq L$ and includes the noise term

$$\boldsymbol{\lambda}_q^{\mathcal{I}} = \sqrt{M}\mathbf{F}_M^{\mathcal{I}}\mathbf{h}_q + \mathbf{w}_q^{\mathcal{I}}, \tag{3.20}$$

where $\mathbf{w}_q^{\mathcal{I}}$ is the noise vector at subcarrier indices within the set $\mathcal{I}$ at BS antenna q, and $\mathbf{h}_q$ represents the CIR from the single user to antenna q. Again, $\mathbf{F}_M^{\mathcal{I}}$ is a $m_{\mathrm{P}} \times L$ matrix formed by selecting the L first columns of $\mathbf{F}_M$ with the rows indexed by $\mathcal{I}$, only now m_{P} may assume values different of L. From (3.20), the CIR can be estimated as

$$\widehat{\mathbf{h}}_q = \left(\sqrt{M}\mathbf{F}_M^{\mathcal{I}}\right)^{\dagger} \boldsymbol{\lambda}_q^{\mathcal{I}} = \mathbf{h}_q + \left(\sqrt{M}\mathbf{F}_M^{\mathcal{I}}\right)^{\dagger} \mathbf{w}_q^{\mathcal{I}}. \tag{3.21}$$

To simplify the analysis, consider that m_{P} is a divisor of M. This way, the term $\sqrt{M}\mathbf{F}_M^{\mathcal{I}}$ becomes L first columns of the m_{P}-point DFT matrix, and the pseudo inverse of $\sqrt{M}\mathbf{F}_M^{\mathcal{I}}$ becomes

$$\left(\sqrt{M}\mathbf{F}_M^{\mathcal{I}}\right)^{\dagger} = \frac{\sqrt{M}}{m_{\mathrm{P}}}(\mathbf{F}_M^{\mathcal{I}})^{\mathrm{H}}. \tag{3.22}$$

Hence, (3.21) can be simplified as

$$\widehat{\mathbf{h}}_q = \mathbf{h}_q + \frac{\sqrt{M}}{m_{\mathrm{P}}}(\mathbf{F}_M^{\mathcal{I}})^{\mathrm{H}}\mathbf{w}_q^{\mathcal{I}}. \tag{3.23}$$

With the CIR estimates from (3.23), the CFR estimates at each subcarrier m can be obtained as

$$\widehat{\lambda}_q[m] = \sqrt{M}\mathbf{f}_{M,m}^{\mathrm{T}}[\widehat{\mathbf{h}}_q^{\mathrm{T}}, \mathbf{0}_{1\times(M-L)}]^{\mathrm{T}} = \lambda_q[m] + \frac{M}{m_{\mathrm{P}}}\mathbf{f}_{M,m}^{\mathrm{T}}[\left((\mathbf{F}_M^{\mathcal{I}})^{\mathrm{H}}\mathbf{w}_q^{\mathcal{I}}\right)^{\mathrm{T}}, \mathbf{0}_{1\times(M-L)}]^{\mathrm{T}}, \tag{3.24}$$

where $\mathbf{f}_{M,m}$ denotes the m^{th} column of $\mathbf{F}_M$. The vector containing the channel estimation noise at all the subcarriers for a given antenna q is defined as $\boldsymbol{\beta}_q = [\beta_q[0], \ldots, \beta_q[M-1]]^{\mathrm{T}}$, where $\beta_q[m] = \frac{M}{m_{\mathrm{P}}}\mathbf{f}_{M,m}^{\mathrm{T}}[\left((\mathbf{F}_M^{\mathcal{I}})^{\mathrm{H}}\mathbf{w}_q^{\mathcal{I}}\right)^{\mathrm{T}}, \mathbf{0}_{1\times(M-L)}]^{\mathrm{T}}$.

With the expression for the noise terms, it can be proven that the channel estimation noise between different subcarriers is correlated by calculating the covariance.

$$\mathrm{cov}\{\beta_q[m], \beta_q[m']\} = \mathbb{E}\{\beta_q[m]\beta_q^*[m']\} - \mathbb{E}\{\beta_q[m]\}\mathbb{E}\{\beta_q^*[m']\}. \tag{3.25}$$

Since the terms of $(\mathbf{w}_q^{\mathcal{I}})^{\mathrm{T}}$ are zero mean and independent from each other, the term $\mathbb{E}\{\beta_q[m]\}\mathbb{E}\{\beta_q^*[m']\}$ is zero. Therefore, the covariance is calculated with only the expected value

$$\mathbb{E}\{\beta_q[m]\beta_q^*[m']\} = \mathbb{E}\{\frac{M^2}{M_{\mathrm{P}}^2}[(\mathbf{w}_q')^{\mathrm{T}}, \mathbf{0}_{1\times(M-m_{\mathrm{P}})}]^*\mathbf{f}_{M,m'}^*\mathbf{f}_{M,m}^{\mathrm{T}}[(\mathbf{w}_q')^{\mathrm{T}}, \mathbf{0}_{1\times(M-m_{\mathrm{P}})}]^{\mathrm{T}}\}, \tag{3.26}$$

where $\mathbf{w}'_q = \big((\mathbf{F}_M^{\mathcal{I}})^{\mathrm{H}}\mathbf{w}_q^{\mathcal{I}}\big)$. Since the normalized DFT matrix is a unitary matrix, $\mathbf{w}'_q$ retains the statistical properties of $\mathbf{w}_q^{\mathcal{I}}$. Hence, similar to (3.16), the expectation in (3.26) can be calculated using the quadratic forms formula [89]

$$\frac{M^2}{M_{\mathrm{P}}^2}\mathbb{E}\{[(\mathbf{w}'_q)^{\mathrm{T}}, \mathbf{0}_{1\times(M-m_{\mathrm{P}})}]^*\mathbf{f}^*_{M,m'}\mathbf{f}^{\mathrm{T}}_{M,m}[(\mathbf{w}'_q)^{\mathrm{T}}, \mathbf{0}_{1\times(M-m_{\mathrm{P}})}]^{\mathrm{T}}\} = \frac{M^2}{M_{\mathrm{P}}^2}(\mathrm{tr}\{\mathbf{A}\boldsymbol{\Sigma}\} + \boldsymbol{\mu}^{\mathrm{T}}\mathbf{A}\boldsymbol{\mu}), \tag{3.27}$$

where $\boldsymbol{\mu}$ and $\boldsymbol{\Sigma}$ represent the mean and covariance matrices of $[(\mathbf{w}'_q)^{\mathrm{T}}, \mathbf{0}_{1\times(M-m_{\mathrm{P}})}]^{\mathrm{T}}$, respectively, and $\mathbf{A} = \mathbf{f}^*_{M,m'}\mathbf{f}^{\mathrm{T}}_{M,m}$. Given that $\mathbf{w}'_q$ is composed from the AWGN noise and the DFT matrix, its statistical measures can be derived as

$$\boldsymbol{\mu} = \mathbf{0}_{M\times 1} \text{ and } \boldsymbol{\Sigma} = \frac{m_{\mathrm{P}}}{M}\mathrm{diag}\{[\sigma_w^2, \ldots, \sigma_w^2, \mathbf{0}_{1\times(M-m_{\mathrm{P}})}]^{\mathrm{T}}\}. \tag{3.28}$$

Finally, substituting the aforementioned values in (3.27) results in

$$\begin{aligned}
\mathrm{cov}\{\beta_q[m], \beta_q[m']\} &= \frac{\sqrt{M}}{m_{\mathrm{P}}}\mathbf{f}^{\mathrm{T}}_{M,(m-m')}[\sigma_w^2, \ldots, \sigma_w^2, \mathbf{0}_{1\times(M-m_{\mathrm{P}})}]^{\mathrm{T}} = \\
&= \frac{\sigma_w^2}{m_{\mathrm{P}}}\sum_{l=0}^{m_{\mathrm{P}}-1} e^{\frac{-j2\pi(m-m')l}{M}} \\
&= \left(\frac{\sigma_w^2}{m_{\mathrm{P}}}\right)\frac{1-e^{\frac{-j2\pi(m-m')m_{\mathrm{P}}}{M}}}{1-e^{\frac{-j2\pi(m-m')}{M}}} \\
&= \left(\frac{\sigma_w^2}{m_{\mathrm{P}}}\right)\frac{\sin(\frac{\pi(m-m')m_{\mathrm{P}}}{M})}{\sin(\frac{\pi(m-m')}{M})}e^{\frac{-j\pi(m-m')(m_{\mathrm{P}}-1)}{M}} \\
&= \sigma_w^2\frac{\mathrm{sinc}(\frac{(m-m')m_{\mathrm{P}}}{M})}{\mathrm{sinc}(\frac{(m-m')}{M})}e^{\frac{-j\pi(m-m')(m_{\mathrm{P}}-1)}{M}}.
\end{aligned} \tag{3.29}$$

From (3.29), it can be deduced that the noise terms are only uncorrelated when $\mathrm{sinc}(\frac{(m-m')m_{\mathrm{P}}}{M}) = 0$, i.e., if $m - m'$ is a multiple of $\frac{M}{m_{\mathrm{P}}}$. Furthermore, the correlation between the noise terms of the adjacent subcarriers will be the highest. Since depth is only effective with the subcarriers within the coherence bandwidth, i.e., in the neighborhood of each subcarrier, implementing depth in the conventional MMSE combining fails to average out noise effectively. These results also show that the noise terms become correlated due to estimating M CFR terms with only m_{P} pilots. This issue can be solved by allocating one pilot for each subcarrier, i.e., $m_{\mathrm{P}} = M$, making all the noise terms uncorrelated. However, this is not practical as this leads to a large spectral efficiency loss. In contrast, in the proposed joint channel estimation and equalization technique, data subcarriers are utilized as virtual pilots to estimate the channel. This can be seen as deploying a pilot per subcarrier. In other words, in the proposed technique, the CFR is estimated as if the effective number of pilots was $m_{\mathrm{P}} = M$. Consequently, the covariance of channel estimation noise for the proposed technique using (3.29) becomes zero. The same conclusion can be drawn from (3.13), where the channel estimate at a given subcarrier m is obtained as

$$\widehat{\mathbf{\Lambda}}_m = \overline{\mathbf{Y}}_m(\widehat{\mathbf{X}}_m^{\mathrm{HD}})^{\dagger} = \overline{\mathbf{\Lambda}}_m + \overline{\mathbf{W}}_m(\widehat{\mathbf{X}}_m^{\mathrm{HD}})^{\dagger}. \tag{3.30}$$

Since $\overline{\mathbf{W}}_m$ is the AWGN in the frequency domain and all the data symbols are considered to be uncorrelated, the channel estimation noise $\overline{\mathbf{W}}_m(\widehat{\mathbf{X}}_m^{\mathrm{HD}})^{\dagger}$, will be uncorrelated from one subcarrier to another.

In the following section, the performance of the proposed technique is numerically evaluated. The conventional LS-based channel estimation and MMSE combining are used as a benchmark comparison for the proposed method. It is shown that the proposed channel estimation and equalization method, using only K pilots, outperforms the conventional method, which requires LK pilots.

3.5 Numerical Analysis

In this section, the efficacy of the proposed technique is evaluated and compared with the conventional LS-based channel estimation and MMSE equalization. The following parameters are in accordance with the 3rd Generation Partnership Project (3GPP) standards given in [44]. In the simulations, the UL transmission of a single frame with 16-QAM and OFDM modulation, $M = 1024$ subcarriers, and $N = 14$ time symbols are considered. The BS serves $K = 7$ users, where $N_{\mathrm{p}} = 7$ time slots are allocated to each user for channel estimation, and $N_{\mathrm{d}} = 7$ time slots for data transmission. The ETU channel model, [44], with a coherence bandwidth of $F_{\mathrm{c}} \approx 200$ kHz, is used. Considering subcarrier spacing of $\Delta f = 15$ kHz and transmission bandwidth of 15 MHz, the channel length is determined to be $L = 77$. Therefore, for the conventional LS-based channel estimators, $m_{\mathrm{P}} = L$ pilot subcarriers are deployed, resulting in a total of $LN_{\mathrm{p}} = 539$ time-frequency resources allocated for pilot transmission. This is while the proposed technique requires only $N_{\mathrm{p}} = 7$ time-frequency resources. Perfect knowledge of the PDP for each user at the BS is assumed. These results were obtained through the ensemble average of 5000 random trials.

In Fig. 3.2, the SINR performance of the proposed technique is evaluated against the number of BS antennas for depth factors of $D = 1, 2, 3$, and without the imple-

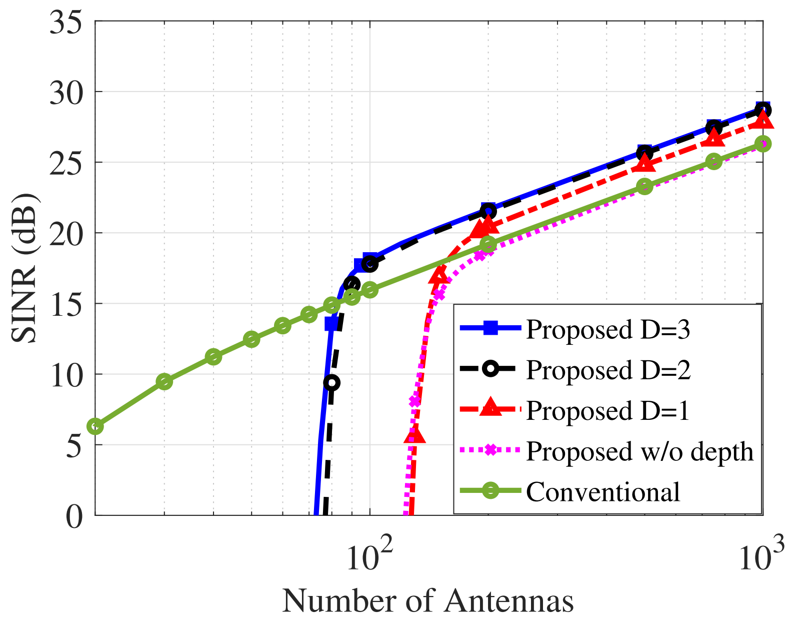

Fig. 3.2 SINR performance as a function of the number of BS antennas.

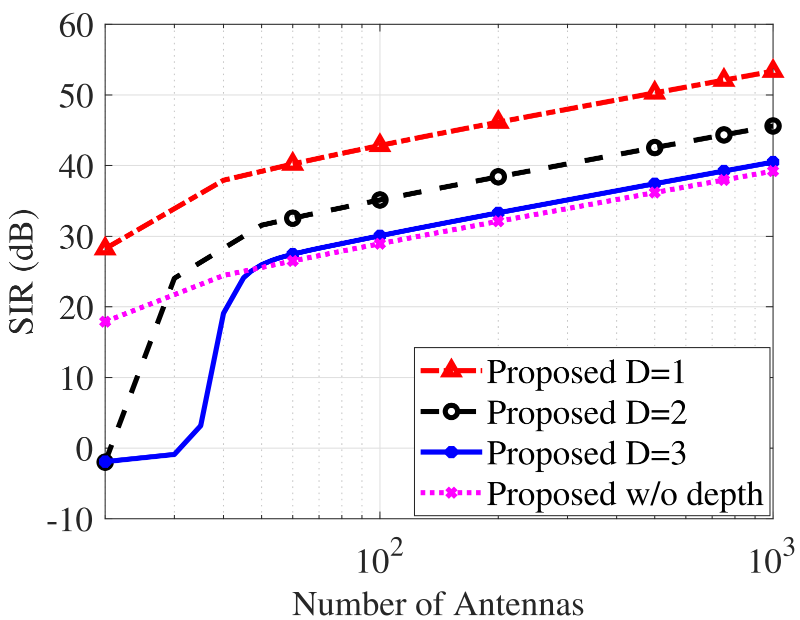

Fig. 3.3 SIR performance as a function of the number of BS antennas.

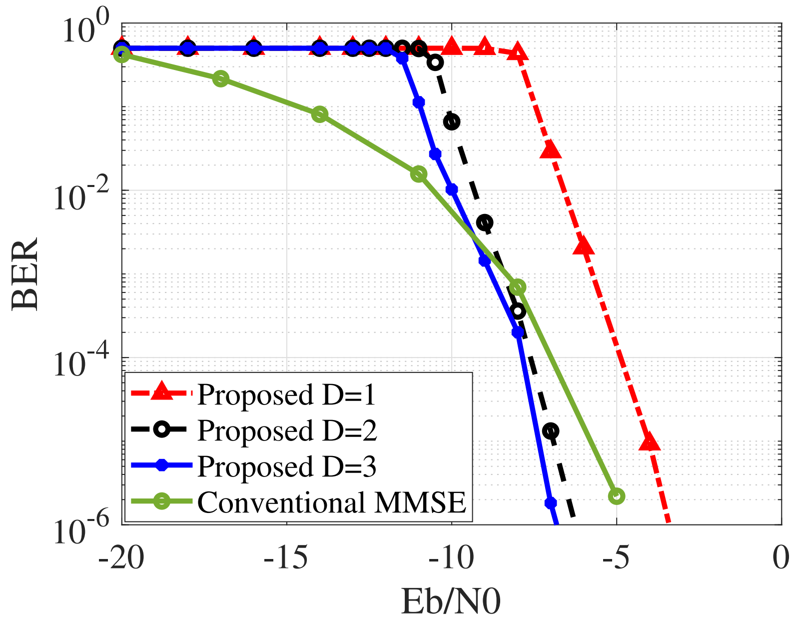

Fig. 3.4 BER performance for the proposed technique and MMSE combining.

mentation of *depth*. When *depth* is not implemented, only one sliding direction is considered, where one estimate of the data symbol at each subcarrier is obtained, i.e., the output is derived from $\widehat{\mathbf{X}}_m = \mathbf{\Psi}_1^{-1}\mathbf{\Phi}_{m-1}^{\text{MMSE}}\overline{\mathbf{Y}}m$. An input SNR of 0 dB was used. The results in Fig. 3.2 show that noise and multiuser interference can be effectively averaged out by the proposed technique as the number of BS antennas increases. Additionally, the proposed technique without the implementation of *depth* can achieve performance very close to that of the conventional MMSE combiner. However, with $D = 1, 2$, and 3, the proposed technique results in an SINR performance gain of around 2dB compared to the conventional MMSE combining. It is worth noting that the SINR performance becomes linear only after a minimum number of BS antennas is deployed. This is due to error propagation at the channel estimation stage in (3.30), highlighting the benefit of increasing depth, as it significantly improves SINR performance, especially when considering fewer BS antennas or lower input SNR. Furthermore, frequency diversity predominantly averages out the channel estimation noise in (3.4). However, as shown in Fig. 3.3, in the absence of noise, increasing depth negatively impacts the signal to interference ratio (SIR). This occurs due to the approximation in (3.12). The conventional LS channel estimation and MMSE combining result in infinite SIR in the absence of noise and, thus, are not included in Fig. 3.3.

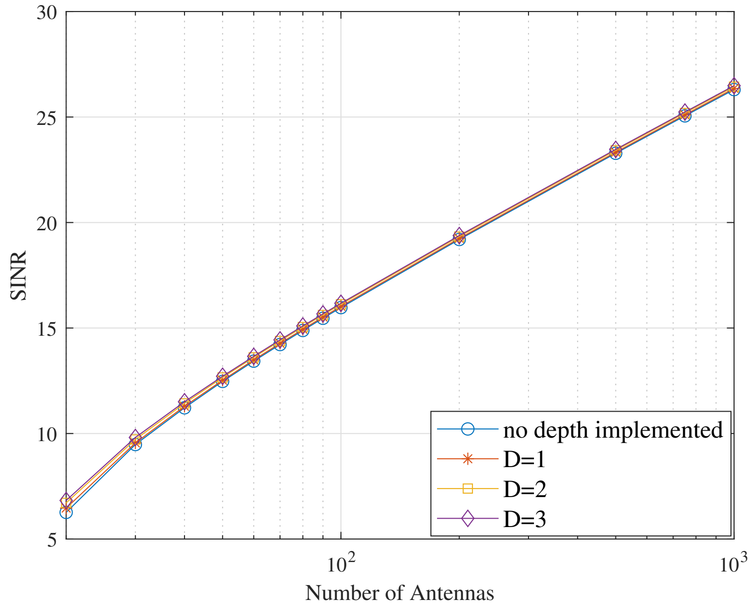

Fig. 3.5 SINR performance of the conventional method with the implementation of depth.

In Fig. 3.4, the BER performance of the proposed technique is analyzed when $Q = 200$ BS antennas are deployed. With $D = 3$, the proposed technique results in a 2 dB performance gain at higher Eb/N0s compared to the conventional method. These results demonstrate that increasing D from 1 to 3 provides nearly 4 dB performance gain.

Fig. 3.5 shows that implementation of depth in conventional LS- channel estimation technique with MMSE combining is not effective. The conventional LS channel estimation with MMSE combining is implemented in a manner similar to the proposed technique, using depth as a parameter. In Fig. 3.5, the SINR performance of the conventional method versus the number of BS antennas with and without implementation of depth are evaluated. The results show that even when implementing D = 3, the SINR performance improvement is negligible. Hence, the implementation of depth is not beneficial in this scenario.

In the previous simulations, the performance of the proposed technique was only analyzed under the ETU channel model, as it is the most hostile channel among other 3GPP channel models [44]. This is due to the fact that ETU channel has the smallest coherence bandwidth ($F_c \approx 200$ kHz) when compared to other 3GPP standard channel models [44], such as Extended Pedestrian A (EPA) with coherence bandwidth 12 times that of ETU ($F_c \approx 2.4$ MHz) and EVA with coherence bandwidth twice as large as that of ETU ($F_c \approx 400$ kHz). Hence, among these channel models, ETU

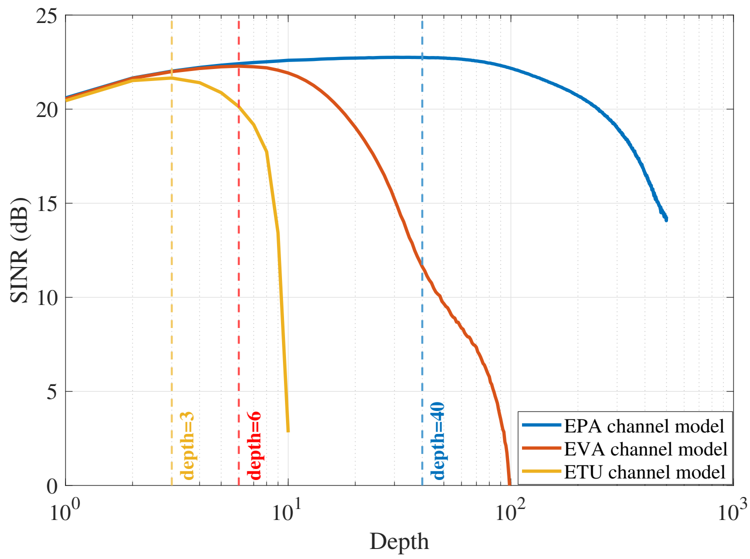

Fig. 3.6 SINR performance as a function of depth D.

accommodates the smallest number of subcarriers within its coherence bandwidth. This reduces the frequency diversity and consequently, it reduces the gains from depth implementation in ETU channel model. Furthermore, since ETU channel is highly frequency-selective, it requires a large number of pilots when conventional LS-based channel estimation methods are deployed since the channel length L becomes larger.

To study the effect of depth under different channel conditions, the SINR performance versus depth for all the 3GPP channel models, i.e., ETU, EPA andEVA, are compared in Fig. 3.6. In all channel scenarios, $Q = 200$ BS antennas are deployed. For the ETU model, the best performance is achieved for $D = 3$ and the performance degrades sharply thereafter. On the other hand, the EVA model achieves the highest SINR at $D = 6$ and the performance drops sharply as D increases. It is worth noting that the EVA model was considered solely for its coherence bandwidth size. Hence, it was simulated in a static scenario, i.e., zero Doppler was considered. Finally, for the EPA channel model, maximum SINR is achieved at a depth of $D = 40$. The highest SINR performance achieved for each channel model was marked with a dashed vertical line having the same color as the respective curve in Fig. 3.6. As mentioned earlier, the EVA and EPA channel models have 2 and 12 times larger coherence bandwidth than the ETU channel model, respectively. These ratios are in agreement with the ratios of the depth, D, at which the maximum SINR is achieved for each channel model.

3.6 Conclusion

In this Chapter, a sliding joint channel estimation and equalization technique was proposed to significantly reduce pilot overhead in massive MIMO. First, this chapter demonstrated that data symbols on adjacent subcarriers can be detected using linear combining and CFR estimates on a single reference subcarrier. This is possible due to the fact that the subcarrier spacing is considerably shorter than the coherence bandwidth of the channel. Therefore, the correlation between the channel of subcarriers within the coherence bandwidth has values close to one. This is while the derivations of this chapter also show that in the asymptotic regime, as the number of BS antennas tends to infinity, MRC combining results in the channel correlation. Hence, the above derivations lead to the conclusion that the CFR at a single subcarrier can be used to estimate the data of a band of adjacent subcarriers. The detected adjacent data symbols were then used as virtual pilots to update their corresponding channel estimates. The updated CFRs were subsequently employed for the equalization of the remaining data symbols in a sliding manner. This method can effectively estimate the channel and the data symbols of the transmitted frame using only a single reference pilot subcarrier, effectively reducing by almost two orders of magnitude the pilot overhead compared to conventional methods.

Apart from reducing the pilot overhead, it was shown in this chapter that the proposed method is capable of efficiently taking advantage of frequency diversity. This is because the joint channel estimation and equalization approach generates multiple estimates of the transmitted data symbols at each subcarrier, which are averaged to provide additional frequency diversity, supplementing the spatial diversity gains of massive MIMO. Naturally, the number of different subcarrier CFRs that can be used in the averaging is strictly limited by the coherence bandwidth. Hence, the term *depth* was proposed to determine the number of adjacent subcarriers utilized for the averaging. Additionally, the derivations of this chapter showed that conventional techniques can only fully take advantage of the frequency diversity when a pilot is transmitted in every subcarrier. When only the minimum required number of pilots are transmitted, i.e., $m_\mathrm{P} = L$, the channel estimation noise between different CFRs becomes highly correlated. In other words, the noise term will not be averaged out after combining.

Through extensive numerical analysis, it was demonstrated that the proposed technique achieves similar SINR and BER performance compared to conventional linear combiners when depth is not implemented. However, with the implementation of depth, the simulation results showed that the proposed method surpasses the SINR and BER performance of conventional methods. Furthermore, simulation results also corroborate the claims that frequency diversity is not effective in conventional linear combiners. When depth is implemented in these systems, the simulation results show no improvements in SINR performance. Finally, it was also shown the benefits of depth in different channel scenarios, where the channel coherence bandwidth differs. When the coherence bandwidth increases, a larger depth size leads to a larger SINR performance gain.

In this chapter, a novel method was proposed for contemporary wireless systems and services, where the channel is approximately constant over multiple subcarriers. However, as the wireless communications systems progress, new challenges emerge. In future network systems, emerging applications such as bullet trains, autonomous driving, and Integrated satellite, aerial, and terrestrial networks face the common issue of high mobility scenarios. In such cases, the channel Doppler spread makes the channel coefficients rapidly time-varying, leading to substantial signaling overhead to manage these variations. Furthermore, most techniques aimed at 4G and 5G systems, including the one proposed in this chapter, suffer severely from the interference caused by the Doppler spread. Therefore, in the following chapters, novel approaches are introduced to reduce the signaling overhead when significant delay and Doppler spreads are present in the channel.

Chapter 4

OTFS Without CP in Massive MIMO

The new generation of services and applications in 6G mobile systems presents many challenging requirements, including extremely low latency and ultra-high reliability of wireless links [1, 14]. These challenges are more noticeable in mission-critical applications such as autonomous driving that require safe and rapid reactions and cannot tolerate the wireless link becoming unreliable. Loss of reliability can be due to the fast time variations of the channel caused by mobility. Dealing with time-varying channels has a long history and rigorous foundations in the development of time-frequency domain signaling schemes, [7, 43, 90]. However, conventional solutions require fast channel tracking and/or large signaling overheads leading to significant latency issues.

As one of the key building blocks that will underpin next-generation networks, the air interface needs to be highly resilient to inherent wireless channel-fading effects, i.e. multipath and Doppler effects. Unlike the LTI channel scenario discussed in the previous chapter, channels with high Doppler effects introduce fast variations in the channel response, making channel estimation and equalization significantly more challenging. Furthermore, the Doppler spread disrupts many of the advantageous properties of mainstream technologies from 4G and 5G systems, such as the single-tap equivalent channel in OFDM. This motivates the need for a more robust waveform. Thus, the focus of this chapter is on the new waveform called OTFS [11]. As shown in Chapter 2, OTFS deploys the data in DD instead of the time-frequency domain. This has the interesting benefit of making the channel response in this domain sparse and time-invariant, [11, 18, 66]. Furthermore, OTFS can be implemented on top of OFDM and its signal can be formed by concatenating multiple OFDM symbols in time. However, OFDM may suffer from bandwidth efficiency loss due to its redundant

CP, whose length can be up to 25% of the symbol duration in its extended form as devised in the recent 3GPP 5G NR standard [25].

An important point to note is that the CP overhead makes the symbols longer and hence the time variation of the channel from one symbol to the next is increased. Additionally, the presence of CP can become a bottleneck when shortening the OFDM symbols within each OTFS block, i.e., each OTFS time slot, to tackle the time variations of the channel. Therefore, the authors in [26] have shown that the CP overhead can be reduced to only one CP at the beginning of each OTFS block instead of having multiple CPs within one block of OTFS. Recently, the authors in [29] have shown that in massive MIMO systems one can dispense with the redundant CP of OFDM by application of TR-MRC in LTI channels. In a more recent work, the authors in [30] extended the results of [29] to single carrier transmission in LTI channels. Time reversal is a technique that compresses the channel impulse response, concentrating the signal energy in one point. Paired with massive MIMO, which by itself can average out the effects of noise and MUI by deploying a large number of antennas at the BS, can effectively average out the delay spread of the channel. Motivated by the need to reduce the signaling overhead of OTFS and alternative ways to deal with Doppler spread, this chapter answers the following research question.

Can TR-MRC average out doubly spread channel effects and break the Doppler limitations of OTFS?

In this chapter, TR-MRC is proposed as a solution to completely remove CP of OTFS-based massive MIMO systems. Assuming locally LTI channels over each symbol within the OTFS blocks, it was demonstrated that both the delay and Doppler spread of the channel at the time-reversal combiner output average out as the number of receive antennas grows large. However, for considerably large Doppler shifts, this assumption does not hold and a residual Doppler effect remains after time-reversal combining. The numerical analysis in the asymptotic regime showed that this effect reduces to scaling of the received symbols in the delay dimension with the samples of a Bessel function that depends on the maximum Doppler frequency. Based on this observation, a novel solution to the Doppler limitation of OTFS is proposed through the application of a RDC window. It is worth noting that time reversal focuses the delay spread into a single point using a convolution function in the delay-time domain. As shown in Chapter 2, the OTFS equivalent channel can be represented as a 2D circular convolution. This raises the idea of performing time reversal as a

2D convolution in the DD domain, focusing the effect of both the delay and Doppler spread of the channel into a single point. Hence, this chapter also shows how TR-MRC can be performed in the DD domain as a 2D circular convolution and compares the computational complexity of the DD domain implementation with the time-frequency domain implementation.

4.1 OTFS-based Massive MIMO

Consider an OFDM-based OTFS system in a large scale MIMO setup where a single antenna user is communicating with a BS that is equipped with Q antennas. To better cope with the time variations of the channel, the OFDM symbols are shortened by removing the CP overhead. Let the $M \times N$ matrix $\mathbf{X}$ contain the QAM data symbols in the DD domain. The elements of $\mathbf{X}$ are i.i.d. zero-mean complex random variables of unit variance. In the first stage of OTFS modulation, the data symbols are first mapped to the time-frequency plane with N time slots and M frequency bins by an inverse symplectic finite Fourier transform (ISFFT) operation, [11]. This can be implemented by performing M-point DFT and N-point IDFT operations along the columns and rows of $\mathbf{X}$, respectively, i.e., $\mathbf{F}_M\mathbf{X}\mathbf{F}_N^{\mathrm{H}}$. In this first stage, OTFS is performed with rectangular transmit and receive window functions. The resulting time-frequency samples are then fed into an OFDM modulator and the OTFS transmit signal in the absence of CP is formed as

$$\mathbf{S} = \mathbf{F}_M^{\mathrm{H}}(\mathbf{F}_M\mathbf{X}\mathbf{F}_N^{\mathrm{H}}) = \mathbf{X}\mathbf{F}_N^{\mathrm{H}}. \tag{4.1}$$

Hence, the OFDM-based OTFS modulation reduces to N-point IDFT operations along the rows of $\mathbf{X}$, [23]. After parallel-to-serial conversion of $\mathbf{S}$, the transmit signal can be formed as $\mathbf{s} = [\mathbf{s}_0^{\mathrm{T}}, \ldots, \mathbf{s}_{N-1}^{\mathrm{T}}]^{\mathrm{T}}$ where $\mathbf{s}_n$ indicates the n^{th} column of $\mathbf{S}$, i.e.,

$$\mathbf{s}_n = \mathbf{X}\mathbf{f}_{N,n}^* = \frac{1}{\sqrt{N}}\sum_{i=0}^{N-1}\mathbf{x}_i e^{\frac{j2\pi ni}{N}}, \tag{4.2}$$

and $\mathbf{x}_i$ denotes the i^{th} column of $\mathbf{X}$.

After the digital-to-analog conversion of the signal $\mathbf{s}$, the continuous-time baseband signal, $s(t)$ goes through the LTV channel. Considering the same SNR and statistically independent channels between the mobile terminal and the BS antennas, the received signal at the BS antenna q can be written as

$$r_q(t) = \int\int h_q(\tau,\upsilon)s(t-\tau)e^{j2\pi\upsilon(t-\tau)}d\upsilon d\tau + \eta_q(t), \tag{4.3}$$

where $\eta_q(t)$ is the AWGN, and

$$h_q(\tau,\upsilon) = \sum_{p=0}^{P-1} \alpha_{p,q}\delta(\tau-\tau_{p,q})\delta(\upsilon-\upsilon_{p,q}) \tag{4.4}$$

is the sparse channel response with P paths in DD domain between the user and BS antenna q. The parameters $\alpha_{p,q}$, $\tau_{p,q}$ and $\upsilon_{p,q}$ represent the path gains, delays, and Doppler shifts of path p at antenna q, respectively. It is assumed the same PDP for the channels between the user and all the BS antennas and the path gains at different antennas to be i.i.d. complex Gaussian random variables with zero mean and variance of $\rho(p)$, i.e., $\alpha_{p,q} \sim \mathcal{CN}(0,\rho(p)), \forall q$. Considering a normalized PDP, $\boldsymbol{\rho} = [\rho(0), ..., \rho(P-1)]^{\mathrm{T}}$ where $\sum_{p=0}^{P-1}\rho(p) = 1$. In practical systems, the sampling period is short enough to approximate the path delays to the nearest sampling points. Consequently, fractional delays are not considered, and each $\tau_{p,q}$ is approximated as an integer multiple of the sampling period T_{s}, i.e., $\tau_{p,q} \approx \ell_{\tau_{p,q}}T_{\mathrm{s}}$ where $\ell_{\tau_{p,q}} \in [0, L-1]$ and L is the number of delay taps after discretization [40]. Thus, the received signal at antenna q after analog-to-digital conversion with the sampling period T_{s}, i.e., $r_q(\ell T_{\mathrm{s}}) = r_q[\ell]$, can be expressed as

$$r_q[\ell] = \sum_{k=0}^{L-1} h_q[k,\ell]s[\ell-k] + \eta_q[\ell], \tag{4.5}$$

where

$$h_q[k,\ell] = \sum_{p=0}^{P-1} \alpha_{p,q}e^{j2\pi\upsilon_{p,q}(\ell-k)T_{\mathrm{s}}}\delta[k-\ell_{\tau_{p,q}}] \tag{4.6}$$

is the channel response in delay-time domain and $h_q[k,\ell] = 0$ for any $k \notin [0, L-1]$.

After serial-to-parallel conversion of each received OTFS block of size MN samples at a given antenna q, an $M \times N$ matrix $\mathbf{R}_q = [\mathbf{r}_{0,q}, \ldots, \mathbf{r}_{N-1,q}]$ with the columns $\mathbf{r}_{n,q} = [r_q[nM], \ldots, r_q[(n+1)M-1]]^{\mathrm{T}}$ is formed. In the first stage of OTFS demodulation, the columns of $\mathbf{R}_q$ are fed into an OFDM demodulator to obtain the received signal in the time-frequency domain as $\mathbf{F}_M\mathbf{R}_q$. The resulting signal samples are then translated to the DD domain at the second OTFS demodulation stage through an SFFT operation,

$$\hat{\mathbf{X}}_q = \mathbf{F}_M^{\mathrm{H}}(\mathbf{F}_M\mathbf{R}_q)\mathbf{F}_N = \mathbf{R}_q\mathbf{F}_N, \tag{4.7}$$

where $\hat{\mathbf{X}}_q = [\hat{\mathbf{x}}_{0,q}, ..., \hat{\mathbf{x}}_{N-1,q}]$ and

$$\hat{\mathbf{x}}_{n,q} = \mathbf{R}_q \mathbf{f}_{N,n} = \frac{1}{\sqrt{N}} \sum_{i=0}^{N-1} \mathbf{r}_{i,q} e^{\frac{-j2\pi ni}{N}}. \tag{4.8}$$

4.2 Proposed TR-MRC with RDC Windowing

In this section, TR-MRC is applied to an OFDM-based OTFS without the addition of CP. The output and analysis show that the interference caused by both delay spread, i.e., ISI and inter block interference (IBI), and time variations of the channel can be effectively alleviated as the number of BS antennas grows large.

Considering the received OFDM symbol n at antenna q with the samples due to the transient of the channel from (4.5), the $(M + L - 1) \times 1$ vector $\tilde{\mathbf{r}}_{n,q} = [r_q[nM], \ldots, r_q[(n+1)M + L - 2]]^{\mathrm{T}}$ can be obtained as

$$\tilde{\mathbf{r}}_{n,q} = \mathbf{H}_{n,q}^{(n,n-1)} \mathbf{s}_{n-1} + \mathbf{H}_{n,q}^{(n,n)} \mathbf{s}_n + \mathbf{H}_{n,q}^{(n,n+1)} \mathbf{s}_{n+1} + \boldsymbol{\eta}_{n,q}. \tag{4.9}$$

The $(M + L - 1) \times M$ convolution matrices $\mathbf{H}_{n,q}^{(n,n)}$, $\mathbf{H}_{n,q}^{(n,n-1)}$ and $\mathbf{H}_{n,q}^{(n,n+1)}$ when multiplied to the symbols $\mathbf{s}_n$, $\mathbf{s}_{n-1}$ and $\mathbf{s}_{n+1}$ form the channel affected symbol n, the tail of the symbol $n-1$ that overlaps with the first $L-1$ samples of the symbol n, and the first $L-1$ samples of the symbol $n+1$ that overlap with the tail of the symbol n, respectively. The elements of these matrices are represented as

$$\begin{aligned} [\mathbf{H}_{n,q}^{(n,n)}]_{ab} &= h_q[a-b, Mn+a], \\ [\mathbf{H}_{n,q}^{(n,n-1)}]_{ab} &= h_q[M-b+a, Mn+a], \\ [\mathbf{H}_{n,q}^{(n,n+1)}]_{ab} &= h_q[a-b-M, Mn+a], \end{aligned} \tag{4.10}$$

where $a = 0, \ldots, M+L-2$ and $b = 0, \ldots, M-1$. It is worth mentioning that these matrices follow a Toeplitz-like structure (but, not quite Toeplitz because of the time variation of the channel) as shown in (4.11), (4.12) and (4.13). In these matrices, each diagonal represents a channel tap that varies every sample according to its respective Doppler shift. As mentioned earlier, the absence of CP leads to IBI between OTFS blocks apart from ISI. This effect is represented using the same matrices as the ones that are shown in (4.9). Hence, IBI is treated in the same way as ISI.

In the following subsections, OTFS without CP is asymptotically analyzed using TR-MRC as the number of BS antennas tends to infinity for both LTI and LTV channels. Based on the derivations and analysis, a novel windowing technique tailored

$$\mathbf{H}_{n,q}^{(n,n-1)} = \begin{bmatrix} 0 & \dots & h_q[L-1, Mn] & \dots & h_q[1, Mn] \\ \vdots & \ddots & \ddots & \ddots & \vdots \\ 0 & \ddots & \ddots & \ddots & h_q[L-1, Mn+L-2] \\ \vdots & \ddots & \ddots & \ddots & \vdots \\ 0 & \dots & \dots & \dots & 0 \end{bmatrix}, \tag{4.11}$$

$$\mathbf{H}_{n,q}^{(n,n)} = \begin{bmatrix} h_q[0, Mn] & \dots & 0 \\ \vdots & \ddots & \vdots \\ h_q[L-1, Mn+L-1] & \ddots & 0 \\ \vdots & \ddots & \vdots \\ 0 & \ddots & h_q[0, M(n+1)-1] \\ \vdots & \ddots & \vdots \\ 0 & \dots & h_q[L-1, M(n+1)+L-2] \end{bmatrix}, \tag{4.12}$$

$$\mathbf{H}_{n,q}^{(n,n+1)} = \begin{bmatrix} 0 & \dots & \dots & \dots & 0 \\ \vdots & \ddots & \ddots & \ddots & \vdots \\ 0 & \ddots & \ddots & \ddots & 0 \\ h_q[0, M(n+1)] & \ddots & \ddots & \ddots & 0 \\ \vdots & \ddots & \ddots & \ddots & \vdots \\ h_q[L-2, M(n+1)+L-2] & \dots & h_q[0, M(n+1)+L-2] & \dots & 0 \end{bmatrix}, \tag{4.13}$$

to the channel correlation function is proposed to address the residual Doppler effect caused by the time variations of the channel within each OFDM symbol.

4.2.1 TR-MRC for OTFS in LTI channels

For an LTI channel, there is no time variation over the OTFS blocks, i.e., $h_q[k,m] = h_q[k,m']$, $\forall k, m$ and m'. Thus, the convolution matrices in 4.11, 4.12 and 4.13 become Toeplitz matrices. In TR-MRC, the received signals on the BS antennas q for OFDM time symbol n are first pre-filtered with the corresponding time-reversed and conjugated CIRs. Then the resulting signals at different antennas are combined and the first $L-1$ samples at the filter output, i.e., the time-reversal filter transient, are discarded by the rectangular window $\mathbf{W} = [\mathbf{0}_{M\times(L-1)}, \mathbf{I}_M]$. Thus, obtaining

$$\mathbf{r}_n^{\mathrm{TR}} = \frac{1}{Q}\sum_{q=0}^{Q-1} \mathbf{W}\mathbf{H}_{n,q}^{\mathrm{TR}}\tilde{\mathbf{r}}_{n,q}, \tag{4.14}$$

where the time-reversal filter for antenna q can be represented by $\mathbf{H}_{n,q}^{\mathrm{TR}}$ with the elements $[\mathbf{H}_{n,q}^{\mathrm{TR}}]_{ab} = h_q^*[L-1-(a-b), 0]$ that are independent of n, for $a, b = 0, ..., M+L-2$.

Substituting $\tilde{\mathbf{r}}_{n,q}$ from (4.9) into (4.14), obtaining

$$\mathbf{r}_n^{\mathrm{TR}} = \mathbf{G}_n^{(n,n-1)}\mathbf{s}_{n-1} + \mathbf{G}_n^{(n,n)}\mathbf{s}_n + \mathbf{G}_n^{(n,n+1)}\mathbf{s}_{n+1} + \boldsymbol{\eta}'_n, \tag{4.15}$$

where

$$\begin{aligned}
\mathbf{G}_n^{(n,n-1)} & \frac{1}{Q}\sum_{q=0}^{Q-1} \mathbf{W}\mathbf{H}_{n,q}^{\mathrm{TR}}\mathbf{H}_{n,q}^{(n,n-1)}, \\
\mathbf{G}_n^{(n,n)} &= \frac{1}{Q}\sum_{q=0}^{Q-1} \mathbf{W}\mathbf{H}_{n,q}^{\mathrm{TR}}\mathbf{H}_{n,q}^{(n,n)}, \\
\mathbf{G}_n^{(n,n+1)} &= \frac{1}{Q}\sum_{q=0}^{Q-1} \mathbf{W}\mathbf{H}_{n,q}^{\mathrm{TR}}\mathbf{H}_{n,q}^{(n,n+1)}, \\
\boldsymbol{\eta}'_n &= \frac{1}{Q}\sum_{q=0}^{Q-1} \mathbf{W}\mathbf{H}_{n,q}^{\mathrm{TR}}\boldsymbol{\eta}_{n,q}.
\end{aligned} \tag{4.16}$$

The elements of the matrices are given by $[\mathbf{G}_n^{(n,n-1)}]_{a,b} = g[M+a-b, 0]$, $[\mathbf{G}_n^{(n,n)}]_{a,b} = g[a-b, 0]$ and $[\mathbf{G}_n^{(n,n+1)}]_{a,b} = g[a-b-M, 0]$ for $a, b = 0, \ldots, M-1$, and $g[i, 0] =$

$\frac{1}{Q}\sum_{q=0}^{Q-1}\sum_{k=0}^{L-1} h_q[k,0]h_q^*[k-i,0]$ represents the channel correlation function after combining.

As the number of BS antennas Q tends to infinity, due to the law of large numbers, the equivalent time-reversal combining matrices in (4.15) converge almost surely to the respective expected value. Hence, as Q tends to infinity, $\mathbf{G}_n^{(n,n)}$ tends to an identity matrix while $\mathbf{G}_n^{(n,n-1)}$ and $\mathbf{G}_n^{(n,n+1)}$ tend to zero. This is due to the fact that the elements on the main diagonal of $\mathbf{G}_n^{(n,n)}$,

$$[\mathbf{G}_n^{(n,n)}]_{b,b} \to \sum_{k=0}^{L-1} \mathbb{E}\{h_q[k,0]h_q^*[k,0]\} = \sum_{p=0}^{P-1} \mathbb{E}\{|\alpha_{p,q}|^2\} = 1 \text{ as } Q \to \infty, \tag{4.17}$$

while the off-diagonal elements of $\mathbf{G}_n^{(n,n)}$ tend to sum of uncorrelated terms of the form $\mathbb{E}\{h_q[k,0]h_q^*[j,0]\} = \mathbb{E}\{\alpha_{p,q}\alpha_{p',q}^*\} = 0$ when $k \neq j$ and $p \neq p'$.

Finally, TR-MRC output signal is fed into the OTFS demodulator to retrieve the DD data symbols,

$$\hat{\mathbf{x}}_n^{\mathrm{TR}} = \frac{1}{\sqrt{N}} \sum_{i=0}^{N-1} \mathbf{r}_i^{\mathrm{TR}} e^{\frac{-j2\pi ni}{N}}. \tag{4.18}$$

Based on the above discussion, when $Q \to \infty$, $\mathbf{r}_i^{\mathrm{TR}} \to \mathbf{s}_i$ and hence the transmit symbols can be perfectly recovered.

4.2.2 TR-MRC with RDC windowing for OTFS in LTV channels

As opposed to LTI channels, time variations of LTV channels make it impossible to achieve temporal focusing with the same time-reversal filtering procedure as in Section 4.2.1. Additionally, it is impossible to estimate the channel gains at each single time sample ℓ, i.e., $h[k,\ell]$. Thus, it is assumed an approximately constant CIR over each OFDM symbol and the channel response to be known at the delay sample $M_{\mathrm{P}} \in [0, M-1]$ in a given OFDM symbol n where M_{P} is the position of the isolated pilot symbol that is used for channel estimation, [75]. Relying on the near constant CIR within each OFDM symbol, the time-reversal filtering matrix for a given OFDM symbol n can be defined as $[\mathbf{H}_{n,q}^{\mathrm{TR}}]_{ab} = h_q^*[L-1-(a-b), Mn+M_{\mathrm{P}}]$. Then, substituting this time-reversal filter into (4.14) while considering the received signal in (4.9) when the channel is LTV.

In contrast to the LTI channels, the correlation function of the LTV channels depends on the statistical properties of an additional random variable $\upsilon_{p,q}$. It is worth noting that the channel gains $\alpha_{p,q}$ and Doppler shifts $\upsilon_{p,q}$ at all the paths p and all the BS antennas are independent with respect to one another. Therefore, $\mathbb{E}\{\alpha_{p,q}\Gamma(\upsilon_{p,q})\} = \mathbb{E}\{\alpha_{p,q}\}\mathbb{E}\{\Gamma(\upsilon_{p,q})\}$ for any measurable function of $\upsilon_{p,q}$, $\Gamma(\upsilon_{p,q})$. Similar to the derivations in Section 4.2.1, as $Q \to \infty$, the elements of the equivalent channel matrices in (4.15), for LTV channels, tend to zero except for the diagonal elements of $\mathbf{G}_n^{(n,n)}$, i.e.,

$$\begin{aligned}
[\mathbf{G}_n^{(n,n)}]_{b,b} &= \frac{1}{Q}\sum_{q=0}^{Q-1}\sum_{k=0}^{L-1} h_q[k, Mn+b]h_q^*[k, Mn+M_{\mathrm{P}}] \\
&= \frac{1}{Q}\sum_{q=0}^{Q-1}\sum_{k=0}^{L-1}\sum_{p=0}^{P-1} e^{j2\pi(\upsilon_{p,q}(Mn+b-Mn-M_{\mathrm{P}}))T_{\mathrm{s}}} \\
&\quad \times \alpha_{p,q}\alpha_{p,q}^*\delta[k-\ell_{\tau_{p,q}}] \\
&= \frac{1}{Q}\sum_{q=0}^{Q-1}\sum_{k=0}^{L-1}\sum_{p=0}^{P-1} |\alpha_{p,q}|^2 e^{j2\pi\upsilon_{p,q}(b-M_{\mathrm{P}})T_{\mathrm{s}}}\delta[k-\ell_{\tau_{p,q}}]. \qquad (4.19)
\end{aligned}$$

From (4.19), it can be observed that if the channel was LTI within each OFDM symbol, the same result as in the previous subsection would be achieved. However, in reality, the channel time variations over each OFDM symbol leaves a residual Doppler effect at each path that is observed on the exponential term $e^{j2\pi\upsilon_{p,q}(b-M_{\mathrm{P}})T_{\mathrm{s}}}$ in (4.19). An in-depth understanding of this effect on the performance of TR-MRC can be obtained with the asymptotic derivations, which leads to my proposed RDC windowing technique.

As the number of BS antennas tends to infinity, the diagonal elements of $\mathbf{G}_n^{(n,n)}$ in (4.19),

$$[\mathbf{G}_n^{(n,n)}]_{b,b} \to \sum_{p=0}^{P-1} \mathbb{E}\{|\alpha_{p,q}|^2\}\mathbb{E}\{e^{j2\pi\upsilon_{p,q}(b-M_{\mathrm{P}})T_{\mathrm{s}}}\} \text{ as } Q \to \infty, \qquad (4.20)$$

where $\mathbb{E}\{|\alpha_{p,q}|^2\} = \rho(p)$. Thus, the term $\mathbb{E}\{e^{j2\pi\upsilon_{p,q}(b-M_{\mathrm{P}})T_{\mathrm{s}}}\}$ needs to be calculated. Considering the Jake's model, [46], for a given maximum Doppler frequency, $\upsilon_{\max}$, the Doppler frequency for path p and antenna q can be obtained as $\upsilon_{p,q} = \upsilon_{\max}\cos(\theta_{p,q})$, where $\theta_{p,q}$ is uniformly distributed within the range $[-\pi, \pi]$, i.e. $\theta_{p,q} \sim \mathcal{U}(-\pi, \pi)$.

Consequently,

$$\mathbb{E}\{e^{j2\pi\upsilon_{p,q}(b-M_{\mathrm{P}})T_{\mathrm{s}}}\} = \int_{-\infty}^{\infty} e^{j\beta\cos(\theta_{p,q})(b-M_{\mathrm{P}})} f(\theta_{p,q}) d\theta_{p,q}$$
$$= J_0(\beta(b-M_{\mathrm{P}})), \tag{4.21}$$

where $\beta = 2\pi\upsilon_{\max}T_{\mathrm{s}}$, $f(\theta_{p,q}) = \frac{1}{2\pi}$ is the probability density function of $\theta_{p,q}$ and $J_0(\cdot)$ denotes the zero-order Bessel function of the first kind. This result shows that, in the asymptotic regime, the residual Doppler effect is reduced to a real-valued attenuation function of the maximum Doppler frequency, given by

$$[\mathbf{G}_n^{(n,n)}]_{b,b} = \sum_{p=0}^{P-1} \rho(p) J_0(\beta(b-M_{\mathrm{P}})) = J_0(\beta(b-M_{\mathrm{P}})). \tag{4.22}$$

From (4.22), one may realize that, as Q grows large, the residual Doppler effect can be easily corrected by dividing the TR-MRC output with the diagonal elements of $\mathbf{G}_n^{(n,n)}$. Therefore, the RDC windowing technique is proposed to effectively compensate for the residual Doppler effect. This window can be straightforwardly integrated into the window $\mathbf{W}$ in (4.14) as $\mathbf{W} = [\mathbf{0}_{M\times L-1}, \mathbf{W}_J]$, where

$$\mathbf{W}_J = \mathrm{diag}\{[J_0^{-1}(-M_{\mathrm{P}}\beta), ..., J_0^{-1}((M-M_{\mathrm{P}}-1)\beta)]\}. \tag{4.23}$$

Finally, the transmit data symbols can be recovered in the same fashion as in (4.18). It is worth noting that the proposed RDC windowing technique in (4.23) brings substantial performance improvement for large relative velocities between the transmit and receive antennas. This relaxes the limitations of OTFS on the maximum Doppler frequency that it can tolerate.

4.3 Implementation in Delay Doppler Domain

In the previous section, TR-MRC and RDC windowing were performed in the delay-time domain, followed by the OTFS demodulation to retrieve the data in the DD domain. In this section, TR-MRC with RDC windowing technique is implemented in the DD domain where the wireless channels and the corresponding time reversal combiners become sparse and time-invariant.

Starting by substituting (4.14) in (4.18) to obtain

$$\hat{\mathbf{x}}_n^{\mathrm{TR}} = \frac{1}{Q\sqrt{N}} \sum_{q=0}^{Q-1} \sum_{i=0}^{N-1} \mathbf{W}\mathbf{H}_{i,q}^{\mathrm{TR}} \tilde{\mathbf{r}}_{i,q} e^{\frac{-j2\pi ni}{N}}. \tag{4.24}$$

It is worth noting that the matrices $\mathbf{H}_{i,q}^{\mathrm{TR}}$ are Toeplitz. Hence,

$$\mathbf{W}\mathbf{H}_{i,q}^{\mathrm{TR}} = \mathbf{W}\mathrm{circ}\{\bar{\mathbf{h}}_{i,q}\}, \tag{4.25}$$

where $\bar{\mathbf{h}}_{i,q}$ is the time reversal filter for the time symbol i in delay-time domain, padded by $M-1$ zeros, i.e., $\bar{\mathbf{h}}_{i,q} = [h_q^*[L-1, Mi+M_{\mathrm{P}}], \ldots, h_q^*[0, Mi+M_{\mathrm{P}}], \mathbf{0}_{1\times(M-1)}]^{\mathrm{T}}$. Considering the relationship between the DD and time-delay representations of the time reversal filter, i.e., $\bar{\mathbf{h}}_{i,q} = \sum_{k=0}^{N-1} \tilde{\mathbf{h}}_{k,q} e^{\frac{j2\pi ik}{N}}$, where $\tilde{\mathbf{h}}_{k,q}$ is the time reversal filter in the DD domain at Doppler bin k for antenna q, it can be obtained

$$\mathbf{W}\mathbf{H}^{\mathrm{TR}_{\mathrm{i,q}}} = \mathbf{W} \sum_{k=0}^{N-1} \mathrm{circ}\{\tilde{\mathbf{h}}_{k,q}\} e^{\frac{j2\pi ik}{N}}. \tag{4.26}$$

Substituting (4.26) into (4.24), results in

$$\begin{aligned} \hat{\mathbf{x}}_n^{\mathrm{TR}} &= \frac{1}{Q\sqrt{N}} \sum_{q=0}^{Q-1} \sum_{k=0}^{N-1} \mathbf{W}\mathrm{circ}\{\tilde{\mathbf{h}}_{k,q}\} \sum_{i=0}^{N-1} \tilde{\mathbf{r}}_{i,q} e^{\frac{-j2\pi(n-k)i}{N}} \\ &= \frac{1}{Q}\mathbf{W} \sum_{q=0}^{Q-1} \sum_{k=0}^{N-1} \mathrm{circ}\{\tilde{\mathbf{h}}_{k,q}\} \tilde{\mathbf{x}}_{((n-k))_N,q}, \end{aligned} \tag{4.27}$$

where $\tilde{\mathbf{x}}_{n,q} = \frac{1}{\sqrt{N}} \sum_{i=0}^{N-1} \tilde{\mathbf{r}}_{i,q} e^{\frac{-j2\pi ni}{N}}$. Due to the circulant properties from (4.27), the expresssion can be rewritten as a 2D convolution operation, i.e.,

$$\hat{\mathbf{X}}^{\mathrm{TR}} = \frac{1}{Q}\mathbf{W} \sum_{q=0}^{Q-1} (\boldsymbol{\mathcal{H}}_{\mathrm{q}}^{\mathrm{TR}} \overset{\mathrm{2D}}{\circledast} \tilde{\mathbf{X}}_q), \tag{4.28}$$

where $\tilde{\mathbf{X}}_q = [\tilde{\mathbf{x}}_{0,q}, \ldots, \tilde{\mathbf{x}}_{N-1,q}]$ and $\boldsymbol{\mathcal{H}}_{\mathrm{q}}^{\mathrm{TR}} = [\tilde{\mathbf{h}}_{0,q}, \ldots, \tilde{\mathbf{h}}_{N-1,q}]$ is the 2D time reversal filter that can be formed by conjugating and reversing the elements of the channel response along both delay and Doppler dimensions. This can be understood via the relationship between the delay-time and DD representations of the channel. In particular, when time reversal is performed along the delay dimension, it has the same effect in both the DD or the delay-time domain. This is while conjugation of the delay-time CIR translates into conjugation and reversal of the DD channel response along the Doppler dimension. This is in accordance to the time reversal and conjugation property of the DFT matrix, [39].

Due to the sparsity of the proposed time reversal filters in the DD domain, only a portion of them are significant and the rest can be approximated as zero at the expense of only a negligible loss in performance. In comparison, the delay-time counterparts of these filters are not sparse and all of them need to be considered to achieve satisfactory performance. An important point to note here is that TR-MRC implementation in the DD domain calls for 2D convolution operations while delay-time implementation involves linear convolution operations. Furthermore, DD implementation requires an OTFS demodulator per antenna while delay-time implementation consists of only one OTFS demodulator after combining. According to the above points, it is not clear which implementation leads to a lower computational load. Hence, in the next section, the computational complexity of the two implementations is analyzed in detail.

4.4 Delay-Time vs. Delay Doppler Implementation

This section studies the implementation complexity of TR-MRC in the DD domain versus in the delay-time domain. For both cases, it is considered that the channel is estimated in the DD domain through the EP-aided channel estimation technique [75]. Hence, the delay-time implementation requires the additional step of transforming the DD domain channel to the delay-time domain. However, the advantage of the delay-time implementation is that the TR-MRC combines the received signal of all receive antennas before demodulation. This way, only a single OTFS demodulator is required. Hence, the OTFS demodulation complexity is an important metric for comparing the two implementation options. To compute the demodulation complexity of the OTFS demodulator, the low-complexity OFDM-based demodulator proposed in [23] is considered. This way, a single DFT per delay block is required for the OTFS demodulation. Furthermore, the fast Fourier transform (FFT) algorithm is considered for efficient implementation of the DFT operations.

Each step of the implementation in the delay-time domain is shown in Fig. 4.1, with the complexity of each step listed in Table 4.1. When implementing in the delay-time domain, the first step is the time reversal operations, one at each of the Q BS antennas. This is followed by N RDC windowing operations with real-valued window coefficients over blocks of M samples. These steps require a total of $QNL(M + L - 1)$ and $\frac{MN}{2}$ complex multiplications (CMs), respectively. After

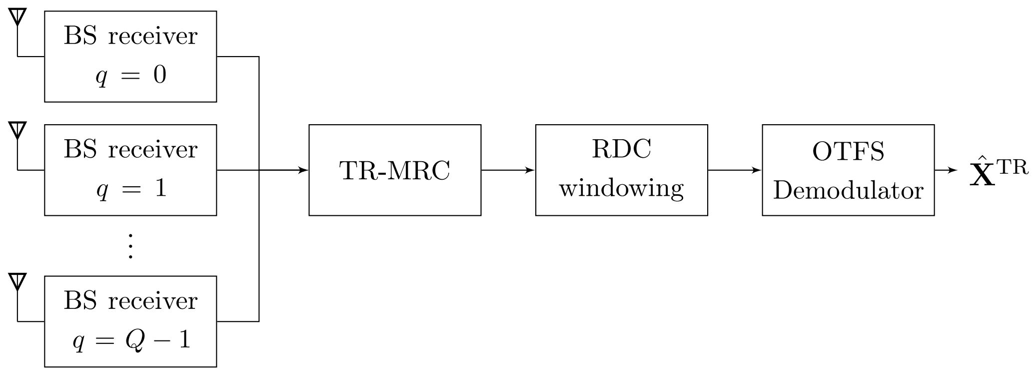

Fig. 4.1 Implementation steps of TR-MRC with RDC windowing in the delay-time domain.

Step	Number of Complex Multiplications
TR-MRC in delay-time domain	$QNL(M+L-1)$
RDC windowing	$\frac{MN}{2}$
OTFS demodulation	$\frac{MN}{2}\log_2 N$
Obtaining CIR from DD channel estimates	$\frac{QLN}{2}\log_2 N$

Table 4.1 Computational complexity of each step for implementing TR-MRC with RDC windowing in the delay-time domain.

combining, the signal is mapped to the DD domain through the OTFS demodulator, which requires $\frac{MN}{2}\log_2 N$ CMs [23]. Finally, it is necessary to take into consideration the complexity of obtaining the CIR from the DD channel estimates. Hence, an additional L number of N-point FFT operations at each BS antenna are required, adding up to $\frac{QLN}{2}\log_2 N$ CMs. Consequently, the total computational load of the proposed delay-time implementation is

$$\mathcal{C}_{\mathrm{dt}} = Q(\frac{LN}{2}\log_2 N + (M+L-1)NL) + \frac{MN}{2}(\log_2 N + 1). \tag{4.29}$$

Step	Number of Complex Multiplications
OTFS demodulation at each BS antenna	$\frac{Q(M+L-1)N}{2}\log_2 N$
2D time reversal in DD domain	$QN^2L(M+L-1)$
RDC windowing	$\frac{MN}{2}$

Table 4.2 Computational complexity of each step for implementing TR-MRC with RDC windowing in the DD domain.

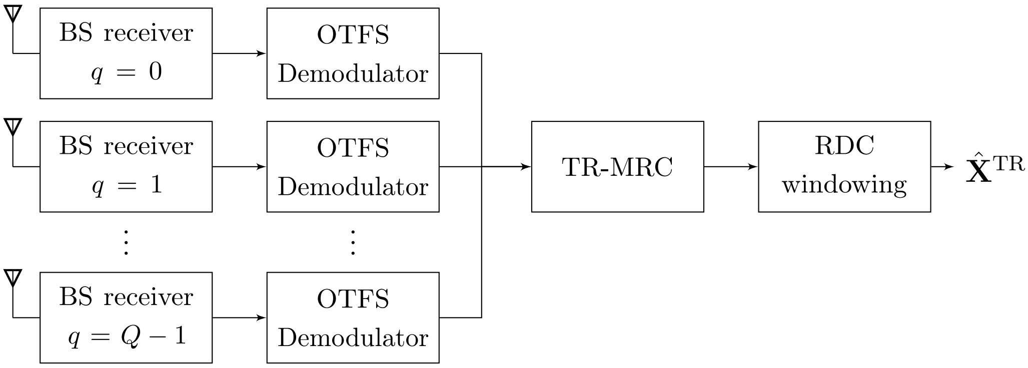

Fig. 4.2 Implementation steps of TR-MRC with RDC windowing in the DD domain.

Each step of the implementation in the DD domain is shown in Fig. 4.2, with the complexity of each step listed in Table 4.2. The DD implementation of the proposed technique starts with an OTFS demodulator at each BS antenna, which requires $\frac{Q(M+L-1)N}{2}\log_2 N$ CMs. This is followed by Q 2D time reversal operations and N RDC windowing operations with real-valued window coefficients over blocks of M samples in length. Hence, the TR-MRC with RDC windowing requires $QN^2L(M+L-1)$ and $\frac{MN}{2}$ CMs, respectively. Therefore, the total computational complexity of the DD implementation can be calculated as

$$\mathcal{C}_{\mathrm{dD}} = Q(\frac{(M+L-1)N}{2}\log_2 N + N^2L(M+L-1)) + \frac{MN}{2}. \tag{4.30}$$

From (4.30) it is evident that the operation that demands the largest computational load in the DD implementation is the 2D time reversal operation. In light of the channel sparsity in the DD domain, it can be misconstrued that the DD implementation of TR-MRC leads to a lower complexity than its delay-time counterpart. Comparing (4.29) and (4.30), it can be observed that the DD implementation of TR-MRC is N times more complex than its delay-time implementation. It is worth noting that in special cases, the Doppler spread can be limited to $N_{\mathrm{I}} < N$ Doppler bins, e.g., cases with only integer Doppler. In such cases, the size of the matrix $\boldsymbol{\mathcal{H}}_{\mathrm{q}}^{\mathrm{TR}}$ in (4.28) is reduced to a $L \times N_{\mathrm{I}}$ matrix. Hence, the 2D time reversal in the DD domain would require only $QNN_{\mathrm{I}}L(M+L-1)$ CMs. However, this is still N_{I} times more complex than its delay-time implementation. Therefore, it can be concluded that delay-time implementation is more suitable for practical systems.

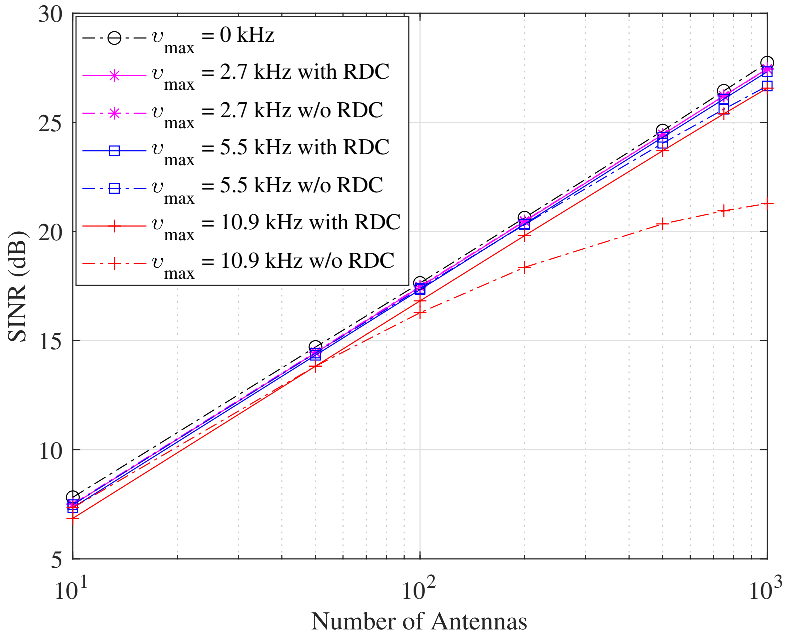

Fig. 4.3 SINR performance as a function of the number of BS antennas.

4.5 Numerical Analysis

In this section, the efficacy of TR-MRC with RDC windowing technique for OTFS without CP in massive MIMO is confirmed through extensive simulations. To model the channel, it is considered the EVA channel model [44], and the Doppler shift is generated using Jake's model [46]. In the simulation setup, a carrier frequency $f_c = 5.9$ GHz, subcarrier spacing $\Delta f = 15$ kHz, $M = 128$, $N = 64$ and $Q = 200$ are considered, unless otherwise stated. The transmission bandwidth is $B = 330\Delta f = 4.95$ MHz, 16-QAM modulation is deployed with 5 OTFS blocks per frame. For the relative speed of V km/h, the maximum Doppler shift can be obtained as $\upsilon_{\max} = f_c \frac{V}{3.6C}$ where $C \approx 3 \times 10^8$ m/s is the speed of light. It is assumed perfect knowledge of the delay-time channel responses at all the BS antennas in the middle of the delay dimension, i.e., $M_P = \frac{M}{2}$.

Fig. 4.3 shows a comparison between the SINR performance of OTFS as a function of the number of BS antennas for different maximum Doppler shifts with and without RDC windowing. SNR at the input is 1 dB. Based on the analytical results in Section 4.2, as the number of BS antennas grows large, TR-MRC can effectively average out the effect of ISI, IBI and time variations of the channel which is evident in Fig. 4.3. As the maximum Doppler shift increases, time variations of the channel within each OFDM symbol become more noticeable, and a residual Doppler effect

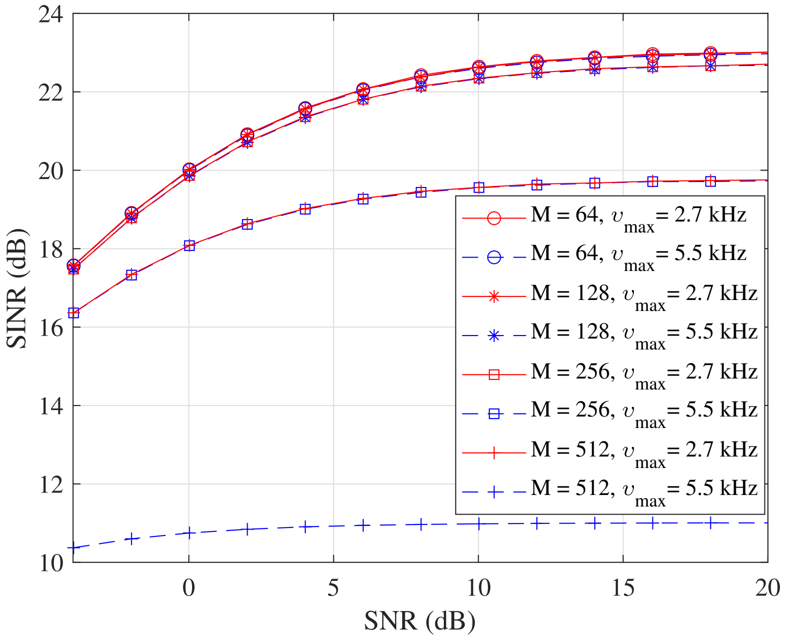

Fig. 4.4 SINR performance versus input SNR for different symbol durations.

remains after TR-MRC operation. As shown in Section 4.2, this effect can be corrected by utilizing my proposed RDC windowing technique. The efficacy of the proposed technique is confirmed by the results in Fig. 4.3 when the maximum Doppler shift is $\upsilon_{\max} = 10.9$ kHz which corresponds to the velocity of $V = 2000$ km/h at $f_c = 5.9$ GHz. It is worth noting that for $\upsilon_{\max} \leq 5.5$ kHz, corresponding to relative velocities up to $V = 1000$ km/h, the channel correlation resulting from the variations within each OFDM symbol is negligible. Consequently, the samples of the Bessel function in (4.22) take values close to 1 and the RDC windowing brings a marginal amount of improvement.

Fig. 4.4 shows the SINR performance of OTFS with TR-MRC versus input SNR for different values of $\upsilon_{\max}$ and M with a constant OTFS block size of $MN = 8192$. From Fig. 4.4 and (4.22), one may realize that every reduction/increase of the symbol duration, M, for a fixed $\upsilon_{\max}$, leads to the same result as if $\upsilon_{\max}$ was reduced/increased with a fixed M by the same proportion. This shows that the results for $\upsilon_{\max} = 10.9$ kHz when $M = 128$ would be the same for a smaller Doppler shift $\upsilon_{\max} = 2.7$ kHz, corresponding to $V = 500$ km/h, when $M = 512$. Additionally, it is worth noting that in millimeter wave bands $\upsilon_{\max} = 10.9$ kHz results from significantly lower speeds due to the high f_c values. However, when the Doppler shift is extremely large and/or symbol duration M is very long, the Bessel function coefficients lead to a large amount

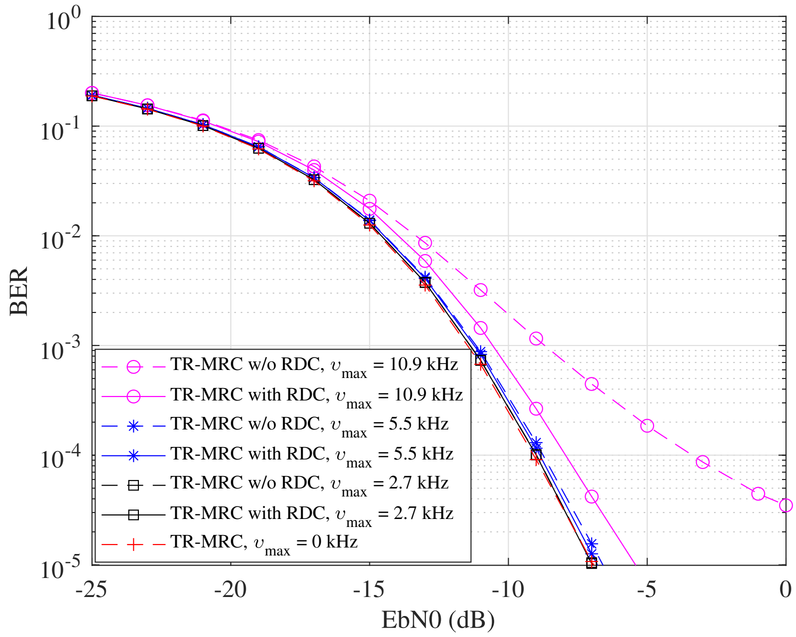

Fig. 4.5 BER performance with RDC windowing.

of attenuation and thus the RDC window may lead to noise enhancement issues. Hence, it is the designer's choice to adjust the symbol duration M and avoid or minimize the noise enhancement effects.

Finally, the BER performance of the proposed TR-MRC technique for OTFS in the absence CP, with and without RDC windowing, is analyzed in Fig. 4.5. It is shown that for non-zero maximum Doppler shifts $\upsilon_{\max} \leq 5.5$ kHz, the proposed TR-MRC technique leads to about the same BER performance as the static scenario. This is while for $\upsilon_{\max} \approx 11$ kHz, corresponding to the relative speed of $V = 2000$ km/h, the RDC windowing technique leads to the substantial performance improvement of over 5 dB at high SNRs. This shows that the proposed technique brings the BER performance very close to that of the static scenario even for very large amounts of Doppler spread.

4.6 Conclusion

The CP is undoubtedly a powerful tool that has two significant benefits in 5G systems. In particular, the CP can effectively avoid ISI and IBI, while making the equivalent LTI channel circulant, which significantly simplifies the equivalent frequency domain channel. However, in LTV channels, the CP loses the circulant channel benefits due to the channel aging problem. Furthermore, long CP sequences are a limiting factor when shorter symbol durations are required. A large number of studies in the OTFS literature consider the approximation of LTI channel per time slot, i.e., per OFDM symbol. However, as the maximum Doppler shift of the channel increases, the symbol duration must be reduced to maintain the validity of this approximation. Hence, solutions that can completely remove the CP become essential in high mobility scenarios.

With this in mind, the TR-MRC with RDC windowing technique was proposed in this chapter as an enabler to completely remove the redundant CP from OTFS while breaking its Doppler limitations in massive MIMO systems. In the first stage of this chapter, the channel within each time slot of OTFS was approximated as constant. This way, TR-MRC can be performed with a single channel estimate at each time slot. The derivations of this chapter show that in the asymptotic regime, as the number of BS antennas tends to infinity, TR-MRC can effectively average out delay and Doppler spread of the channel. Without the delay spread, the interference terms that cause the ISI and IBI disappear as well, making CP unnecessary.

However, when the maximum Doppler frequency goes beyond OTFS limits, a residual Doppler effect within each OTFS time slot always remains. It was analytically shown that after combining, this effect tends to a simple scaling of the received symbols in the delay dimension as the number of BS antennas approaches infinity. The scaling coefficients are defined by the channel correlation, i.e., the samples of a Bessel function, which is dependent on the maximum Doppler shift of the channel. Based on this result, an RDC windowing technique was proposed to overcome the Doppler limitations of OTFS. The simulation results of this chapter showed that with the help of RDC windowing, OTFS can achieve performance close to that of LTI channels even for maximum Doppler shifts equivalent to speeds of 2000 km/h at a carrier frequency of 5.9 GHz.

Finally, this chapter also derived an alternative implementation choice for TR-MRC in the DD domain. In the delay-time domain, time reversal is performed with a convolution to focus the effect of the channel delay spread to a single point. Notably, the equivalent OTFS channel can be represented as a 2D circular convolution. Hence, this sparks the interesting idea of implementing time reversal with a 2D circular convolution to focus both the delay and Doppler simultaneously in the DD domain. However, complexity analysis between the implementation in delay-time and DD domains shows that the delay-time implementation requires less CMs. This is largely due to the high complexity of 2D circular convolutions.

Throughout this chapter, the channel estimates were assumed to be perfectly known, as if they were obtained using the EP scheme. However, this scheme deploys extensive zero guards around the pilot in the DD domain to prevent interference from delay and Doppler spreads, leading to large spectral efficiency loss. While many studies have explored reducing the zero guard for Doppler spread, an effective reduction for delay spread has yet to be demonstrated. Hence, in the next chapter, a novel pilot scheme is proposed to significantly reduce the zero guards along the delay dimension compared to the EP schemes.

Chapter 5

Split Pilot Channel estimation for OTFS

One of the main advantages of OFDM is its robustness to the channel delay spread. The equivalent OFDM channel becomes a simple scaling effect in static scenarios. Without the impact of delay spread, channel estimation can be performed without zero guards, reducing the required pilot overhead. However, this becomes impossible in LTV channels, as the effect of ICI corrupts the channel estimates. Therefore, an impulse pilot-based channel estimation must be placed in the delay domain, as it is seen in OTFS systems.

The prevalent channel estimation technique in the present literature is a high-power impulse pilot embedded in the DD domain together with data symbols [10]. To avoid interference from the pilot to data symbols and vice versa, the pilot is surrounded by a number of zero-guards that are larger than the channel delay and Doppler spread. This leads to a high pilot overhead, especially as the system bandwidth increases, and consequently, the discrete-time baseband channel becomes longer.

To reduce the pilot overhead, the authors in [10] also presented a reduced guard embedded impulse pilot for integer Doppler scenarios by reducing the zero guard across the Doppler dimension to twice the maximum Doppler index. However, this technique is not suitable for practical scenarios with fractional Doppler. Under such scenarios, the lack of a full zero guard across the Doppler dimension results in severe interference in the channel estimates due to the fractional Doppler. To solve this issue, the authors in [91–93] proposed iterative interference cancellation methods to refine the channel estimates. However, these methods are limited to scenarios where the channel is sparse. In [94, 95], authors addressed the channel estimation in OTFS systems using preamble pilot sequences. However, in high mobility scenarios, the channel estimate obtained using preamble-based pilots becomes outdated for the data transmission stage. The authors in [31–33] proposed a superimposed pilot structure to remove the pilot overhead completely. This technique superimposes a high-power pilot signal on all of the DD domain data. The main drawback of such a pilot structure is the huge computational complexity associated with the sophisticated estimation and detection algorithms. Furthermore, superimposed pilots are susceptible to channel variations within each time slot of OTFS, requiring a super-frame solely to obtain initial estimates of the channel delay and Doppler parameters. In [34], the authors developed a BEM-based [7] joint channel estimation and detection technique for impulse pilot with reduced guard across Doppler dimension. This method consists of deploying a reduced pilot overhead and iteratively refining the estimated channel and data using detected data as pseudo-pilots. However, using impulse pilots has the unique benefit of not requiring matrix inversion for channel estimation, a benefit that is lost in pseudo-pilots.

Multiple works in the literature have proposed to reduce the pilot overhead along the Doppler dimension. However, in practical scenarios, the channel length can be extremely large, and the delay guard becomes the main perpetrator of the large overhead. Furthermore, the channel length is directly proportional to the bandwidth of the system. Therefore, the required delay guard in wide band systems can become prohibitively large. Therefore, this chapter addresses the following research question:

> *Is it possible to reduce the pilot overhead along the delay dimension to a minimum, i.e., to the channel length, thereby almost halving the pilot overhead?*

When the delay guard is reduced, the received pilot region becomes filled with both pilot and data symbols. Given that the pilot power is focused on a single impulse, it is still possible to perform channel estimation by absorbing the data interference as noise. However, the data information within the received pilot region becomes severely affected by the pilot, incurring large performance loss. To solve this issue, a split pilot structure with two impulse pilots is proposed in this chapter. With the proposed structure, the two pilots can be used to effectively remove the pilot interference from the received signal, without losing the data information. This way, the pilot overhead is reduced by almost 50%. To remove the data interference from the channel estimates, an iterative joint channel estimation and detection technique is developed. The proposed technique uses the estimated data symbols to refine the channel estimates at each iteration. Through simulations, it is shown that the proposed technique significantly improves the BER performance of the split pilot structure. Furthermore, it has a high convergence speed, as two iterations are sufficient even in very high Doppler scenarios.

The rest of this chapter is laid out as follows. Section 5.1 provides a brief description of the system model considered in this chapter. Section 5.2 presents the issues with reducing the delay zero guard. It is shown that the information of the data transmitted instead of the delay zero guard is irretrievable, even with iterative methods. To solve this issue, a proposed pilot scheme is discussed in Section 5.3. In the proposed pilot scheme, two impulse pilots are deployed, one of them superimposed over data. This scheme allows to discern the received data information from the impulsive pilots. Furthermore, an additional step is proposed to iteratively reduce the data interference in the channel estimates. Section 5.4 provides numerical analysis to corroborate the claims of the previous sections. Finally, the chapter is concluded in 5.5

5.1 Single Antenna OTFS System

Consider an OTFS system in which each OTFS frame consists of M delay bins with the delay resolution $\Delta\tau = T_{\mathrm{s}}$ seconds and N Doppler bins with the Doppler resolution $\Delta\nu = \frac{1}{MNT_{\mathrm{s}}}$, where T_{s} hertz is the sampling period. At the OTFS transmitter, the information bits are mapped onto the Q-ary QAM constellation points where Q is the alphabet size. Then, they are embedded in the DD domain along with the pilot. Let the $M \times N$ matrices $\mathbf{D}$ and $\mathbf{P}$ represent the DD domain data symbols and the pilot signal, respectively, then the final DD domain transmitted signal $\mathbf{X}$ is obtained after multiplexing $\mathbf{D}$ and $\mathbf{P}$, i.e., $\mathbf{X} = \mathbf{D} + \mathbf{P}$. As the first stage of OTFS modulation, the DD frame is translated to the delay-time domain through an N-point IDFT matrix across the rows of $\mathbf{X}$ [23], similar to the previous chapter. The signal is then vectorized through a parallel-to-serial converter. To avoid interference between frames, a CP of length M_{cp} is appended to the start of each frame. M_{cp} is chosen to be larger than the channel length L. The vectorized form of the transmit signal, of length $M_{\mathrm{T}} = MN + M_{\mathrm{cp}}$ can be represented as $\mathbf{s} = \mathbf{A}_{\mathrm{cp}}(\mathbf{F}_N^{\mathrm{H}} \otimes \mathbf{I}_M)\mathbf{x}$, where $\mathbf{x} = \mathrm{vec}(\mathbf{X})$ and $\mathbf{A}_{\mathrm{cp}} = [\mathbf{G}_{\mathrm{cp}}^{\mathrm{T}}, \mathbf{I}_{MN}]^{\mathrm{T}}$ is the CP addition matrix and the $M_{\mathrm{cp}} \times MN$ matrix $\mathbf{G}_{\mathrm{cp}}$ includes the last M_{cp} rows of $\mathbf{I}_{MN}$.

The signal is transmitted through a LTV channel. Let the vector $\mathbf{r}$ represent the discrete-time baseband signal at the output of LTV channel. This signal can be represented as

$$\mathbf{r} = \mathbf{H}\mathbf{x} + \mathbf{w}, \tag{5.1}$$

where $\mathbf{w} \sim \mathcal{CN}(0, \sigma_w^2 \mathbf{I}_{M_\mathrm{T}})$ is the complex additive white Gaussian noise (AWGN) vector with variance σ_w^2, and the $M_\mathrm{T} \times M_\mathrm{T}$ matrix $\mathbf{H}$ is the LTV channel in the delay-time domain. The elements of $\mathbf{H}$ can be represented as

$$[\mathbf{H}]_{m,n} = \sum_{p=0}^{\Gamma-1} \alpha_p e^{j2\pi \upsilon_p n T_\mathrm{s}} \delta[m - n - \ell_p], \tag{5.2}$$

where Γ is the number of propagation paths and $\delta[\cdot]$ represents the Kronecker delta function. ℓ_p, υ_p, and α_p represent the delay tap, Doppler shift, and path gain associated with the p-th path. In practical wideband systems, the sampling rate is large enough to approximate the path delays to the nearest integer multiples of the sampling period [40]. Hence, only integer delays for ℓ_p are considered. This does not apply to the Doppler shifts, and υ_p includes both fractional and integer parts.

After removing CP and taking the delay-time domain received signal to the DD domain, the $MN \times 1$ received DD domain signal is obtained as

$$\mathbf{y} = \mathbf{H}_\mathrm{eff}\mathbf{x} + \mathbf{w}, \tag{5.3}$$

where $\mathbf{H}_\mathrm{eff} = (\mathbf{F}_N \otimes \mathbf{I}_M)\mathbf{R}_\mathrm{cp}\mathbf{H}\mathbf{A}_\mathrm{cp}(\mathbf{F}_N^\mathrm{H} \otimes \mathbf{I}_M)$ is the $MN \times MN$ effective channel matrix in the DD domain, $\mathbf{R}_\mathrm{cp} = [\mathbf{0}_{MN \times M_\mathrm{cp}}, \mathbf{I}_{MN}]$ is the CP removal matrix and $\mathbf{F}_N \otimes \mathbf{I}_M$ takes the delay-time domain signal to the DD domain. The $M \times N$ DD received signal matrix $\mathbf{Y}$ can be obtained by rearranging the vector $\mathbf{y}$.

5.2 Embedded Impulse Pilot Structure

The main challenges that the proposed technique in this chapter addresses are presented in this section. First, the widely used EP-based OTFS channel estimation is presented. This technique requires long zero-guards along delay and Doppler, leading to a large pilot overhead. To improve the spectral efficiency, this chapter proposes to reduce the delay guard above the pilot delay bin. With a reduced delay guard, the delay spread will cause the tail of the data above the pilot to fall inside the received pilot region. Derivations show that this tail can not be retrieved for data detection. Hence, a large portion of the data energy is lost leading to performance loss.

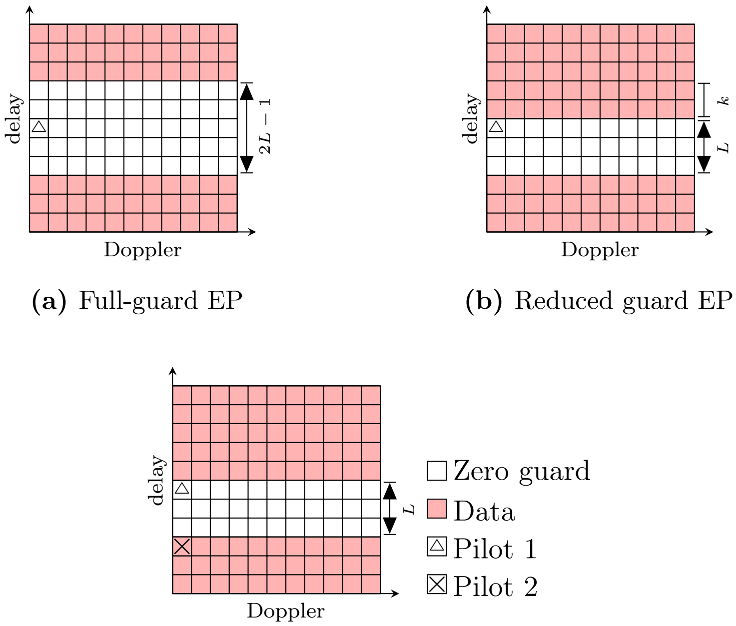

(a) Full-guard EP

(b) Reduced guard EP

(c) Proposed split pilot

Fig. 5.1 Different pilot schemes

5.2.1 Channel Estimation with Impulse Pilot

For an EP-based channel estimation, a single impulse is placed in the DD bin $(m_{\mathrm{p}}, n_{\mathrm{p}})$, surrounded by zero guards to avoid interference from data symbols, as shown in Fig. 5.1 (a). Let $\mathbf{Y}_{\mathrm{p}}$ represent the received pilot region in the DD domain, i.e., rows m_{p} to $m_{\mathrm{p}} + L - 1$ of $\mathbf{Y}$. Due to the delay spread, the received pilot region is affected by the transmitted symbols within the pilot region and $L-1$ delay bins above. The data, pilot and full transmitted symbols that affect the received pilot region are defined as $\mathbf{D}_{\mathrm{p}}$, $\mathbf{P}_{\mathrm{p}}$ and $\mathbf{X}_{\mathrm{p}}$, representing rows $m_{\mathrm{p}} - L + 1$ to $m_{\mathrm{p}} + L - 1$ of $\mathbf{D}$, $\mathbf{P}$ and $\mathbf{X}$, respectively. This structure is termed as full-guard since $\mathbf{X}_{\mathrm{p}}$ is fully allocated for pilot, i.e., $\mathbf{D}_{\mathrm{p}} = \mathbf{0}_{2L-1\times N}$.

The vectorized representation of the received pilot region is given as

$$\mathbf{y}_{\mathrm{p}} = \mathbf{H}_{\mathrm{eff,p}} \mathbf{x}_{\mathrm{p}} + \mathbf{w}_{\mathrm{p}}, \tag{5.8}$$

where $\mathbf{y}_{\mathrm{p}} = \mathrm{vec}(\mathbf{Y}_{\mathrm{p}})$, $\mathbf{x}_{\mathrm{p}} = \mathrm{vec}(\mathbf{X}_{\mathrm{p}})$, $\mathbf{w}_{\mathrm{p}}$ represents the AWGN noise in the received pilot region, and $\mathbf{H}_{\mathrm{eff,p}}$, given in (5.4), is the reduced effective channel matrix reflecting only the received pilot region. The $LN \times 1$ vector $\mathbf{h}$ contains the non-zero elements in the pilot column of $\mathbf{H}_{\mathrm{eff}}$. It is worth noting that $\mathbf{H}_{\mathrm{eff,p}}$ is a block circulant channel matrix formed by the Toeplitz submatrices $\mathbf{H}_n \in \mathbb{C}^{L\times(2L-1)}$. Hence, the property

$$\mathbf{H}_{\text{eff,p}} = \begin{bmatrix} \mathbf{H}_0 & \mathbf{H}_{N-1} & \cdots & \mathbf{H}_1 \\ \mathbf{H}_1 & \mathbf{H}_0 & \ddots & \mathbf{H}_2 \\ \vdots & \ddots & \ddots & \vdots \\ \mathbf{H}_{N-1} & \cdots & \cdots & \mathbf{H}_0 \end{bmatrix}, \tag{5.4}$$

where the matrices $\mathbf{H}_n$ are defined as follows

$$\mathbf{H}_n = \begin{bmatrix} \mathbf{h}[nL+L-1] & \cdots & \mathbf{h}[nL] & 0 & \cdots & 0 \\ 0 & \cdots & \mathbf{h}_n[nL+1] & \mathbf{h}_n[nL] & \cdots & 0 \\ \vdots & \ddots & \vdots & \ddots & \ddots & \vdots \\ 0 & \cdots & \mathbf{h}[nL+L-1] & \cdots & \cdots & \mathbf{h}_n[nL] \end{bmatrix}. \tag{5.5}$$

$$\mathbf{S}_{\text{bc}} = \begin{bmatrix} \mathbf{S}_0 & \mathbf{S}_{N-1} & \cdots & \mathbf{S}_1 \\ \mathbf{S}_1 & \mathbf{S}_0 & \ddots & \mathbf{S}_2 \\ \vdots & \ddots & \ddots & \vdots \\ \mathbf{S}_{N-1} & \cdots & \cdots & \mathbf{S}_0 \end{bmatrix}, \tag{5.6}$$

where the matrices $\mathbf{S}_n$ are defined as follows

$$\mathbf{S}_n = \begin{bmatrix} [X_{\text{p}}]_{L-1,n} & [X_{\text{p}}]_{L-2,n} & \cdots & [X_{\text{p}}]_{0,n} \\ [X_{\text{p}}]_{L,n} & [X_{\text{p}}]_{L-1,n} & \cdots & [X_{\text{p}}]_{1,n} \\ \vdots & \ddots & \ddots & \vdots \\ [X_{\text{p}}]_{2L-2,n} & \cdots & \cdots & [X_{\text{p}}]_{L-1,n} \end{bmatrix}. \tag{5.7}$$

$\mathbf{H}_{\text{eff,p}}\mathbf{x}_{\text{p}} = \mathbf{S}_{\text{bc}}\mathbf{h}$ can be obtained, where $\mathbf{S}_{\text{bc}}$ is the block circulant transmitted symbols matrix given in (5.6). Similar to $\mathbf{S}_{\text{bc}}$, $\mathbf{S}_{\text{d}}$ can be derived with only the data symbols in $\mathbf{D}_{\text{p}}$ and $\mathbf{S}_{\text{p}}$ with only the pilot symbols in $\mathbf{P}_{\text{p}}$, i.e., $\mathbf{S}_{\text{bc}} = \mathbf{S}_{\text{d}} + \mathbf{S}_{\text{p}}$. It is worth noting that in the full-guard structure, $\mathbf{S}_{\text{d}} = \mathbf{0}_{LN\times LN}$, and when $n_{\text{p}} = 0$, $\mathbf{S}_{\text{p}} = \sqrt{\gamma_{\text{p}}}\mathbf{I}_{LN}$. Hence, the block circulant transmitted symbols matrix $\mathbf{S}_{\text{bc}}$ becomes

$$\mathbf{S}_{\text{bc}} = \mathbf{S}_{\text{d}} + \mathbf{S}_{\text{p}} = \sqrt{\gamma_{\text{p}}}\mathbf{I}_{LN}. \tag{5.9}$$

Therefore, the channel estimates are obtained as

$$\widehat{\mathbf{h}} = \frac{1}{\sqrt{\gamma_{\text{p}}}}\mathbf{y}_{\text{p}} = \frac{1}{\sqrt{\gamma_{\text{p}}}}(\mathbf{S}_{\text{bc}}\mathbf{h} + \mathbf{w}_{\text{p}}) = \mathbf{h} + \frac{1}{\sqrt{\gamma_{\text{p}}}}\mathbf{w}_{\text{p}}. \tag{5.10}$$

The channel estimates $\widehat{\mathbf{h}}$ only provide a single column of $\mathbf{H}_{\text{eff}}$. That is, it considers locally time-invariant channels over each time slot. However, in high Doppler environments, the channel variations within each time slot become significant. These variations can not be captured with a single impulse pilot. Hence, to improve the channel estimates, the channel estimates $\widehat{\mathbf{h}}$ are transformed to the delay-time domain, where the estimates are interpolated with spline interpolation to find an estimate of the full channel matrix $\widehat{\mathbf{H}}_{\text{eff}}$ [73]. Finally, the data symbols are detected using this channel estimate.

The above channel estimates can only be achieved when $\mathbf{X}_{\text{p}}$ contains only pilot symbols, i.e., $(2L-1)N$ slots are allocated for the pilot. To improve the spectral efficiency, the effects of reducing the delay guard of the system are analyzed in the following subsection.

5.2.2 Channel Estimation Using Impulse Pilot with Reduced Guard

Aiming to reduce the pilot overhead, the number of zero guard bins along the delay dimension is reduced. In this new structure, only $2L-1-k$ delay bins are assigned for pilot overhead, where k represents the number of delay bins assigned for data instead of zero guards, e.g., $k = L-1$ shown in Fig. 5.1 (b). In this scenario, the received pilot region $\mathbf{Y}_{\text{p}}$ remains in the same location, with the distinction that $\mathbf{X}_{\text{p}}$ contains both data symbols and the pilot signal. The derivations are divided into two stages. The first stage consists of obtaining an initial channel and data estimates. In the second stage, the channel estimates are refined iteratively, using the detected data from previous iterations to remove the data interference from the channel estimates.

Stage 1: With a reduced delay guard, the delay spread will cause the tail of the data symbols above the pilot to spill into the received pilot region. Hence, $\mathbf{S}_{\text{d}}$ now contains the effects of data interference. With the pilot matrix $\mathbf{S}_{\text{p}}$ unchanged, the received pilot region can be shown as

$$\mathbf{y}_{\text{p}} = (\mathbf{S}_{\text{p}} + \mathbf{S}_{\text{d}})\mathbf{h} + \mathbf{w}_{\text{p}} = (\sqrt{\gamma_{\text{p}}}\mathbf{I}_{LN} + \mathbf{S}_{\text{d}})\mathbf{h} + \mathbf{w}_{\text{p}}. \tag{5.11}$$

Hence, by absorbing the interference from data into noise, the estimated channel is given as

$$\widehat{\mathbf{h}} = \frac{1}{\sqrt{\gamma_{\text{p}}}}\mathbf{y}_{\text{p}} = \mathbf{h} + \frac{1}{\sqrt{\gamma_{\text{p}}}}(\mathbf{S}_{\text{d}}\mathbf{h} + \mathbf{w}_{\text{p}}). \tag{5.12}$$

As it is evident from (5.12), the channel estimate is imperfect. When using linear-based detectors, the imperfect channel leads to inaccuracies in data detection. This error is severely enhanced by the high pilot power, affecting the detected data. Hence, the pilot signal must be removed from the received signal before data detection.

However, removing the pilot with (5.12) also removes the tail of the data symbols above the pilot, i.e., $\mathbf{S}_\mathrm{d}$. Therefore, a significant portion of the data energy is lost, leading to a significant performance loss. Hence, in the following stage, the channel estimates are refined iteratively, where the data interference is removed at each iteration. This also allows a more accurate removal of the pilot effect from the received signal.

Stage 2: To refine the channel estimates, the data interference is removed using the estimated data symbols from the previous iterations. Hence, the channel estimate at iteration n is obtained as

$$\begin{aligned}\widehat{\mathbf{h}}^{(n)} =& \frac{1}{\sqrt{\gamma_\mathrm{p}}}(\mathbf{y}_\mathrm{p} - \widehat{\mathbf{S}}_\mathrm{d}^{(n-1)}\widehat{\mathbf{h}}^{(n-1)}) \\ =& \mathbf{h} + \frac{1}{\sqrt{\gamma_\mathrm{p}}}\left((\mathbf{S}_\mathrm{d} - \widehat{\mathbf{S}}_\mathrm{d}^{(n-1)})\mathbf{h} + \mathbf{w}_\mathrm{p}\right) \\ &- \frac{1}{\gamma_\mathrm{p}}\widehat{\mathbf{S}}_\mathrm{d}^{(n-1)}(\mathbf{S}_\mathrm{d}\mathbf{h} + \mathbf{w}_\mathrm{p}).\end{aligned} \tag{5.13}$$

To simplify the above expression, the term $-\frac{1}{\gamma_\mathrm{p}}\widehat{\mathbf{S}}_\mathrm{d}^{(n-1)}(\mathbf{S}_\mathrm{d}\mathbf{h}+\mathbf{w}_\mathrm{p})$ is absorbed into noise as generally the pilot power is sufficiently large to make this term negligible. From (5.13), it can be concluded that the channel estimates are refined if $\widehat{\mathbf{S}}_\mathrm{d}^{(n)}$ converges to $\mathbf{S}_\mathrm{d}$.

After the channel estimate is refined, the pilot effect is removed from the received signal using (5.13)

$$\mathbf{y}_\mathrm{p} - \mathbf{S}_\mathrm{p}\widehat{\mathbf{h}}^{(n)} = \widehat{\mathbf{S}}_\mathrm{d}^{(n-1)}\mathbf{h}. \tag{5.14}$$

This indicates that the original data information within the received pilot region is replaced with the estimated data in the previous iterations. Hence, the iterative method also fails to preserve the tail of the data $\mathbf{S}_\mathrm{d}$.

The above derivations lead to the conclusion that the main issue of reducing the delay guard comes from losing data energy within the received pilot region. To solve this issue, a new pilot structure is proposed in the next section. The proposed structure reduces the delay guard and enables the removal of the pilot effect without data energy loss.

5.3 Proposed Split Pilot Structure and Channel Estimation Technique

It was shown in the previous section that reducing the pilot delay guard in EP schemes causes data loss in the received pilot region. More specifically, this issue occurs when the pilot effect is removed from the received signal before data detection. Since data interference is present in the channel estimate, removing the pilot effect also removes a portion of the data energy, resulting in performance loss. This issue persists even when the data interference is iteratively removed from the channel estimate. To solve this issue, a new pilot structure is proposed, which is capable of removing the pilot effect without loss of data information. To refine the channel estimates, an iterative joint channel estimation and detection technique, tailored to the pilot structure, is introduced. Ultimately, the proposed structure significantly reduces the pilot overhead compared to EP-based structures.

In the proposed pilot structure, the impulse pilot is split into two impulses of equal power $\frac{\gamma_{\mathrm{p}}}{2}$. The position of pilot 1 is kept at DD bin $(m_{\mathrm{p}}, n_{\mathrm{p}})$ and pilot 2 is placed at DD bin $(m_{\mathrm{p}}+L, n_{\mathrm{p}})$. The two impulses are placed L delay taps apart, hence the pilots do not interfere with each other. To minimize the pilot overhead, the second pilot is superimposed over data, and both pilots share a reduced zero guard region, as shown in Fig. 5.1 (c). The proposed method is divided into two stages. In the first stage, the channel is estimated by averaging the response from each pilot, while absorbing the data interference into noise. To remove the pilot effect from the received signal, the effect of one impulse is canceled out using the response of the second impulse. Stage two consists of the proposed joint channel estimation and detection technique. In this stage, the channel estimate is refined by iteratively removing the data interference in the received pilot region.

Stage 1: Since there are now two impulsive pilots, the effect of each impulse pilot is analyzed separately. Similar to (5.8), the regions of the received impulse pilot 1 and 2 are defined as $\mathbf{Y}_{\mathrm{p}_1}$ and $\mathbf{Y}_{\mathrm{p}_2}$, respectively. Each region extends from the delay bin of the impulse pilot to the $L-1$ delay bins below. The pilot regions are also affected by data interference $\mathbf{S}_{\mathrm{d}_1}$ and $\mathbf{S}_{\mathrm{d}_2}$, containing data symbols within $L-1$ delay bins above and after the respective pilots' location. Since minimal variation exists in the channel within L delay taps, the channel variations within the two pilots are disregarded in the derivations. Hence, at each pilot region, the channel estimates are obtained as

$$\begin{aligned}\widehat{\mathbf{h}}_1 &= \frac{\sqrt{2}}{\sqrt{\gamma_\mathrm{p}}}\mathbf{y}_{\mathrm{p}_1} = \mathbf{h} + \frac{\sqrt{2}}{\sqrt{\gamma_\mathrm{p}}}(\mathbf{S}_{\mathrm{d}_1}\mathbf{h} + \mathbf{w}_{\mathrm{p}_1}),\\ \widehat{\mathbf{h}}_2 &= \frac{\sqrt{2}}{\sqrt{\gamma_\mathrm{p}}}\mathbf{y}_{\mathrm{p}_2} = \mathbf{h} + \frac{\sqrt{2}}{\sqrt{\gamma_\mathrm{p}}}(\mathbf{S}_{\mathrm{d}_2}\mathbf{h} + \mathbf{w}_{\mathrm{p}_2}),\end{aligned} \tag{5.15}$$

where $\mathbf{w}_{\mathrm{p}_1}$ and $\mathbf{w}_{\mathrm{p}_2}$ represent the AWGN noise from received pilot 1 and 2, respectively. To reduce the noise and interference, the final channel estimate $\widehat{\mathbf{h}}$ is obtained after averaging $\widehat{\mathbf{h}}_1$ and $\widehat{\mathbf{h}}_2$.

As explained in the previous section, the pilot effect has to be removed from the received signal before data detection. Therefore, $\widehat{\mathbf{h}}_1$ is used to remove the effect of the second pilot

$$\mathbf{y}_{\mathrm{p}_2} - \mathbf{y}_{\mathrm{p}_1} = (\mathbf{S}_{\mathrm{d}_2} - \mathbf{S}_{\mathrm{d}_1})\mathbf{h} + \mathbf{w}_{\mathrm{p}_2} - \mathbf{w}_{\mathrm{p}_1}. \tag{5.16}$$

In this expression, the pilot is completely removed, and the data information from both pilot regions is preserved. Furthermore, due to the shared delay guard between the two impulse pilots, there is no overlap between the non-zero elements of $\mathbf{S}_{\mathrm{d}_1}$ and $\mathbf{S}_{\mathrm{d}_2}$. This ensures that the data symbols in $\mathbf{S}_{\mathrm{d}_1}$ and $\mathbf{S}_{\mathrm{d}_2}$ are discernible in the detector. Finally, the negative sign of the data vector $\mathbf{S}_{\mathrm{d}_1}$ in (5.16) can be absorbed in the channel elements when reconstructing $\widehat{\mathbf{H}}_{\mathrm{eff}}$. The received signal and channel estimate are then fed to the detector to obtain an initial data estimate $\widehat{\mathbf{D}}^{(0)}$.

In reality, the channel ages within the two impulse pilots. The channel estimated from the first pilot is slightly different from the channel estimated from the second pilot. This introduces interference in (5.16). To tackle this issue, the pilot effect is removed from the received signal after interpolating the channel estimates at each iteration of the next stage.

Stage 2: With an initial data estimation provided from stage 1, the data interference can be iteratively removed in (5.15) to refine the channel estimates. At each iteration n, the detected data from the previous iteration $\widehat{\mathbf{D}}^{(n-1)}$ are used to generate the matrices $\widehat{\mathbf{S}}_{\mathrm{d}_1}^{(n-1)}$ and $\widehat{\mathbf{S}}_{\mathrm{d}_2}^{(n-1)}$. These data matrices are then used to remove the data interference from each pilot region before performing channel estimation. This way, the channel estimate from each impulse pilot at iteration n is obtained as

$$\begin{aligned}\widehat{\mathbf{h}}_1^{(n)} &= \mathbf{h} + \frac{\sqrt{2}}{\sqrt{\gamma_{\mathrm{p}}}}\Big((\mathbf{S}_{\mathrm{d}_1} - \widehat{\mathbf{S}}_{\mathrm{d}_1}^{(n-1)})\mathbf{h} + \mathbf{w}_{\mathrm{p}_1}\Big),\\ \widehat{\mathbf{h}}_2^{(n)} &= \mathbf{h} + \frac{\sqrt{2}}{\sqrt{\gamma_{\mathrm{p}}}}\Big((\mathbf{S}_{\mathrm{d}_2} - \widehat{\mathbf{S}}_{\mathrm{d}_2}^{(n-1)})\mathbf{h} + \mathbf{w}_{\mathrm{p}_2}\Big).\end{aligned} \tag{5.17}$$

Once again, the above channel estimates are averaged to reduce the effect of noise.

In *Stage 1*, it was considered the approximation of a time-invariant channel within each time slot. However, in high Doppler scenarios, the channel ages between the two pilots causing an interference in (5.16). Although the channel only ages slightly within L samples, this variation is greatly enhanced by the pilot power, causing performance loss in the system. Additionally, it was shown in (5.14) that removing the pilot effect with its own estimate leads to data energy loss. Therefore, to avoid both issues, the channel estimates in (5.17) are interpolated first and $\widehat{\mathbf{h}}_2^{(n)}$ is used to remove pilot 1 from the received signal and vice versa. The received signal after pilot removal becomes

$$\begin{aligned}\mathbf{y}_{\mathrm{p}_1} - \mathbf{S}_{\mathrm{p}}\widehat{\mathbf{h}}_2^{(n)} &= (\mathbf{S}_{\mathrm{d}_1} - \mathbf{S}_{\mathrm{d}_2} + \widehat{\mathbf{S}}_{\mathrm{d}_2}^{(n-1)})\mathbf{h} + \mathbf{w}_{\mathrm{p}_1} - \mathbf{w}_{\mathrm{p}_2},\\ \mathbf{y}_{\mathrm{p}_2} - \mathbf{S}_{\mathrm{p}}\widehat{\mathbf{h}}_1^{(n)} &= (\mathbf{S}_{\mathrm{d}_2} - \mathbf{S}_{\mathrm{d}_1} + \widehat{\mathbf{S}}_{\mathrm{d}_1}^{(n-1)})\mathbf{h} + \mathbf{w}_{\mathrm{p}_2} - \mathbf{w}_{\mathrm{p}_1}.\end{aligned} \tag{5.18}$$

The received signal and channel estimate are then fed to the detector to obtain the data estimates $\widehat{\mathbf{D}}^{(n)}$. This process is repeated until one of the following stopping criteria is met:

- The data symbols after hard decision in $\mathbf{S}_{\mathrm{d}_1}^{(n)}$ and $\mathbf{S}_{\mathrm{d}_2}^{(n)}$ does not change from the previous iteration, i.e., $\mathbf{S}_{\mathrm{d}_1}^{(n)} = \mathbf{S}_{\mathrm{d}_1}^{(n-1)}$ and $\mathbf{S}_{\mathrm{d}_2}^{(n)} = \mathbf{S}_{\mathrm{d}_2}^{(n-1)}$.
- The maximum number of iterations $n_{\max}$ is reached.

Comparing (5.18) with (5.14), it can be observed that the proposed method effectively retains the data information in the pilot region. Furthermore, the data interference reduces at each iteration, as $\widehat{\mathbf{S}}_{\mathrm{d}_1}^{(n)}$ and $\widehat{\mathbf{S}}_{\mathrm{d}_2}^{(n)}$ converges to $\mathbf{S}_{\mathrm{d}_1}$ and $\mathbf{S}_{\mathrm{d}_2}$, respectively. The proposed technique is summarized in Algorithm 2.

5.4 Simulation Results

In this section, the efficacy of the proposed method is confirmed by comparing its performance with that of full and reduced guard schemes. An OTFS system with

Algorithm 2 Proposed split pilot technique.

Obtain the initial estimate $\widehat{\mathbf{h}} = \frac{\widehat{\mathbf{h}}_1+\widehat{\mathbf{h}}_2}{2}$ using (5.15).
Interpolate $\widehat{\mathbf{h}}$ to generate $\widehat{\mathbf{H}}_{\text{eff}}$.
Remove the pilot from $\mathbf{Y}$ using (5.16).
Feed $\widehat{\mathbf{H}}_{\text{eff}}$ and $\mathbf{Y}$ to the detector to obtain $\widehat{\mathbf{D}}^{(0)}$.
for $n = 1$ to $n_{\max}$ **do**
    Refine channel estimates using (5.17).
    Interpolate $\widehat{\mathbf{h}} = \frac{\widehat{\mathbf{h}}_1^{(n)}+\widehat{\mathbf{h}}_2^{(n)}}{2}$ to generate $\widehat{\mathbf{H}}_{\text{eff}}^{(n)}$.
    Remove Pilot 1 from $\mathbf{Y}$ using interpolated $\widehat{\mathbf{h}}_2^{(n)}$.
    Remove Pilot 2 from $\mathbf{Y}$ using interpolated $\widehat{\mathbf{h}}_1^{(n)}$.
    Feed $\widehat{\mathbf{H}}_{\text{eff}}^{(n)}$ and $\mathbf{Y}$ to the detector to obtain $\widehat{\mathbf{D}}^{(n)}$.
    Stop if the stopping criteria is met.
end for

$M = 128$ delay and $N = 32$ Doppler bins is considered. In the simulation setup, a carrier frequency $f_{\text{c}} = 5.9$ GHz, subcarrier spacing $\Delta f = 15$ kHz, and 4-QAM modulation is deployed. The channel is modeled using the EVA channel model, [44], and the Doppler shift is generated using Jake's model for the relative speed of 500 km/h. The maximum delay spread of the channel is 2510 ns and the sampling period of the system is $T_{\text{s}} = 520.3$ ns, leading to a channel length $L = 5$. The full-guard scheme deploys 288 DD bins as pilot overhead, while the proposed method deploys only 160 DD bins for the pilot. Similar to [10], the total pilot power is set at $\gamma_{\text{p}} = 40$ dB for all pilot schemes. Pilot 1 is placed at delay bin $m_{\text{p}} = \frac{M}{2}$ and Doppler bin $n_{\text{p}} = 0$. Unless otherwise stated, four iterations are considered for the EP with reduced guard structure. The least squares minimum residual-based technique with interference cancellation [35] is used for data detection.

In Fig. 5.2, the BER performance of the proposed scheme is compared with the full and reduced guard schemes. The results show that the reduced guard scheme has a high BER floor even after refining the channel estimates for four iterations. This result is in line with the analysis in (5.14), where it is shown that the iterative process is incapable of improving the data detection performance. In contrast, the proposed method can achieve similar performances after two iterations of refining the channel. The observed difference in performance is caused by the channel aging between the two pilots and noise enhancement within the pilot region, i.e., $\mathbf{w}_{\text{p}_2} - \mathbf{w}_{\text{p}_1}$ in (5.16).

The proposed technique is also evaluated in terms of normalized mean square error (NMSE) of channel estimation, defined as $\frac{||\mathbf{H}_{\text{eff}}-\widehat{\mathbf{H}}_{\text{eff}}^{(n)}||_{\text{F}}^2}{||\widehat{\mathbf{H}}_{\text{eff}}^{(n)}||_{\text{F}}^2}$. Fig. 5.3 shows that after convergence, the proposed technique reaches the NMSE of 10^{-3} with a 2 dB loss compared to EP with full-guard, whereas the reduced guard has over 4 dB loss.

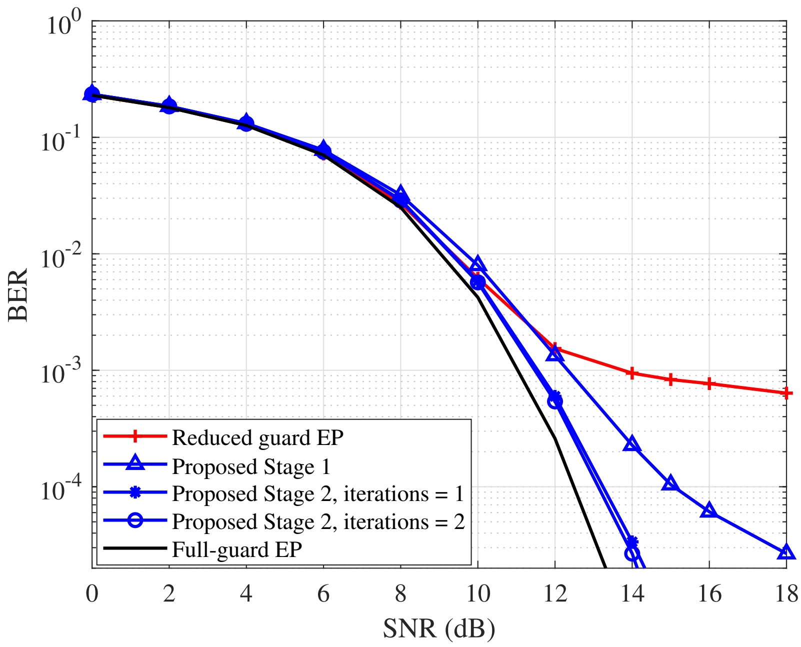

Fig. 5.2 BER performance of the proposed scheme compared with full and reduced guard schemes.

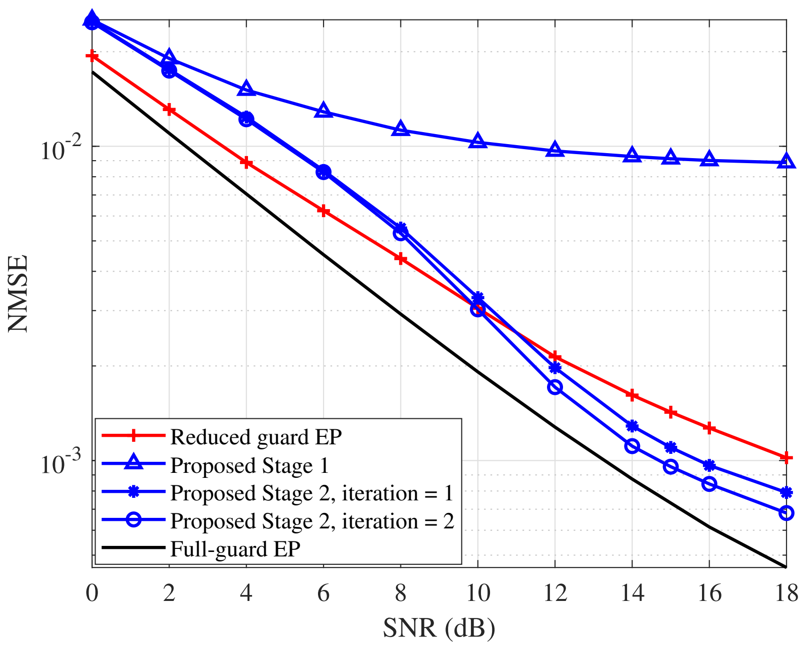

Fig. 5.3 NMSE performance of the proposed scheme compared with full and reduced guard schemes.

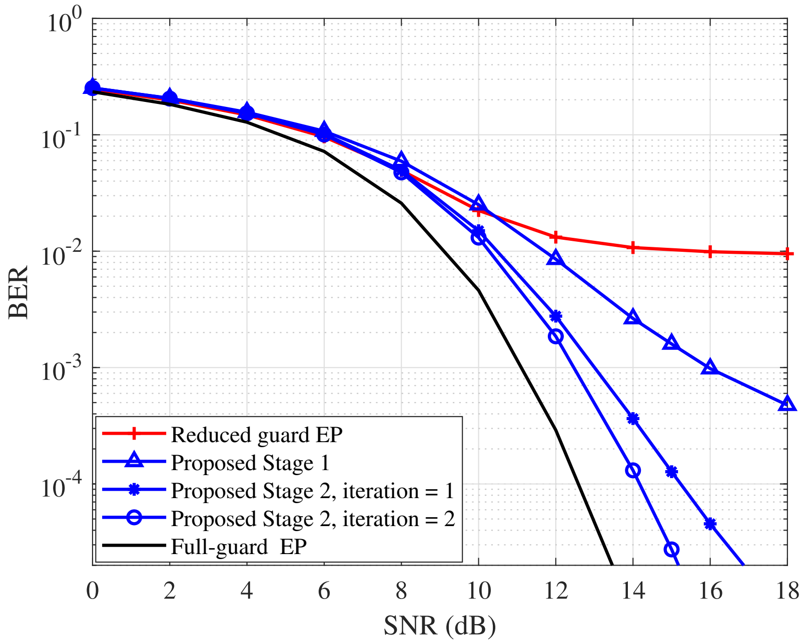

Fig. 5.4 BER performance with increased channel length.

Additionally, it can be observed that even though the reduced guard EP attains acceptable NMSE at high SNRs, there is a BER floor (refer to Fig. 5.2) due to the data energy loss as shown in (5.14).

The proposed method is also validated in scenarios with large channel lengths. In Fig. 5.4, the sampling period of the OTFS system is shortened to $T_s = 133.33$ ns. Consequently, the channel length increases to $L = 19$. In this system, the full-guard scheme deploys a total of 1184 DD bins for pilot overhead, while the proposed scheme requires only 608 DD bins. The performance loss of the proposed method is more pronounced since the noise enhancement in the pilot region spans over a larger portion of the transmission frame.

Finally, Fig. 5.5 investigates the convergence speed of the proposed scheme in terms of BER and NMSE performance at SNR of 14 dB. It is shown that within two iterations, the proposed method converges to significantly lower NMSE and BER values than the reduced guard EP.

5.5 Conclusion

In the effort of reducing the pilot overhead in high mobility scenarios, this chapter studies the possibility of reducing the delay guard of channel estimation schemes in OTFS. First, this chapter proves that simply reducing the delay guards in widely used

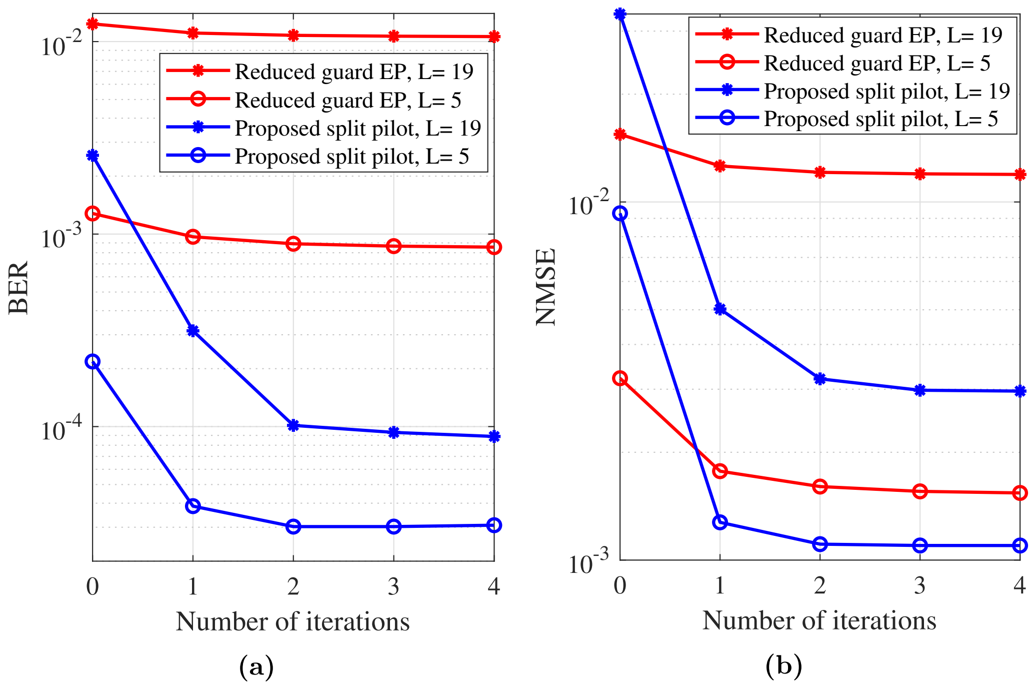

Fig. 5.5 Convergence speed in terms of BER (a) and NMSE (b) performance at 14 dB.

EP schemes is ineffective. The analysis show that with a single pilot, it is impossible to distinguish the data information that the delay spreads over the transmitted pilot. Without this data information, the detection of the data transmitted in the delay bins adjacent to the pilot is jeopardized. Therefore, high error floors can be seen in the simulated BER performance of the reduced guard EP schemes.

Hence, to solve this issue, a split pilot scheme is proposed. With two pilots, the pilot interference over data information can be effectively removed. This is while both pilots can efficiently share the reduced delay zero guard region. In the first stage of the proposed channel estimation method, the data interference over the channel estimates is absorbed into noise. Afterwards, the second pilot is used to fully remove the effect of the first pilot, without any loss of data information. With this step, the simulation results show that BER performance improves significantly compared to the reduced guard EP scheme.

However, the NMSE performance of the channel estimates reveal that the split pilots suffers greatly from data interference. Therefore, a joint channel estimation and equalization technique is proposed for the second stage of the split pilot scheme. In this method, the channel estimates are refined iteratively using the detected data at each iteration. Simulation results show that, with as few as 2 iterations, the channel estimates from the proposed method can surpass the reduced guard EP scheme in terms of NMSE performance. Consequently, the proposed scheme achieves BER performances close to that of full guard EP schemes.

Finally, this chapter also shows through simulations that the proposed split pilot scheme remains effective under scenarios with longer channel lengths. Hence, proving that the proposed method effectively reduce the delay guard by 50% compared to EP schemes, independent of the channel length. Furthermore, the iterative joint channel estimation and equalization stage has a high convergence speed, requiring only two iterations even in high mobility scenarios.

Chapter 6

Conclusions and Future Work

Time and frequency selectivity of the channel impose large signaling overheads to both contemporary and future networks. Hence, reducing the large signaling overhead is a necessary step towards achieving contemporary networks' high data rate requirements. Furthermore, in the move towards 6G, a large number of new applications involving high mobility, such as drone communications, autonomous vehicles, and bullet trains, emerged. Under high mobility scenarios, the channel becomes time-varying, which demands faster channel tracking. Consequently, the signaling overhead becomes a greater issue in such scenarios. Therefore, the main focus of this thesis was to find innovative approaches to deal with the delay and Doppler spreads of the channel. This thesis proposed novel techniques that significantly reduce the signaling overhead without affecting the functionality of the system.

6.1 Summary of Contributions and Conclusions

This section briefly outlines the key contributions presented in this thesis. More specifically, this section highlights the key findings of Chapters 3, 4, and 5, and how they address the research questions raised in Chapter 1.

6.1.1 Reserch Question 1

- **Is it possible to reduce the selectivity of the channel into its known and constant correlation function to minimize the channel estimation overhead?**

In contemporary networks, OFDM-based massive MIMO systems require a long pilot sequence to estimate the CFR at each subcarrier which degrades the spectral efficiency of the system. Hence, a solution in the form of a novel joint channel estimation and equalization technique was proposed in Chapter 3 that requires only a single pilot subcarrier. This chapter first showed that the channel hardening effect results in the channel correlation. Recognizing that the coherence bandwidth defines the frequency band in which the correlation is high, the transmitted data from a band of subcarriers within the coherence band of the channel were estimated using the CFR of a single subcarrier. Thereafter, the CFR of each subcarrier within the coherence band of the channel was updated using the estimated data as virtual pilots. Each new CFR estimate was then used to estimate a new band of subcarriers. This process was repeated in a sliding manner to detect the transmitted data at all subcarriers in the OFDM frame. This way, the channel estimation overhead was reduced to only a single pilot subcarrier, independent of the channel length.

The derivations and insights from the proposed joint channel estimation and equalization method also led to an interesting finding in the form of frequency diversity. Frequency diversity was achieved when multiple CFRs within the coherence bandwidth were combined to average out the channel estimation noise. However, similar to spatial diversity, combining only improves performance when the noise terms are uncorrelated. For this reason, it was shown in Chapter 3 that only the proposed method benefits from frequency diversity because virtual pilots are used for channel estimation. Meanwhile, the conventional LS-based channel estimation technique does not benefit from the diversity as the CFR estimation noise from adjacent subcarriers is highly correlated. Consequently, the proposed method achieved higher SINR and BER performances when compared with the conventional methods, even when using only one single pilot subcarrier.

Concluding Remarks

The proposed method in Chapter 3 can effectively deal with frequency selectivity with only a single pilot subcarrier. However, in the process of extending the findings of Chapter 3 to deal with time selectivity, the major drawbacks of OFDM in LTV channels posed a significant challenge. More specifically, the ICI caused by the Doppler shifts severely degrades the channel estimation performance using impulse pilots without a guard. Furthermore, as shown in Chapters 2 and 3, multiuser channel estimation relies on the constant channel response along different OFDM symbols, and the orthogonality of the pilot sequence, e.g., the ZC sequence used in this thesis. In the presence of high Doppler shifts, the pilot sequence orthogonality is also lost and multiuser channel estimates become riddled with MUI. Hence, the motivation to explore new waveforms, such as OTFS, arises.

OTFS modulation is a fresh and revolutionary approach to deal with doubly selective channels. Within only a few years of existence, it has already gained its spot as a candidate waveform for the next-generation wireless systems. However, like any emerging technique, OTFS literature still has much to be explored. In the context of this thesis, since OTFS places the data in the DD domain, the delay and Doppler spreads demanded long guard sequences within the transmitted signal. This issue motivated the following research questions that were addressed in this thesis.

6.1.2 Reserch Question 2

- **Can TR-MRC average out doubly spread channel effects and break the Doppler limitations of OTFS?**

Research questions 2 and 3 are motivated by the need to minimize the signaling overhead in high mobility scenarios. These scenarios can be found in a multitude of new applications that are emerging in next-generation networks and applications, e.g., drone communications, autonomous vehicles, and bullet trains. Hence, innovative solutions that can efficiently deal with the delay and Doppler spreads of the channel are essential. Therefore, TR-MRC with RDC windowing was proposed for OTFS-based massive MIMO systems in Chapter 4. The study in this chapter showed that using TR-MRC effectively averaged out the delay and Doppler spreads of the channel while eliminating the need for any guard in between delay blocks during transmission, i.e., CPs within and in between OTFS blocks. Apart from the spectral efficiency gains from removing CP, it was an important step required when designing the OTFS system parameters. Numerous works in the literature consider the approximation of a constant channel along each OTFS delay block [11, 18]. For this approximation to be acceptable in high Doppler channels, the duration of each delay block must be reduced. However, this reduction would incur severe spectral performance losses if CPs were to be appended at the start of each delay block.

Noticeably, reducing the duration of an OTFS delay block is limited by any kind of signaling overhead, such as pilot sequences. Hence, the RDC windowing was proposed in Chapter 4. This method corrects the channel variations within each delay block of the OTFS frame. This significantly alleviates the need to reduce the duration of each delay block as it increases the limits of OTFS in terms of maximum Doppler shifts, i.e., maximum Doppler shift corresponding to a relative speed between transmitter and receiver of 2000 kmph, at the carrier frequency of 5.9 GHz.

Concluding Remarks

The proposed TR-MRC with RDC windowing technique is a powerful technique that deals with the delay and Doppler spreads of the channel. However, it is worth noting that combining techniques requires accurate CSI. In other words, the delay and Doppler shifts are only averaged out after accurate channel estimation, and guards were still necessary for the pilot overhead. Hence, the large guard sequences required in the channel estimation stage degraded significantly the spectral efficiency of OTFS. In Chapter 4, the derivations considered the widely used EP-aided channel estimation technique [10] in the OTFS literature. This structure deploys an impulsive pilot in the DD domain surrounded by zero guards to avoid data interference caused by delay and Doppler spreads. In other words, twice the delay spread length is allocated as zero guards in the delay dimension, this is while all Doppler bins are allocated for zero guards. Ultimately, a significant portion of the OTFS transmission system was designated for pilot overhead. This issue motivated the next research question that was addressed in Chapter 5.

6.1.3 Reserch Question 3

- **Is it possible to reduce the pilot overhead along the delay dimension to a minimum, i.e., to the channel length, thereby almost halving the pilot overhead?**

Under static channel scenarios, frequency-domain channel estimation techniques require pilot sequence lengths equal to the channel length. However, when the channel is estimated in the delay domain, e.g., in the EP-aided channel estimation technique, long guards are deployed to avoid interference caused by the delay spread. Consequently, delay-domain channel estimation techniques require almost double the pilot overhead compared to frequency-domain methods. With this in mind, a split pilot scheme that requires the minimum overhead length in the delay dimension was proposed in Chapter 5. This pilot scheme used two impulsive pilots to effectively remove the interference caused by the transmitted pilots over data in the absence of a delay guard. Furthermore, an iterative channel estimation and equalization technique was also proposed in this chapter. This technique used the estimated data from each iteration to remove the interference caused by the transmitted data over the pilots. The main benefit of this technique is that it significantly improves the channel estimation performance in terms of NMSE, and consequently the BER performance of the system. Furthermore, the proposed technique showed a fast convergence speed since as few as two iterations were required. Altogether, the proposed split pilot scheme achieved BER performance close to that of EP schemes while using almost half the pilot overhead.

Concluding Remarks

The split pilot scheme is an ingenious take on impulsive pilot channel estimation that can efficiently circumvent the effects of the channel delay spread. Ultimately, the proposed method can reduce the required delay guard by half, when compared to the widely used EP scheme. This is an important improvement, especially in scenarios with large delay spread.

This thesis proposed a joint channel estimation and equalization technique that significantly reduced the pilot overhead for contemporary systems in Chapter 3. Moving to next-generation networks under high mobility scenarios, Chapter 4 proposed the TR-MRC with RDC windowing method to completely remove the CP of OTFS systems. Furthermore, a novel split pilot scheme was proposed in Chapter 5 that effectively reduced by almost half the required pilot overhead. All these methods contributed to a considerable reduction in the signaling overhead of both contemporary and next-generation wireless systems. However, there are alternative approaches, aside from reducing signaling overhead, that can further enhance the spectral efficiency of wireless systems. The next section discusses some of the research directions in this regard.

6.2 Future Work and Final Remarks

The contributions of this thesis ignite multiple new research lines and opportunities for novel approaches aimed at improving spectral efficiency and reducing the latency of future 6G networks and the underlying services. Some of these noteworthy topics are outlined as follows:

- Implementation and analysis of the proposed methods in test beds are an important research direction for proof of concept of the study presented in this thesis. Furthermore, the proposed methods can be evaluated in multiple different real-world scenarios, where the delay and Doppler spreads of the channel can vary greatly.

- Contrary to OFDM, OTFS literature is still in its early stages of development. Therefore, many research topics surrounding OTFS remain to be addressed. One of these topics is related to OTFS synchronization. Most existing synchronization studies require a preamble to estimate the carrier frequency and timing offsets [96]. In order to reduce the transmission overhead, novel synchronization techniques can be researched using the pilot structures proposed in this thesis.

- Another interesting research direction involving OTFS is on approaches that can reduce the effect of Doppler spread. Specifically, there are multiple waveforms that use different pulse-shaping designs that can reduce the effect of fractional Doppler, e.g., filter bank multicarrier-based OTFS, and Hermite functions [9, 97].

- Emerging multiple antenna technologies, such as Cell-free massive MIMO, unmanned aerial vehicle (UAV)-based MIMO, and intelligent reflecting surfaces (IRS) [2, 98], have gained significant interest in the research community. These technologies can bring substantial improvements in data rate and reliability to future network systems. Developing novel approaches to address channel delay and Doppler spreads in these scenarios is an important area of research.

- Estimation of channel parameters, i.e., delay and Doppler shifts of each path, instead of the CIR [99]. As explained in Chapter 2, the time window during which the channel parameters can be considered constant is significantly longer than the time window over which the CIR remains constant. Hence, while estimating the channel parameters might require longer pilot overhead than estimating one snapshot of the CIR, it may prove to be more efficient as it can be used for multiple transmission frames.

- In this thesis, only integer delay was considered. However, in specific scenarios such as integrated sensing and communications (ISAC) [100], the fractional delays may play a major role. Therefore, fractional delay estimation and compensation within the context of this thesis is another interesting research direction.

In conclusion, this thesis has provided significant contributions toward reducing the signaling overhead in wireless communication systems. However, each step taken toward enabling future applications and services opens new doors for even more groundbreaking innovations. Hence, new research topics emerge on the seemingly endless road from the contemporary to the next generation of wireless systems.

References

[1] F. Tariq, M. R. A. Khandaker, K.-K. Wong, M. A. Imran, M. Bennis, and M. Debbah, "A speculative study on 6g," *IEEE Wireless Communications*, vol. 27, no. 4, pp. 118–125, 2020.

[2] J. Zhang, E. Björnson, M. Matthaiou, D. W. K. Ng, H. Yang, and D. J. Love, "Prospective multiple antenna technologies for beyond 5g," *IEEE Journal on Selected Areas in Communications*, vol. 38, no. 8, pp. 1637–1660, 2020.

[3] C. Sturm and W. Wiesbeck, "Waveform design and signal processing aspects for fusion of wireless communications and radar sensing," *Proceedings of the IEEE*, vol. 99, no. 7, pp. 1236–1259, 2011.

[4] Z. Xiao, J. Yang, T. Mao, C. Xu, R. Zhang, Z. Han, and X.-G. Xia, "LEO satellite access network (LEO-SAN) toward 6g: Challenges and approaches," *IEEE Wireless Communications*, vol. 31, no. 2, pp. 89–96, 2024.

[5] M. Chafii, L. Bariah, S. Muhaidat, and M. Debbah, "Twelve scientific challenges for 6g: Rethinking the foundations of communications theory," *IEEE Communications Surveys & Tutorials*, vol. 25, no. 2, pp. 868–904, 2023.

[6] D. Tse and P. Viswanath, *Fundamentals of wireless communication.* Cambridge university press, 2005.

[7] F. Hlawatsch and G. Matz, *Wireless Communications Over Rapidly Time-varying Channels*, ser. Academic Press. Academic Press, 2011.

[8] X. Cai, X. Cheng, and F. Tufvesson, "Toward 6G with terahertz communications: Understanding the propagation channels," *IEEE Commun. Mag.*, vol. 62, no. 2, pp. 32–38, 2024.

[9] B. Farhang-Boroujeny and H. Moradi, "OFDM inspired waveforms for 5g," *IEEE Communications Surveys & Tutorials*, vol. 18, no. 4, pp. 2474–2492, 2016.

[10] P. Raviteja, K. T. Phan, and Y. Hong, "Embedded pilot-aided channel estimation for OTFS in delay–doppler channels," *IEEE Trans. Veh. Technol.*, vol. 68, no. 5, pp. 4906–4917, 2019.

[11] R. Hadani, S. Rakib, M. Tsatsanis, A. Monk, A. J. Goldsmith, A. F. Molisch, and R. Calderbank, "Orthogonal time frequency space modulation," in *IEEE Wireless Commun. and Netw. Conf. (WCNC)*, 2017, pp. 1–6.

[12] H. Tataria, M. Shafi, A. F. Molisch, M. Dohler, H. Sjöland, and F. Tufvesson, "6G wireless systems: Vision, requirements, challenges, insights, and opportunities," *Proceedings of the IEEE*, vol. 109, no. 7, pp. 1166–1199, 2021.

[13] L. Lu, G. Y. Li, A. L. Swindlehurst, A. Ashikhmin, and R. Zhang, "An overview of massive MIMO: Benefits and challenges," *IEEE Journal of Selected Topics in Signal Processing*, vol. 8, no. 5, pp. 742–758, 2014.

[14] M. Alsabah, M. A. Naser, B. M. Mahmmod, S. H. Abdulhussain, M. R. Eissa, A. Al-Baidhani, N. K. Noordin, S. M. Sait, K. A. Al-Utaibi, and F. Hashim, "6G wireless communications networks: A comprehensive survey," *IEEE Access*, vol. 9, pp. 148 191–148 243, 2021.

[15] E. G. Larsson, O. Edfors, F. Tufvesson, and T. L. Marzetta, "Massive MIMO for next generation wireless systems," *IEEE Communications Magazine*, vol. 52, no. 2, pp. 186–195, 2014.

[16] T. L. Marzetta, "Noncooperative cellular wireless with unlimited numbers of base station antennas," *IEEE Transactions on Wireless Communications*, vol. 9, no. 11, pp. 3590–3600, 2010.

[17] H. Q. Ngo and E. G. Larsson, "No downlink pilots are needed in TDD massive MIMO," *IEEE Transactions on Wireless Communications*, vol. 16, no. 5, pp. 2921–2935, 2017.

[18] A. Monk, R. Hadani, M. Tsatsanis, and S. Rakib, "OTFS-orthogonal time frequency space: A novel modulation meeting 5G high mobility and massive MIMO challenges," *arXiv:1608.02993*, 2016.

[19] L. Gaudio, G. Colavolpe, and G. Caire, "Otfs vs. ofdm in the presence of sparsity: A fair comparison," *IEEE Transactions on Wireless Communications*, vol. 21, no. 6, pp. 4410–4423, 2022.

[20] A. Farhang and M. Bayat, "SC-FDMA as a delay-doppler domain modulation technique," 2024. [Online]. Available: https://arxiv.org/abs/2402.07751

[21] F. Lampel, A. Avarado, and F. M. Willems, "On OTFS using the discrete zak transform," in *2022 IEEE International Conference on Communications Workshops (ICC Workshops)*, 2022, pp. 729–734.

[22] R. Hadani and A. Monk, "OTFS: A new generation of modulation addressing the challenges of 5g," 2018. [Online]. Available: https://arxiv.org/abs/1802.02623

[23] A. Farhang, A. RezazadehReyhani, L. E. Doyle, and B. Farhang-Boroujeny, "Low complexity modem structure for OFDM-based orthogonal time frequency space modulation," *IEEE Wireless Commun. Lett.*, vol. 7, no. 3, pp. 344–347, 2017.

[24] S. P. S. and A. Farhang, "A practical pilot for channel estimation of otfs," in *ICC 2023 - IEEE International Conference on Communications*, 2023, pp. 1319–1325.

[25] 3GPP, "NR; physical channels and modulation, July 2018," *3rd Generation Partnership Project (3GPP), TS 38.211 V15.2.0*, 2018.

[26] P. Raviteja, Y. Hong, E. Viterbo, and E. Biglieri, "Practical pulse-shaping waveforms for reduced-cyclic-prefix OTFS," *IEEE Trans. Veh. Technol.*, vol. 68, no. 1, pp. 957–961, 2019.

[27] S. E. Zegrar and H. Arslan, "A novel cyclic prefix configuration for enhanced reliability and spectral efficiency in OTFS systems," *IEEE Wireless Communications Letters*, vol. 12, no. 5, pp. 888–892, 2023.

[28] S. S. Das, V. Rangamgari, S. Tiwari, and S. C. Mondal, "Time domain channel estimation and equalization of cp-otfs under multiple fractional dopplers and residual synchronization errors," *IEEE Access*, vol. 9, pp. 10 561–10 576, 2021.

[29] A. Aminjavaheri, A. Farhang, A. Rezazadehreyhani, L. E. Doyle, and B. Farhang-Boroujeny, "OFDM without CP in massive MIMO," *IEEE Trans. on Wireless Commun.*, vol. 16, no. 11, pp. 7619–7633, 2017.

[30] A. Farhang, A. Aminjavaheri, and B. Farhang-Boroujeny, "Single carrier transmission in massive MIMO revisited," in *Int. Conf. on Comp., Netw. and Commun. (ICNC)*, 2020, pp. 96–101.

[31] H. B. Mishra, P. Singh, A. K. Prasad, and R. Budhiraja, "OTFS channel estimation and data detection designs with superimposed pilots," *IEEE Trans. Wireless Commun.*, vol. 21, no. 4, pp. 2258–2274, 2022.

[32] W. Yuan, S. Li, Z. Wei, J. Yuan, and D. W. K. Ng, "Data-aided channel estimation for OTFS systems with a superimposed pilot and data transmission scheme," *IEEE Wireless Commun. Lett.*, vol. 10, no. 9, pp. 1954–1958, 2021.

[33] W. Yuan, Z. Wei, S. Li, J. Yuan, and D. W. K. Ng, "Integrated sensing and communication-assisted orthogonal time frequency space transmission for vehicular networks," *IEEE J. Sel. Signal Process.*, vol. 15, no. 6, pp. 1515–1528, 2021.

[34] Y. Liu, Y. L. Guan, and D. G. G., "Near-optimal BEM OTFS receiver with low pilot overhead for high-mobility communications," *IEEE Trans. Commun.*, vol. 70, no. 5, pp. 3392–3406, 2022.

[35] H. Qu, G. Liu, L. Zhang, S. Wen, and M. A. Imran, "Low-complexity symbol detection and interference cancellation for OTFS system," *IEEE Trans. Commun.*, vol. 69, no. 3, pp. 1524–1537, 2021.

[36] D. L. Li and A. Farhang, "OTFS without CP in massive MIMO: Breaking doppler limitations with TR-MRC and windowing," in *2022 IEEE Wireless Communications and Networking Conference (WCNC)*, 2022, pp. 2518–2523.

[37] ——, "Joint channel estimation and equalization in massive MIMO using a single pilot subcarrier," *IEEE Wireless Communications Letters*, vol. 12, no. 11, pp. 1931–1935, 2023.

[38] A. F. Molisch, *Wireless Communications*, 2nd ed. Wiley Publishing, 2011.

[39] J. G. Proakis and D. G. Manolakis, *Digital signal processing (4th ed.): principles, algorithms, and applications.* USA: Prentice-Hall, Inc., 2007.

[40] Z. Wei, W. Yuan, S. Li, J. Yuan, and D. W. K. Ng, “Transmitter and receiver window designs for orthogonal time-frequency space modulation,” *IEEE Trans. Commun.*, vol. 69, no. 4, pp. 2207–2223, 2021.

[41] Y. Hong, T. Thaj, and E. Viterbo, *Delay-Doppler Communications: Principles and Applications.* Elsevier Science, 2022. [Online]. Available: https://books.google.ie/books?id=dGheEAAAQBAJ

[42] B. C. Pandey, S. K. Mohammed, P. Raviteja, Y. Hong, and E. Viterbo, “Low complexity precoding and detection in multi-user massive MIMO OTFS downlink,” *IEEE Transactions on Vehicular Technology*, vol. 70, no. 5, pp. 4389–4405, 2021.

[43] P. Bello, “Characterization of randomly time-variant linear channels,” *IEEE Transactions on Communications Systems*, vol. 11, no. 4, pp. 360–393, 1963.

[44] 3GPP, “Evolved universal terrestrial radio access (E-UTRA); base station (BS) radio transmission and reception,” *3rd Generation Partnership Project (3GPP), TS 36.104 V15.3.0*, 2018.

[45] ——, “LTE; 5G; study on channel model for frequency spectrum above 6 GHz,” *3rd Generation Partnership Project (3GPP), TS 38.900 V15.0.0*, 2018.

[46] W. C. Jakes and D. C. Cox, *Microwave mobile communications.* Wiley-IEEE press, 1994.

[47] M. Masood, L. H. Afify, and T. Y. Al-Naffouri, “Efficient coordinated recovery of sparse channels in massive MIMO,” *IEEE Transactions on Signal Processing*, vol. 63, no. 1, pp. 104–118, 2015.

[48] Y. Liu, Z. Tan, H. Hu, L. J. Cimini, and G. Y. Li, “Channel estimation for OFDM,” *IEEE Communications Surveys & Tutorials*, vol. 16, no. 4, pp. 1891–1908, 2014.

[49] L. Tong, B. Sadler, and M. Dong, “Pilot-assisted wireless transmissions: general model, design criteria, and signal processing,” *IEEE Signal Processing Magazine*, vol. 21, no. 6, pp. 12–25, 2004.

[50] I. Barhumi, G. Leus, and M. Moonen, “Optimal training design for mimo ofdm systems in mobile wireless channels,” *IEEE Transactions on Signal Processing*, vol. 51, no. 6, pp. 1615–1624, 2003.

[51] K. M. Z. Islam, T. Y. Al-Naffouri, and N. Al-Dhahir, “On optimum pilot design for comb-type ofdm transmission over doubly-selective channels,” *IEEE Transactions on Communications*, vol. 59, no. 4, pp. 930–935, 2011.

[52] Y. Mostofi and D. Cox, “Ici mitigation for pilot-aided ofdm mobile systems,” *IEEE Transactions on Wireless Communications*, vol. 4, no. 2, pp. 765–774, 2005.

[53] A. F. Molisch, M. Toeltsch, and S. Vermani, “Iterative methods for cancellation of intercarrier interference in OFDM systems,” *IEEE Transactions on Vehicular Technology*, vol. 56, no. 4, pp. 2158–2167, 2007.

[54] M. Toeltsch and A. Molisch, "Efficient OFDM transmission without cyclic prefix over frequency-selective channels," in *11th IEEE International Symposium on Personal Indoor and Mobile Radio Communications. PIMRC 2000. Proceedings (Cat. No.00TH8525)*, vol. 2, 2000, pp. 1363–1367 vol.2.

[55] J.-B. Lim, C.-H. Choi, and G.-H. Im, "MIMO-OFDM with insufficient cyclic prefix," *IEEE Communications Letters*, vol. 10, no. 5, pp. 356–358, 2006.

[56] Z. Chen, C. Yongyu, and D. Yang, "Low-complexity turbo equalization for MIMO-OFDM system without cyclic prefix," in *2009 IEEE 20th International Symposium on Personal, Indoor and Mobile Radio Communications*, 2009, pp. 310–314.

[57] H. Q. Ngo, E. G. Larsson, and T. L. Marzetta, "Energy and spectral efficiency of very large multiuser MIMO systems," *IEEE Transactions on Communications*, vol. 61, no. 4, pp. 1436–1449, 2013.

[58] S. M. Kay, *Fundamentals of statistical signal processing: estimation theory*. Prentice-Hall, Inc., 1993.

[59] E. Björnson, E. G. Larsson, and M. Debbah, "Massive MIMO for maximal spectral efficiency: How many users and pilots should be allocated?" *IEEE Transactions on Wireless Communications*, vol. 15, no. 2, pp. 1293–1308, 2016.

[60] H. Hosseiny, A. Farhang, and B. Farhang-Boroujeny, "FBMC receiver design and analysis for medium and large scale antenna systems," *IEEE Transactions on Vehicular Technology*, vol. 71, no. 3, pp. 3044–3057, 2022.

[61] C. Chen, J. Zhang, Y. Han, J. Lu, and S. Jin, "Channel estimation for massive MIMO-OTFS system in asymmetrical architecture," *IEEE Signal Processing Letters*, vol. 30, pp. 1412–1416, 2023.

[62] W. Shen, L. Dai, J. An, P. Fan, and R. W. Heath, "Channel estimation for orthogonal time frequency space (OTFS) massive MIMO," *IEEE Trans. on Signal Process.*, vol. 67, no. 16, pp. 4204–4217, 2019.

[63] J. Feng, H. Q. Ngo, M. F. Flanagan, and M. Matthaiou, "Performance analysis of OTFS-based uplink massive MIMO with ZF receivers," in *2021 IEEE International Conference on Communications Workshops (ICC Workshops)*. IEEE, 2021, pp. 1–7.

[64] W. Guo, W. Zhang, P. Mu, F. Gao, and H. Lin, "High-mobility wideband massive MIMO communications: Doppler compensation, analysis and scaling laws," *IEEE Trans. on Wireless Commun.*, vol. 18, no. 6, pp. 3177–3191, 2019.

[65] M. Li, S. Zhang, F. Gao, P. Fan, and O. A. Dobre, "A new path division multiple access for the massive MIMO-OTFS networks," *IEEE J. Sel. Areas Commun.*, vol. 39, no. 4, pp. 903–918, 2021.

[66] R. Hadani, S. Rakib, A. F. Molisch, C. Ibars, A. Monk, M. Tsatsanis, J. Delfeld, A. Goldsmith, and R. Calderbank, "Orthogonal time frequency space (OTFS) modulation for millimeter-wave communications systems," in *IEEE MTT-S Int. Microw. Symp. (IMS)*, 2017, pp. 681–683.

[67] P. Raviteja, E. Viterbo, and Y. Hong, “OTFS performance on static multipath channels,” *IEEE Wireless Commun. Lett.*, vol. 8, no. 3, pp. 745–748, 2019.

[68] A. RezazadehReyhani, A. Farhang, M. Ji, R. R. Chen, and B. Farhang-Boroujeny, “Analysis of discrete-time MIMO OFDM-based orthogonal time frequency space modulation,” in *2018 IEEE International Conference on Communications (ICC)*, 2018, pp. 1–6.

[69] Z. Wei, W. Yuan, S. Li, J. Yuan, G. Bharatula, R. Hadani, and L. Hanzo, “Orthogonal time-frequency space modulation: A promising next-generation waveform,” *IEEE Wireless Communications*, vol. 28, no. 4, pp. 136–144, 2021.

[70] G. D. Surabhi and A. Chockalingam, “Low-complexity linear equalization for 2×2 MIMO-OTFS signals,” in *2020 IEEE 21st International Workshop on Signal Processing Advances in Wireless Communications (SPAWC)*, 2020, pp. 1–5.

[71] ——, “Low-complexity linear equalization for otfs modulation,” *IEEE Communications Letters*, vol. 24, no. 2, pp. 330–334, 2020.

[72] P. Raviteja, K. T. Phan, Y. Hong, and E. Viterbo, “Embedded delay-doppler channel estimation for orthogonal time frequency space modulation,” in *2018 IEEE 88th Vehicular Technology Conference (VTC-Fall)*, 2018, pp. 1–5.

[73] T. Thaj, E. Viterbo, and Y. Hong, “Orthogonal time sequency multiplexing modulation: Analysis and low-complexity receiver design,” *IEEE Trans. Wireless Commun.*, vol. 20, no. 12, pp. 7842–7855, 2021.

[74] F. Long, K. Niu, and J. Lin, “Joint channel estimation and equalization for otfs based on ep,” in *2021 IEEE Global Communications Conference (GLOBECOM)*, 2021, pp. 01–06.

[75] M. Kollengode Ramachandran and A. Chockalingam, “MIMO-OTFS in high-Doppler fading channels: Signal detection and channel estimation,” in *IEEE Global Commun. Conf. (GLOBECOM)*, 2018.

[76] P. Raviteja, K. T. Phan, Q. Jin, Y. Hong, and E. Viterbo, “Low-complexity iterative detection for orthogonal time frequency space modulation,” in *IEEE Wireless Commun. and Netw. Conf. (WCNC)*, 2018, pp. 1–6.

[77] P. Raviteja, K. T. Phan, Y. Hong, and E. Viterbo, “Interference cancellation and iterative detection for orthogonal time frequency space modulation,” *IEEE Trans. Wireless Commun.*, vol. 17, no. 10, pp. 6501–6515, 2018.

[78] J.-J. van de Beek, O. Edfors, M. Sandell, S. Wilson, and P. Borjesson, “On channel estimation in OFDM systems,” in *1995 IEEE 45th Vehicular Technology Conference. Countdown to the Wireless Twenty-First Century*, vol. 2, 1995, pp. 815–819 vol.2.

[79] E. Nayebi and B. D. Rao, “Semi-blind channel estimation for multiuser massive MIMO systems,” *IEEE Transactions on Signal Processing*, vol. 66, no. 2, pp. 540–553, 2018.

[80] F. Wan, W.-P. Zhu, and M. N. S. Swamy, "A semiblind channel estimation approach for MIMO–OFDM systems," *IEEE Transactions on Signal Processing*, vol. 56, no. 7, pp. 2821–2834, 2008.

[81] C. Shin, R. W. Heath, and E. J. Powers, "Blind channel estimation for MIMO-OFDM systems," *IEEE Transactions on Vehicular Technology*, vol. 56, no. 2, pp. 670–685, 2007.

[82] D. Verenzuela, E. Björnson, X. Wang, M. Arnold, and S. ten Brink, "Massive-MIMO iterative channel estimation and decoding (MICED) in the uplink," *IEEE Transactions on Communications*, vol. 68, no. 2, pp. 854–870, 2020.

[83] Y. Huang, J. Zhang, H. Wang, Z. Zhao, and H. Yin, "Spatial multiplexing superimposed pilots for multicell multiuser MIMO uplink systems," *IEEE Systems Journal*, vol. 16, no. 2, pp. 3151–3162, 2022.

[84] A. Fengler, O. Musa, P. Jung, and G. Caire, "Pilot-based unsourced random access with a massive mimo receiver, interference cancellation, and power control," *IEEE Journal on Selected Areas in Communications*, vol. 40, no. 5, pp. 1522–1534, 2022.

[85] P.-Y. Tsai and T.-D. Chiueh, "Adaptive raised-cosine channel interpolation for pilot-aided OFDM systems," *IEEE Transactions on Wireless Communications*, vol. 8, no. 2, pp. 1028–1037, 2009.

[86] S. Colieri, M. Ergen, A. Puri, and B. A, "A study of channel estimation in ofdm systems," in *Proceedings IEEE 56th Vehicular Technology Conference*, vol. 2, 2002, pp. 894–898 vol.2.

[87] 3GPP, "NR; physical channels and modulation," *3rd Generation Partnership Project (3GPP), Technical Specification (TS) 38.211*, vol. 9, 2018.

[88] T. ETSI, "138 912, 5g," *Study on New Radio (NR) access technology (3GPP TR 38.912 version 14.0. 0 Release 14)*, vol. 14, 2017.

[89] A. M. Mathai and S. B. Provost, *Quadratic forms in random variables: theory and applications.* Dekker, 1992.

[90] T. Wang, J. Proakis, E. Masry, and J. Zeidler, "Performance degradation of OFDM systems due to Doppler spreading," *IEEE Trans. on Wireless Commun.*, vol. 5, no. 6, pp. 1422–1432, 2006.

[91] I. A. Khan and S. K. Mohammed, "A low-complexity OTFS channel estimation method for fractional delay-doppler scenarios," *IEEE Wireless Commun. Lett.*, vol. 12, no. 9, pp. 1484–1488, 2023.

[92] L. Zhao, W.-J. Gao, and W. Guo, "Sparse bayesian learning of delay-doppler channel for OTFS system," *IEEE Commun. Lett.*, vol. 24, no. 12, pp. 2766–2769, 2020.

[93] F. Liu, Z. Yuan, Q. Guo, Z. Wang, and P. Sun, "Message passing-based structured sparse signal recovery for estimation of OTFS channels with fractional doppler shifts," *IEEE Trans. Wireless Commun.*, vol. 20, no. 12, pp. 7773–7785, 2021.

[94] O. K. Rasheed, G. D. Surabhi, and A. Chockalingam, “Sparse delay-doppler channel estimation in rapidly time-varying channels for multiuser OTFS on the uplink,” in *IEEE Veh. Technol. Conf. (VTC)*, 2020, pp. 1–5.

[95] K. R. Murali and A. Chockalingam, “On OTFS modulation for high-doppler fading channels,” in *Inf. Theory and Appl. Workshop (ITA)*, 2018, pp. 1–10.

[96] M. Bayat and A. Farhang, “Time and frequency synchronization for otfs,” *IEEE Wireless Communications Letters*, vol. 11, no. 12, pp. 2670–2674, 2022.

[97] R. Haas and J.-C. Belfiore, “Multiple carrier transmission with time-frequency well-localized impulses,” in *IEEE Second Symposium on Communications and Vehicular Technology in the Benelux*, 1994, pp. 187–193.

[98] H. Q. Ngo, A. Ashikhmin, H. Yang, E. G. Larsson, and T. L. Marzetta, “Cell-free massive mimo versus small cells,” *IEEE Transactions on Wireless Communications*, vol. 16, no. 3, pp. 1834–1850, 2017.

[99] L. Gaudio, M. Kobayashi, G. Caire, and G. Colavolpe, “On the effectiveness of otfs for joint radar parameter estimation and communication,” *IEEE Transactions on Wireless Communications*, vol. 19, no. 9, pp. 5951–5965, 2020.

[100] C. Sturm and W. Wiesbeck, “Waveform design and signal processing aspects for fusion of wireless communications and radar sensing,” *Proceedings of the IEEE*, vol. 99, no. 7, pp. 1236–1259, 2011.